Time Harmonics and Unbalance Effects in Linear Induction Drives

Canadian Institute of
Guided Ground Transport
Queen's University
at Kingston, Ontario

A.R. Eastham
G.E. Dawson
J.F. Gieras
K. Anathesivam
G. John

CIGGT Report No. 85-11
Transport Canada Report No. TP-8040E

CIGGT Project No. PRO-273
CIGGT Report No. 85-11
Transport Canada Report No. TP 8040E

TIME HARMONIC AND PHASE UNBALANCE EFFECTS IN LINEAR INDUCTION DRIVES

A.R. Eastham
G.E. Dawson
J.F. Gieras
K. Ananthasivam
G. John

This study was conducted by CIGGT for the Transportation Development Centre of Transport Canada under Service Contract No. OSD83-00192

Canadian Institute of Guided Ground Transport
Queen's University
Kingston, Ontario
K7L 3N6

December 1985

89-06043/

ACKNOWLEDGEMENTS

We would like to thank Dr. J.H. Parker and Mr. W.J. Ballantyne of the Urban Transportation Development Corporation for many helpful discussions on time harmonic and phase unbalance effects in linear induction drives for urban transit, and Mr. C.A. Versailles, Project Officer at the Transportation Develpment Centre, for his interest and guidance in the development of this project.

ISBN 0 88911 272 X

Un sommaire en français de ce document est inclus avant la table des matières.

This report resulted from research conducted through the Canadian Institute of Guided Ground Transport. The report represents the views of the authors and does not necessarily have the endorsement of the University or the other participating organizations.

REPORT DOCUMENTATION FORM

1. Transport Canada Report No.
TP 8040E

2. TDC Project No.
6097, 6514

3. Recipient's Catalogue No.

4. Title and Subtitle
TIME HARMONIC AND PHASE UNBALANCE EFFECTS
IN LINEAR INDUCTION DRIVES

5. Report Date
December 1985

6. Performing Organization Report No.
85-11

7. Author(s)
A.R. Eastham, G.E. Dawson, J.F. Gieras,
K. Ananthasivam, G. John

8. Transport Canada File No.
D1465-427

9. Performing Organization Name and Address
Canadian Institute of Guided Ground Transport (CIGGT)
Queen's University
Kingston, Ontario K7L 3N6

10 DSS File No.
11SD.T8200-3-3552

11. DSS or Transport Canada Contract No.
OSD.83-00192

12. Sponsoring Agency Name and Address
Transportation Development Centre (TDC)
200 Dorchester Blvd West, Suite 601, West Tower
Montreal, Quebec H2Z 1X4

13. Type of Report and Period Covered
Final, Feb/83-Dec/85

14. Sponsoring Agency Code

15. Supplementary Notes

16. TDC Project Officer
C.A. Versailles

17. Abstract

This project was established to investigate the effects of time harmonics and phase unbalance on the performance of linear induction motors (LIMs). Two analytical models were developed, the first being based on the solution of the electromagnetic field distribution in a saturable layer model of the machine, and the second being based on the finite element technique. Analytical results were validated by comparison with the performance of a large-scale, six-pole LIM operated on the CIGGT test wheel facility.

With regard to time harmonics, it was found that higher harmonics in LIM excitation can enhance or degrade mechanical performance, depending on the modulation ratio of the inverter drive. However, effects on mechanical performance were found to be negligibly small, and the dominant effects of time harmonics are related to acoustic and electromagnetic noise.

It was shown that, under balanced voltage excitation, the unbalance in phase currents in an LIM is primarily due to longitudinal end effect. The unbalance was shown to be most prominant close to synchronous speed. The finite element method allowed the magnitude of the unbalance to be determined. Its effects were then evaluated by resolving the airgap field into positive and negative sequence components. It was shown that unless the strength of the negative sequence field is at least 20 per cent of that of the positive sequence field, the degradation in mechanical performance is small. Phase unbalance is likely to be of concern for high-speed LIMs, but not for urban transit drives.

18. Key Words
Linear induction motors,
Phase unbalance, Time harmonics,
Finite elements, Electromagnetics

19. Distribution Statement
Available on request from
CIGGT or TDC

20. Security Classification (of this report)
unclassified

21. Security Classification (of this page)
unclassified

22. No. of Pages
136

23. Price

FORMULE DE DOCUMENTATION POUR RAPPORT

1. Nº du rapport Transports Canada TP 8040E	2. Nº de l'étude — CDT 6097, 6514	3. Nº de catalogue du destinataire

4. Titre et sous-titre
TIME HARMONIC AND PHASE UNBALANCE EFFECTS IN LINEAR INDUCTION DRIVES

5. Date du rapport
décembre 1985

6. Nº du rapport de l'organisme exécutant
85-11

7. Auteur(s)
A.R. Eastham, G.E. Dawson, J.F. Gieras, K. Ananthasivam, G. John

8. Nº de dossier Transports Canada
D1465-427

9. Nom et adresse de l'organisme exécutant
Canadian Institute of Guided Ground Transport (CIGGT)
c/o Queen's University
Kingston, Ontario K7L 3N6

10. Nº de dossier — ASC
11SD.T8200-3-3552

11. Nº de contrat — ASC ou Transports Canada
OSD.83-00192

12. Nom et adresse de l'organisme parrain
Centre de développement des transports (CDT)
200 ouest, boul. Dorchester
Suite 601, tour ouest
Montréal, Québec H2Z 1X4

13. Genre de rapport et période visée
final, fév.83-déc.85

14. Code de l'organisme parrain

15. Remarques additionnelles

16. Agent de projet — CDT
C.A. Versailles

17. Résumé

Ce projet avait pour but d'étudier les effets des harmoniques temporels et des déséquilibres de phase sur la performance des moteurs à induction linéaire (MIL). Deux modèles analytiques ont été élaborés, l'un consistant à déterminer la distribution du champ électromagnétique dans une machine à couche saturable, et l'autre utilisant la méthode des éléments finis. Les résultats analytiques ont été confirmés par une comparaison avec le rendement d'un gros MIL à six pôles entraînant le volant d'essai du CIGGT.

Pour ce qui est des harmoniques temporels, les résultats indiquent que les harmoniques supérieurs de l'excitation du MIL peuvent améliorer ou dégrader le rendement mécanique de ce dernier selon le rapport de modulation de l'entraînement à inverseur. Toutefois, les effets sur le rendement mécanique se sont révélés négligeables, les effets dominants se traduisant par des bruits acoustiques et électromagnétiques.

Nous avons démontré que, lorsque les tensions d'excitation sont équilibrées, le déséquilibre des courants de phase dans un MIL est surtout dû à l'effet d'extrémité longitudinal et qu'il est plus prononcé au voisinage de la vitesse synchrone. La méthode des éléments finis nous a permis de déterminer la grandeur de ce déséquilibre. Ses effets ont ensuite été évalués en décomposant le champ dans l'entrefer, selon ses composantes positive et négative. Nous avons démontré que la dégradation du rendement mécanique est faible, à moins que la composante négative du champ ne soit au moins égale à 20% de la composante positive. Le déséquilibre de phase est probablement nuisible dans les MIL à grande vitesse, mais non dans les moteurs de véhicules de transport en commun.

18. Mots-clés
Moteurs à induction linéaire, déséquilibre de phase, harmoniques temporels, éléments finis, champ électromagnétique

19. Diffusion
On peut se procurer ce rapport en faisant la demande au CIGGT ou au CDT

20. Classification de sécurité (de ce rapport) non-classifié	21. Classification de sécurité (de cette page) non-classifiée	22. Nombre de pages 136	23. Prix

SUMMARY

The linear induction motor (LIM) offers non-contact propulsion for transit vehicles, i.e. a drive system with performance that is independent of the state of wheel/rail adhesion. The LIM can provide excellent grade climbing and reliable acceleration/braking characteristics, and is considered an appropriate drive for close-headway transit systems.

Most analytical approaches for the computation of the mechanical performance and terminal characteristics of LIMs have assumed pure sinusoidal current and balanced phase conditions. Little attention has been given to the harmonic content of the excitation, such as would be produced by a cycloconverter or inverter power conditioner, or to phase unbalance, as would be produced by phase winding asymmetry and end effects in the LIM. With regard to these factors, it may be noted that a variable-voltage, variable-frequency drive is essential to gain optimal performance from the LIM, and substantial harmonic content in the excitation is unavoidable with transistorized or thyristorized power conditioners. Also, under balanced voltage conditions, winding asymmetry and the delay in the establishment of airgap flux (end effect) causes an imbalance in the impedance of the three stator phase windings, and the resulting unbalanced phase currents have a significant negative sequence component, causing a degradation in the performance of the LIM.

This project was established to investigate the effects of time harmonics and phase unbalance on the performance of linear induction motors (LIMs). Two analytical models were developed, the first being based on the solution of the electromagnetic field distribution in a saturable layer model of the machine, and the second being based on the finite element technique. Analytical results were validated by comparison with the performance of a large-scale, six-pole LIM operated on the CIGGT test wheel facility.

With regard to time harmonics, it was found that higher harmonics in LIM excitation can enhance or degrade mechanical performance, depending on the modulation ratio of the inverter drive. However, effects on mechanical performance were found to be negligibly small,

and the dominant effects of time harmonics are related to acoustic and electromagnetic noise.

It was shown that, under balanced voltage excitation, the unbalance in phase currents in an LIM is primarily due to longitudinal end effect. The unbalance was shown to be most prominant close to synchronous speed. The finite element method allowed the magnitude of the unbalance to be determined. Its effects were then evaluated by resolving the airgap field into positive and negative sequence components. It was shown that unless the strength of the negative sequence field is at least 20 per cent of that of the positive sequence field, the degradation in mechanical performance is small. Phase unbalance is likely to be of concern for high-speed LIMs, but not for urban transit drives.

SOMMAIRE

Le moteur à induction linéaire (MIL) permet d'obtenir un système de propulsion sans contact pour les véhicules de transport en commun, donc, un système dont la performance ne dépend pas des conditions d'adhésion des roues aux rails. Le MIL s'avére excellent pour gravir les pentes et posséde des caractéristiques d'accélération et de freinage fiables; il est par conséquent approprié aux systèmes de transport en commun à faible espacement entre les véhicules.

La plupart des calculs du rendement mécanique et des caractéristiques terminales du MIL reposent sur les hypothèses que le courant est exactement sinusoidal et qu'il n'y a aucun déséquilibre de phase. Jusqu'ici, on a fait peu de cas des harmoniques de l'excitation, comme ceux produits par un cycloconvertisseur ou un conditionneur de puissance inverseur, ni des déséquilibres de phase, comme ceux produits par l'asymétrie des enroulements statoriques et les effets d'extrémité dans le MIL. Pour ce qui a trait à ces facteurs, on remarquera qu'un entraînement à tension et à fréquence variables est essentiel en vue optimiser la performance du MIL, et qu'un contenu harmonique substantiel est inévitable dans l'exitation lorsqu'on utilise des conditionneurs de puissance à transistors ou à thyristors. Par ailleurs, lorsque les tensions d'excitation sont équilibrées, l'asymétrie des enroulements et le retard d'établissement du flux dans l'entrefer (effet d'extrémité) entraînent un déséquilibre d'impédance entre les trois enroulements statoriques et, par suite du déséquilibre résultant dans les courants de phase, ceux-ci ont une composante négative importante, ce qui entraîne une dégradation de la performance du MIL.

Ce projet avait pour but d'étudier les effets des harmoniques temporels et des déséquilibres de phase sur la performance des moteurs à induction linéaire (MIL). Deux modèles analytiques ont été élaborés, l'un consistant à déterminer la distribution du champ électromagnétique dans une machine à couche saturable, et l'autre utilisant la méthode des éléments finis. Les résultats analytiques ont été confirmés par une comparaison avec le rendement d'un gros MIL à six pôles entraînant le volant d'essai du CIGGT.

Pour ce qui est des harmoniques temporels, les résultats indiquent que les harmoniques supérieurs de l'excitation du MIL peuvent améliorer ou dégrader le rendement mécanique de ce dernier selon le rapport de modulation de l'entraînement à inverseur. Toutefois, les effets sur le rendement mécanique se sont révélés négligeables, les effets dominants se traduisant par des bruits acoustiques et électromagnétiques.

Nous avons démontré que, lorsque les tensions d'excitation sont équilibrées, le déséquilibre des courants de phase dans un MIL est surtout dû à l'effet d'extrémité longitudinal et qu'il est plus prononcé au voisinage de la vitesse synchrone. La méthode des éléments finis nous a permis de déterminer la grandeur de ce déséquilibre. Ses effets ont ensuite été évalués en décomposant le champ dans l'entrefer, selon ses composantes positive et négative. Nous avons démontré que la dégradation du rendement mécanique est faible, à moins que la composante négative du champ ne soit au moins égale à 20% de la composante positive. Le déséquilibre de phase est probablement nuisible dans les MIL à grande vitesse, mais non dans les moteurs de véhicules de transport en commun.

TABLE OF CONTENTS

1. INTRODUCTION 1
    1.1 Rationale for Project 1
    1.2 Linear Electric Drive's Resarch at CIGGT 2
    1.3 Time Harmonics and Phase Unbalance 3
    1.4 Work Statement 6
    1.5 Structure of Report 9

2. PULSE WIDTH MODULATION AND SPECTRAL ANALYSIS 10
    2.1 Introduction 10
    2.2 PWM Inverters in AC Drives 10
    2.3 Pulse Width Modulation 11
        2.3.1 Types of Pulse Modulation 12
        2.3.2 Two-Level and Three-Level Modulation 12
    2.4 Developments in PWM Techniques 13
        2.4.1 Natural Sampled Modulation 13
        2.4.2 Regular Sampled Modulation 16
        2.4.3 Optimized PWM 17
    2.5 Generation of Naturally and Regularly Sampled Waveforms 18
        2.5.1 Naturally Sampled PWM 18
        2.5.2 Regularly Sampled PWM 18
    2.6 Harmonic Analysis 19
        2.6.1 Simulation of Three-Phase PWM Inverters 20
    2.7 Simulation of 200 kVA Inverter System 20
        2.7.1 Commutation Rate and Frequency Ratio Control . . . 23
        2.7.2 Minimum Notch-Width 23
        2.7.3 Generation of the Output Waveform 24
        2.7.4 Verification of the Harmonic Spectrum of the Inverter 25

3. HARMONIC BEHAVIOUR OF ROTARY INDUCTION MACHINES 28
    3.1 Introduction 28
    3.2 Nature of Input Waveforms 29
    3.3 Harmonic Equivalent Circuits 30
    3.4 Harmonic Currents 33
    3.5 Motor Losses 33
        3.5.1 Stator Copper Loss 33
        3.5.2 Rotor Copper Loss 34
        3.5.3 Core Loss 34
    3.6 Motor Efficiency 35
    3.7 Harmonic Torques 36

4. TIME HARMONIC EFFECTS IN LINEAR INDUCTION DRIVES 39
    4.1 Analysis 39
    4.2 Computation 39
    4.3 Experimental Machine 40
        4.3.1 Test Equipment 40
        4.3.2 Test Programs 43

4.4 Comparison of Computed and Test Results 44
    4.4.1 Time Harmonic Effects for Aluminum-Capped Rail . . 44
    4.4.2 Time Harmonic Effects for Solid-Steel Rail 47

5. FINITE ELEMENT ANALYSIS APPLIED TO LINEAR INDUCTION MACHINES. . 51
5.1 Phase Unbalance 51
5.2 The Finite Element Method 53
5.3 Discretization 53
5.4 Representation of Excitation 56
5.5 Calculation of Performance 56
5.6 Finite Element Analysis of Test LIM 58
    5.6.1 DC Magnetostatic Test 58
    5.6.2 Complex Steady-State Solution 59
    5.6.3 Comparison of Finite Element and Test Results . . . 74

6. PHASE UNBALANCE EFFECTS IN LIMs 81
6.1 Introduction 81
6.2 Formulation of the Modified Finite-Element Method 81
6.3 Computation Model 84
6.4 Constant Voltage Tests 85
6.5 Unbalance Tests 85
6.6 Effect of Phase Unbalance 91
6.7 Review of Phase Unbalance Effects 96

7. REVIEW AND CONCLUSIONS 98
7.1 Review of Activities 98
    7.1.1 Time Harmonics 98
    7.1.2 Phase Unbalance 99
7.2 Conclusion 100

REFERENCES 102

Appendix A: PERFORMANCE CALCULATION FOR SINGLE-SIDED LINEAR INDUCTION MOTORS WITH A DOUBLE-LAYER REACTION RAIL UNDER CONSTANT CURRENT EXCITATION

Appendix B: FINITE-ELEMENT ANALYSIS OF LIMs

LIST OF TABLES

1. Design Parameters of Test LIM 42
2. Magnitude and Phase Angles of Phase Currents for Different Unbalance Factors 93

LIST OF FIGURES

1. Voltage (upper) and current (lower) waveforms from the Reliance 200 kVA PWM inverter under LIM drive 5
2. Generation of two-level PWM 14
3. Generation of three-level PWM 14
4. Naturally sampled PWM 15
5. Regularly sampled PWM 15
6. Output voltage waveforms 21
7. Harmonic spectra of the naturally sampled waveforms 22
8. Frequency control of PWM inverters 24
9. Reliance inverter waveforms 25
10. Computed harmonic spectra of the inverter waveforms 26
11. Measured harmonic spectra of the inverter waveforms 27
12. Typical waveforms of a voltage source inverter 29
13. Fundamental frequency equivalent circuit 31
14. Equivalent circuit for harmonic current calculation 31
15. Efficiency of medium hp induction motors 36
16. Sixth harmonic torque pulsation 38
17. Flowchart for computation of thrust and normal force in LIM . . 41
18. SLIM rail configuration 42
19. Waveform and harmonic spectrum of Reliance inverter output . . 45
20. LIM thrust for the Al-capped reaction rail. 46
21. Normal force for the Al-capped reaction rail 46
22. Computed thrust and normal force for the harmonic voltages in Figure 19 for Al-capped reaction rail 48
23. Typical harmonic spectrum and performance curves for the LIM with Al-capped reaction rail 48
24. Typical harmonic spectrum and performance curves for the LIM with Al-capped reaction rail 49
25. Thrust for the LIM with solid-steel reaction rail 49
26. Normal force for the LIM with solid-steel reaction rail 50
27. Harmonic spectrum of Reliance inverter and performance curves for the LIM with solid-steel reaction rail 50
28. (a) The geometry of the test LIM, with x-axis compressed relative to y-axis 54
    (b) The finite element discretization used for analysis of field distribution 54
29. Discretization of a typical tooth-slot unit 55
30. Distribution of normalized current at the nodes of a slot . . . 56
31. Terminal connection for the magnetostatic test 59
32. (a) MMF distribution with 200, -100 and -100 Amperes in Phase A, B and C, respectively 60
    (b) Comparison of airgap flux density, as measured and as computed using the finite element model 60

33. Flux plots for complex steady-state finite element solution for f=11 Hz, at a slip frequency of 7 Hz 62
34. Flux plot for the real component of the complex steady-state finite-element solution 63
35. Schematic of expected pattern of flux lines 65
36. Induced current density curves (real component) for f=11 Hz, at a slip frequency of 7 Hz 66
36. Induced current density curves (imaginary component) for f=11 Hz, at a slip frequency of 7 Hz 67
38. Flux density, thrust density and normal force density for f=11 Hz, at a slip frequency of 22 Hz 68
39. Flux density, thrust density and normal force density for f=11 Hz, at a slip frequency of 7 Hz 69
40. Flux density, thrust density and normal force density for f=11 Hz, at a slip frequency of 0 Hz 70
41. Flux density, thrust density and normal force density for f=11 Hz, at a slip frequency of -7 Hz 71
42. Flux plot for the real component of the complex steady-state finite-element solution for f=40 Hz, at a slip frequency of 7 Hz 72
43. Flux density, thrust density and normal force density for f=40 Hz, at a slip frequency of 7 Hz 73
44. Comparison of computed and test results for different frequencies at 200 A for thurst and normal force 75
45. Comparison of computed and test results for difference currents at 28 Hz for thrust and normal force 76
46. Comparison of computed and test results for flux density for f=11 Hz at slips of 0.0, 0.619 and 1.0 78
47. Comparison of computed and test results for flux density for f=11 Hz at slips of 0.0, 0.272 and 1.0 79
48. Comparison of computed and test results for flux density for f=11 Hz at slips of 0.0, 0.161 and 1.0 80
49. LIM equivalent circuit showing the parameters included in finite-element analysis 82
50. Longitudinal section of LIM showing conductors in one phase . . 83
51. Matrix structures of the two finite-element methods 84
52. Comparison of test results and finite-element computations for thrust and normal force, with constant voltages of 160 V at 60 Hz 86
53. Comparison of test results and finite element computations for phase currents, with a contant voltage of 200 V at 60 Hz . . . 87
54. Experimental results for phase currents and the unbalance factor as a function of speed, with constant volts/Hz of 2.67 at 11, 28 and 40 Hz. 89
55. Finite-element results for phase currents and the unbalance factor as a function of speed, with constant volts/Hz of 2.67 at 11, 28 and 40 Hz 90
56. Phasor diagram for star-connected primary 92
57. Thrust and normal force for f=11, 28 and 40 Hz, for unbalance factors of 0, 0.25 and 0.5 94
58. Expected pattern of thrust and normal forces and their sum as a function of speed for positive and negative sequent currents . 95
59. Peak thrust as a function of unbalance factor for f=6, 11, 28 and 40 Hz 96

1. INTRODUCTION

1.1 Rationale for Project

The linear induction motor (LIM) offers non-contact propulsion for transit vehicles, i.e. a drive system with performance that is independent of the state of wheel/rail adhesion. The LIM can provide excellent grade climbing and reliable acceleration/braking characteristics, and is considered an appropriate drive for close-headway transit systems. An LIM drive was developed for integration with an advanced steerable-axle truck suspension in UTDC's intermediate-capacity transit system. This transit vehicle system is now in operation in Scarborough and Vancouver, and is being implemented in downtown Detroit.

Most analytical approaches for the computation of the mechanical performance and terminal characteristics of LIMs have assumed pure sinusoidal current and balanced phase conditions. Little attention has been given to the harmonic content of the excitation, such as would be produced by a cycloconverter or inverter power conditioner, or to phase unbalance, as would be produced by phase winding asymmetry and end effects in the LIM. With regard to these factors, it may be noted that a variable-voltage, variable-frequency drive is essential to gain optimal performance of the LIM, and substantial harmonic content in the excitation is unavoidable with transistorized or thyristorized power conditioners. Also, under balanced voltage conditions, winding asymmetry and the delay in the establishment of airgap flux (end effect) causes an imbalance in the impedance of the three stator phase windings, and the resulting unbalanced phase currents have a significant negative sequence component, causing a degradation in the performance of the LIM.

The specific objective of the work reported here was to develop an analytical model to evaluate the effects and consequences of time harmonics and phase unbalance on the performance of linear induction motors. This study was conducted in consultation with UTDC, as it was considered that the results would be revelant to the operation and improved performance of LIM drives in Canadian transportation systems.

1.2 Linear Electric Drives Research at CIGGT

CIGGT became involved in linear electric drives with the establishment of the Canadian Maglev Group, formed by engineers at Queen's University, the University of Toronto, and McGill University. The Institute administered a three-phase, six-year program, funded by the Transportation Development Centre (TDC) of Transport Canada, which established the technical feasibility of high-speed ground transportation using superconductive electrodynamic suspension and linear synchronous motor propulsion. This project, which included the establishment of a large rotating wheel facility to test the suspension and propulsion concepts using effectively full-scale components, was completed in 1977 [1,2].

Subsequent to the successful completion of electro-dynamic suspension and linear synchronous motor tests, CIGGT was approached by the MITRE Corporation to conduct a test program on a single-sided linear induction motor with a squirrel-cage reaction rail, as part of a USDOT/UMTA-funded feasibility study of the LIM in the integrated suspension/propulsion (ISPS) mode of operation. After upgrading the test wheel facility by the addition of a 64-channel microcomputer-based data acquisition and processing system, the test program was conducted over the summer of 1978 [3]. The MITRE Corporation reported that they considered the data to be reliable and adequate for their assessment of the LIM in the ISPS mode for high-speed ground transportation [4].

A subsequent examination of the CIGGT SLIM test data indicated an inadequacy for the assessment of the squirrel-cage machine as a drive unit for lower-speed systems. For high-speed ISPS assessment, CIGGT obtained performance characteristics for the SLIM over a wide range of positive slip conditions. However, for applications involving frequent stop-go operations, knowledge of the braking performance of the machine becomes important. After discussions with Canadair Services Ltd. and UTDC, a CIGGT proposal to experimentally evaluate the braking performance of the squirrel-cage SLIM in both regenerative and plugging modes was accepted. This test work was conducted during May/June 1979 [5].

In early 1979, CIGGT was again approached by the MITRE Corporation to conduct a second test program on the single-sided LIM, with a solid steel rather than cage reaction rail. Again their interest lay in the assessment of the machine in the ISPS mode of operation. The necessary modifications to the wheel facility were made, i.e. the cage rail was replaced by a solid steel strip on the wheel rim, and the second MITRE test program was conducted over the period July/August 1979 [6].

Again this data was considered inadequate for an examination of solid steel reaction rails for low-speed urban transit SLIM drives. Funding was therefore sought from TDC to expand the solid-steel rail test program to obtain the required data. The linear induction motor test equipment assembled at Queen's University also offered the opportunity to conduct tests on the sheet reaction rail configuration. While extensive test data had been obtained with this type of SLIM by other groups, it was considered that test results using a common SLIM primary were highly desirable for a comparative assessment of the performance characteristics of an LIM with the three different reaction rails. The Transportation Development Centre gave a contract to CIGGT to obtain further solid steel rail test data, to modify the test facility and to procure comparative sheet reaction rail test data. This test work was successfully completed over the summer of 1980 [7].

A subsequent test program was related to the performance and control of a variable-voltage fixed-frequency (VVFF) LIM drive system. As a result of a Department of Electrical Engineering study, this mode of LIM drive appeared to be technically feasible for a certain class of transit operation, such a downtown people-movers or airport shuttle services [8]. In order to evaluate and test the concept, a thyristorized 200 kVA phase-controlled power conditioner was built. The VVFF LIM was operated under both speed and thrust control on the CIGGT test wheel. The test and demonstration aspects of this work were conducted under contract to Metro Canada Limited, and were completed during 1982 [9].

1.3 Time Harmonics and Phase Unbalance

As a result of the above test programs, CIGGT had acquired extensive test data and operating experience with LIM drives. All the data catalogued related to the steady-state mechanical performance, terminal characteristics and flux distribution in the machine, without regard to the nature of the excitation waveform. In fact, deliberate steps were taken to isolate and record only the fundamental component of periodic signals by digital filtering in the processing phase of data reduction. In addition, phase unbalance was ignored by taking the average of the three phase voltages, currents and powers for presentation of the performance characteristics of the test LIM.

(a) Time Harmonics

In order to achieve the best overall performance of an LIM drive system, it is necessary to operate the machine under variable-voltage variable-frequency (VVVF) conditions, and to use an optimal slip frequency control algorithm (as used by UTDC for the ICTS LIM drive). Variable frequency operation implies the use of either a cycloconverter (from a three-phase ac supply) or an inverter (from a dc supply), both of which introduce substantial harmonic content to the motor excitation.

Examples of the pulse-width-modulated (PWM) nature of the line voltage output and the phase current of the Reliance 200 kVA inverter used for LIM tests at CIGGT are shown in Figure 1. These waveforms are typical of those from PWM voltage source inverters, as used for ICTS. It is apparent that the harmonic content of these waveforms is very significant. Inadequate attention had been given to this feature of LIM drives.

Time harmonics in the excitation of LIMs can have a number of effects:

- components of thrust, which may provide either motoring or braking action, and normal force, in addition to the forces produced by the fundamental excitation
- additional heating due to induced currents in the primary copper and in the reaction rail, and due to increased iron losses; these effects lead to a degradation in efficiency
- electromagnetic interference in nearby inductive loops, such as those installed for communication and control of a transit system
- acoustic noise, due to magnetostriction and other effects.

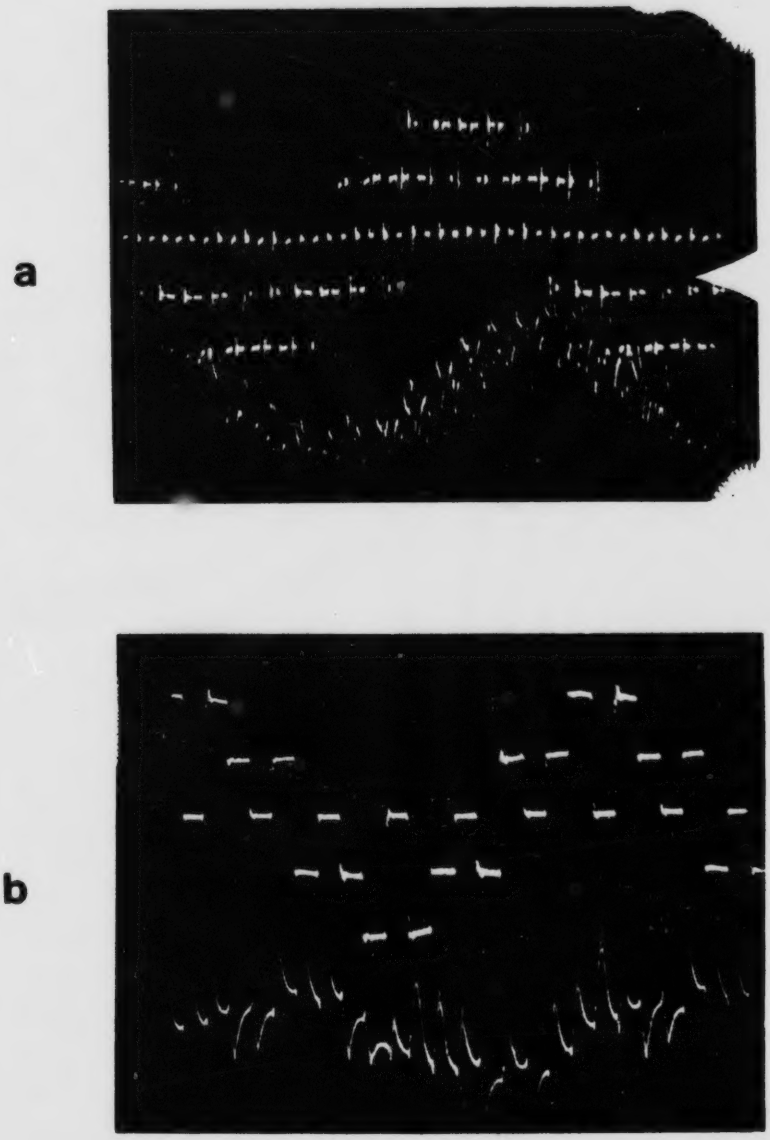

Figure 1 Voltage (upper) and current (lower) waveforms from the Reliance 200 kVA PWM inverter under LIM drive:
(a) 28 Hz, 300 V, 200 A
(b) 90 Hz, 318 V, 100 A

(b) Phase Unbalance

One of the features which distinguishes linear from rotary induction motors is the end effect resulting from parasitic eddy currents in the reaction rail at the entry end of the machine. Thus, induced currents delay the establishment of airgap flux and cause a degradation in the high-speed performance of the machine. The end effect and the asymmetry longitudinal placement of the phase windings leads to a difference in flux linkage and thus a difference in input impedance of the three stator phase windings. For balanced three-phase voltages, the phase currents are correspondingly unbalanced, causing negative sequence fields and a further degradation in performance.

Phase unbalance in the excitation of LIMs can have the following effects:

- generation of negative sequence fields, producing a component of braking (or motoring) action when the LIM is operating in motoring (or braking) mode.
- overloading of one or two of the phase legs of the VVVF power conditioner.

1.4 Work Statement

The specific objective of the work reported here was to develop an analytical model to evaluate the effects and consequences of time harmonics and phase unbalance on the performance of linear induction motors. This objective has been successfully met, and the conclusions and recommendations are presented in Chapter 7 of this report.

TDC's detailed Statement of Work specified the following activities. The corresponding work accomplished is summarized after each item.

(i) Develop a detailed work plan and activity schedule within one month of effective commencement date.

CIGGT's work plan and activity schedule was prepared and submitted to TDC with the first project progress report, dated 31 March 1984.

(ii) Conduct preliminary laboratory tests on time harmonic and phase unbalance effects in rotary induction machines.

A 5 hp, 208 V, 60 Hz, four-pole induction motor was purchased from Canadian General Electric. This was mounted on a test bed with torque/speed transducers and dc machine load. The induction machine was excited by a 60 Hz sinusoidal source and by a 7.5 kVA PWM inverter, providing both voltage and frequency control. The harmonic behavior of rotary induction motors is reported in Chapter 3. Experience with the small rotary motor provided a good appreciation of time harmonic and phase unbalance effects, and served to test out and calibrate the instruments for high-power LIM tests.

(iii) Draw up test plan, in consultation with UTDC.

A test plan for the evaluation of time harmonic and phase unbalance effects in LIMs was drawn up in consultation with Dr. J.H. Parker and Mr. W.J. Ballantyne at UTDC.

(iv) Prepare test facilities, calibrate instrumentation and recommission data acquisition system.

The CIGGT wheel facility was prepared for the time harmonic and phase unbalance LIM test program, as describe in Chapter 4. The instrumentation was assembled and calibrated using the low-power rotary machine test bed, and the 64-channel data acquisition system used for previous LIM test programs was again made fully operational.

(v) Conduct time harmonic and phase unbalance tests with solid steel rail LIM.

While the solid steel reaction rail is of little interest for LIM drives (apart from those which are operated at constant line frequency), some preliminary tests of the time harmonic and phase unbalance effects were conducted, as reported in Chapter 4.

(vi) Design aluminum-capped rail, and subcontract for fabrication and mounting.

The aluminum cap for the reaction rail was designed to be similar to that employed by UTDC for the ICTS LIM drive, i.e. with a 4.5 mm thickness over the core and thicker side bars to accommodate longitudinal currents. The aluminum cap rail sections were fabricated by a local subcontractor.

(vii) Conduct time harmonic and phase unbalance tests with solid aluminum-capped rail LIM.

Most of the analytical and experimental work was focussed on the aluminum-capped reaction rail configuration. Test results are reported in Chapters 4 and 6.

(viii) Analyze time harmonic and phase unbalance effects in LIM drives.

Two versatile techniques were developed for analytical studies of time harmonic and phase unbalance effects in LIMs, based on the electromagnetic field distribution in a layer model of the machine and on the finite element method. These analyses are described in Chapters 4 and 5.

(ix) Evaluate consequences of LIM harmonics and phase unbalance in LIM drives.

The consequences of time harmonics and phase unbalance became evident as a result of the analytical and experimental work. In general, neither factor produced significant degradation in the performance of the types of LIM likely to be employed for urban transit. Phase unbalance was shown to be more significant for higher-speed LIMs.

(x) Formulate recommendations for improved LIM design and operation.

In general, it was found that neither time harmonics nor phase unbalance produced sufficient effect on the mechanical performance of urban transit LIMs to be a major concern in the design process. Apart from acoustic noise, the dominant consideration in specifying PWM strategies is to avoid interference with signalling and control systems. The effects of phase unbalance are negligible for urban-transit LIMs, but can be significant for high-speed LIMs. The conclusions and recommendations of this work are reported in Chapter 7.

1.5 Structure of Report

The report is structured such that the two aspects of LIM operation under investigation, namely time harmonics and phase unbalance, are treated sequentially. The report begins with a review of PWM strategies applicable to both rotary and linear drives, and with analysis of the harmonic content of PWM waveforms. The harmonic behaviour of rotary induction machines is then discussed, followed by analysis and test results of time harmonic effects in linear induction drives.

2. PULSE WIDTH MODULATION & SPECTRAL ANALYSIS

2.1 Introduction

Variable speed drives utilizing an ac motor fed with variable-frequency three-phase ac derived from an inverter are now finding wide industrial application. An inverter used for this purpose must regulate the frequency in accordance with the desired speed, and must regulate the voltage proportionally with the frequency so as to maintain the flux density within the machine at the normal operating value. It is generally recognized that PWM inverters offer a number of advantages over rival converter techniques.

The operational characteristics of PWM inverters depend intrinsically on quite complex modulation processes. Analysis techniques based on Fourier-series methods have been proposed and used to derive analytical expressions for the harmonic spectra of PWM waveforms [10,11]. These expressions can provide the system designer with valuable insight into the harmonic structure of the PWM waveform and the relationships which exist between the various harmonics and the parameters of the modulation process. Unfortunately, in general, this approach can only be applied to well-defined modulation processes, and usually requires quite complex and lengthy analysis involving Bessel function series to derive the harmonic spectra expressions.

An alternative method of analysis, which is more general and can in principle be used to investigate a wide range of PWM systems uses the digital computer to model the PWM process. The simulation model can then be used as the basis for computer investigations of a wide range of operating modes, using both time and frequency domain analysis techniques. This was the approach used in this investigation [12].

2.2 PWM Inverters in AC Drives

For a modest speed range of perhaps two- or three-to-one, a simple six-step inverter, fed by a variable-voltage dc power supply, can meet the requirements [13]. However, as the speed range becomes larger and low-speed operation is required, three problems become significant. First, the supply voltage becomes so low as to impair the commutation capability of the inverter. Second, harmonics of the six-step waveform interact with the fundamental to produce low-frequency torques which produce irregular rotation at very low speeds. Third, the fact that the voltage control loop includes a substantial delay, contributed by the low pass filter between the dc supply and the inverter, jeopardizes the low speed stability of the drive.

All three problems can be overcome by the use of pulse width modulation (PWM). The supply voltage remains constant and good commutation capability is maintained. Harmonics are raised to the vicinity of the inverter carrier frequency, and the resultant high-frequency torques are rendered harmless by the low pass mechanical characteristic provided by the inertia of the rotor and load. The voltage regulating function is performed within the inverter, and can therefore be effected with the same response as the frequency control.

However, the solution of one set of problems introduces others. The first of these arises because the switching frequency of the necessary high-power thyristorized inverters is approximately limited to the range 250-1000 Hz. Modulation of such a carrier so as to produce an output frequency up to say 120 Hz, corresponding to double the normal motor speed, introduces undesirable low harmonic frequencies. A six-step inverter would, of course, have no problem producing such an output frequency and its first effective harmonic, at five times the inverter frequency, would be acceptably high. Second the utilization of the dc power supply is poor in the case of PWM inverters.

Since commutation is not a problem at the higher voltages associated with the higher speeds, and since drive stability is more easily assured at the higher speeds, it is advantageous to combine the merits of the two systems. Pure PWM may be used at the lower speeds and pure six-pulse operation used at the higher speeds, with a transitional stage from one mode of control to the other at an intermediate speed. Before an attempt is made to study the features of such an inverter system, pulse width modulated systems and harmonic analysis techniques are reviewed.

2.3 Pulse Width Modulation

Pulse width modulation essentially involves the sampling of an information signal [10]. The sampled information content is then converted into a series of modulated pulses having pulsewidths that reflect the amplitude of the information signal. In power converter applications, these width-modulated pulses provide the means of controlling the switching sequence of the devices in the power stage of the inverter.

2.3.1 Types of Pulse Modulation

There are, in general, three ways in which the width of pulses may be modulated:

- leading edges occurring at uniformly spaced intervals and the trailing edges modulated
- trailing edges at uniformly spaced intervals and the leading edges modulated
- both edges modulated, or "double edge modulation".

In the production of PWM, the sampling technique employed involves a direct comparison between the amplitudes of a modulating wave and a sweep wave (at the sampling or carrier frequency). The instantaneous intersections of the two waves are then used to determine the switching instants of the width-modulated pulses. The type of modulation is determined by the shape of the sweep wave. For leading-edge modulation, a positive-ramp sweep wave is required; for trailing-edge, a negative ramp; and for double-edge, a triangular wave. It can be shown analytically that, compared with double-edge modulation, single-edge modulation produces significantly greater harmonic distortion [10,14]. This is to be expected, since considerably less information can be transmitted. For this reason, only double-edge modulation is considered in the following sections.

2.3.2 Two-Level and Three-Level Modulation

The PWM wave output can involve either two or three levels. The synthesis of two-level PWM is shown in Figure 2. This waveform is typical of the inverter pole voltage, and can be considered as switching between +H and -H, where H is the magnitude of pole voltage. It can be observed from the diagram that one complete cycle in the variation of pulse widths requires one complete cycle of the modulating wave.

In three-level modulation, the wave may be considered as switching between +H, 0, and -H, as shown in Figure 3. This waveform is typical of the line-to-line voltage waveform in single-phase and three-phase inverters. The three-level waveform can either be generated by combining two suitably phased two-level waveforms, or generated directly as shown in the Figure 3. The pulses change polarity every half-cycle and the width of the pulses in each half-cycle of the output must therefore be modulated according to the positive half-cycle of the modulating wave. The polarity discriminator illustrated in Figure 3 represents the function of the gating logic which is necessary to correctly apply the PWM gating sequence to the power-circuit thyristors.

2.4 Developments in PWM Techniques

It is possible, by surveying the literature over the last decade [15], to trace the development of PWM inverter control techniques and to relate these developments to changes in converter technology. It is helpful to recognize three distinct PWM switching strategies, i.e.:

- natural sampled PWM
- regular sampled PWM
- optimised PWM.

The modulating principles associated with each PWM switching strategy are outlined below and are used to derive equations which describe the PWM switching process. These equations form the basis for the development of computer models and associated algorithms. Only sinusoidal modulation, which is commonly used in PWM schemes, will be considered, although other types of modulation such as trapezoidal, square, etc., can be analysed in a similar manner.

2.4.1 Natural Sampled Modulation

This is the most widely used mode because of its ease of implementation using analog techniques. A practical implementation, showing the general features of this mode of sampling, is illustrated in Figure 4.

It is important to note that, because the switching edge of the width-modulated pulse is determined by the instantaneous intersection of the two waves, the resultant pulse width is proportional to the

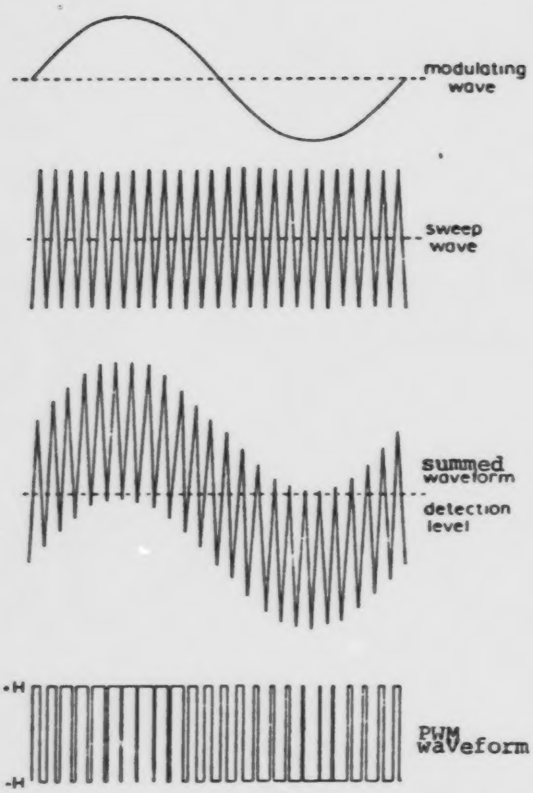
modulating wave
sweep wave
summed waveform
detection level
+H
-H
PWM waveform

◄ Figure 2

Generation of two-level PWM

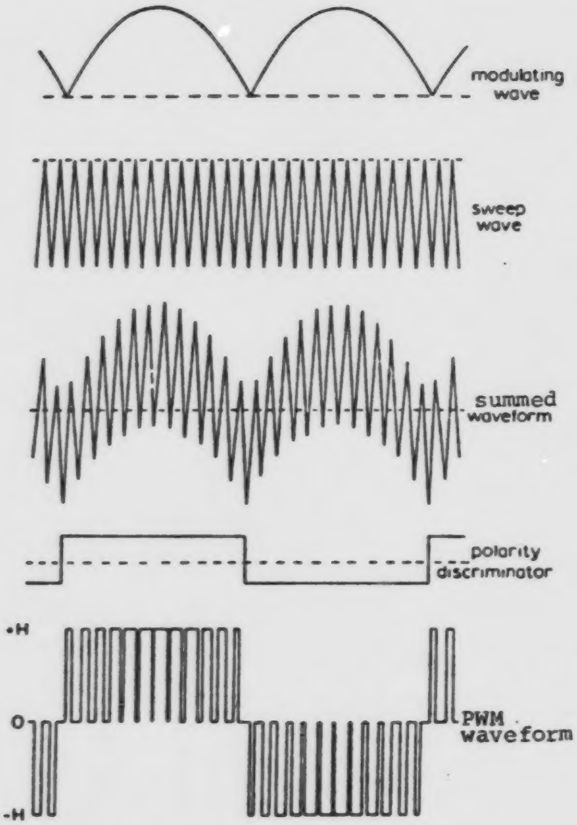
modulating wave
sweep wave
summed waveform
polarity discriminator
+H
0
-H
PWM waveform

Figure 3 ►

Generation of three-level PWM

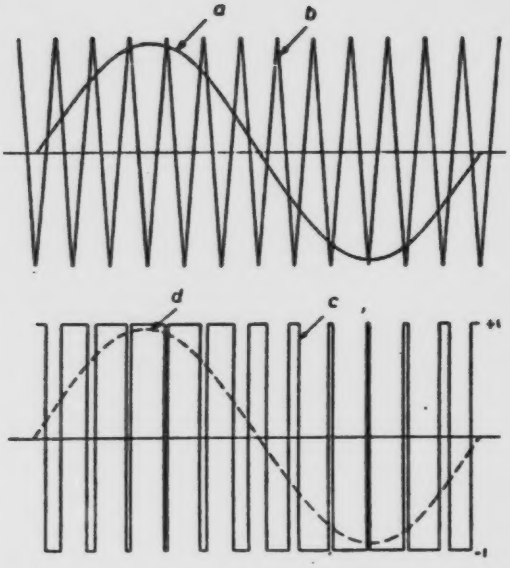

◄ Figure 4

Naturally sampled PWM

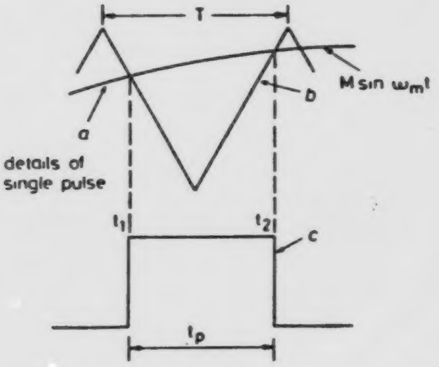
T
M sin ωmt
b
a
details of single pulse
t1
t2
c
tp

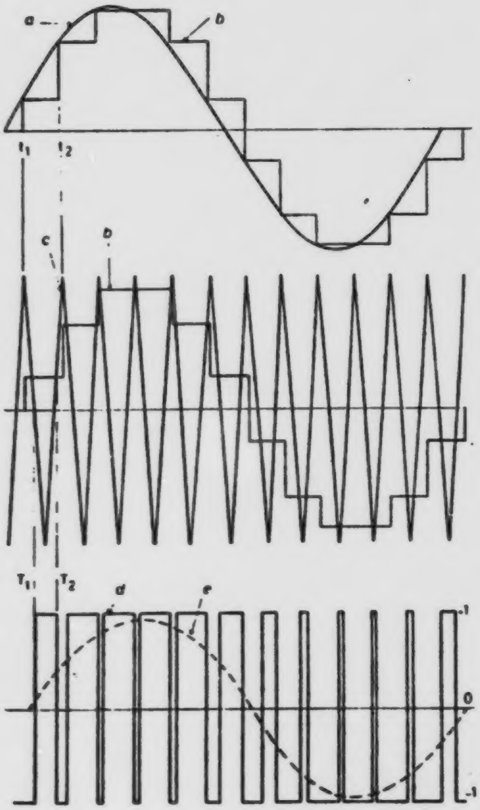
a
b
t1
t2
c
b
T1
T2
d
e
1
0
-1

Figure 5 ►

Regularly sampled PWM

amplitude of the modulating wave at the instant that switching occurs. This has two important consequences:

- centres of the pulses in the resultant PWM wave are not uniformly spaced
- it is not possible to define the widths of the pulses using analytic expressions.

The widths of the pulses can be defined using a transcendental equation [10,14]. Because of the transcendental relationship existing between the switching times, it is not possible to calculate the widths of the modulated pulses directly. It can only be defined in terms of a series of Bessel functions. In the computer-modelling approach, the analog process illustrated in Figure 4 is simulated directly in computer software, and the PWM switching instants are determined using numerical techniques. As shown in Figure 4, the PWM switches between two voltage levels, +1 and -1, and is therefore a two-level PWM. It is also possible to generate a three-level PWM in this manner.

2.4.2 Regular Sampled Modulation

In contrast with natural sampled modulation, regular sampling produces pulse durations which have a linear relationship with the modulation values. A practical implementation, illustrating the general features of this mode of sampling for two-level PWM, is shown in Figure 5. In this mode of control, the amplitude of the modulating signal, a, at the sampling instant, t_1, is stored by a sample-and-hold circuit (operated at the carrier frequency), and is maintained at a constant level during the intersample period, t_1 to t_2, until the next sample is taken. This produces a sample-hold, or amplitude-modulated version of the modulating signal, b. Comparison of signal b with the carrier signal, c, defines the points of intersection used to determine the switching instants, T_1 and T_2, of the width-modulated pulses, d. The variation of the fundamental of the PWM wave, d, is represented in Figure 5. As a result of this process, the modulating wave has a constant amplitude while each sample is being taken, and consequently the widths of the pulses are proportional to the amplitude of the modulating wave at uniformly spaced sampling times -- hence the terminology "uniform" or "regular" sampling.

It is an important characteristic of regular sampling that the sampling positions and sampled values can be defined unambiguously, such that the pulses produced are predictable both in width and position. It is therefore possible to define the width of a pulse in terms of the sampled value of the modulating wave taken at time t_j. Thus:

$$t_{pj} = (1 + M\sin(\omega_m t_j))\ T/2 \qquad (2.1)$$

where: t_{pj} is the pulse width at the sampling instant t_j

T is the period of the carrier signal

M is the amplitude of the modulating signal

The first term in this equation corresponds to the unmodulated carrier-frequency pulse width, and the second term corresponds to the sinusoidal modulation required at time t_j. This equation can be used to calculate the pulse widths directly, and forms the basis of the computer algorithm. This mode is therefore easily implemented using digital or microprocessor techniques. Both two-level and three-level regularly sampled PWMs can be generated, as in the case of naturally sampled PWM.

2.4.3 Optimized PWM

As discussed above, both naturally and regularly sampled PWM are generated using practical circuit implementations based on well-defined modulation processes. It is also possible to generate optimized PWMs by first defining a general PWM waveform analytically in terms of a set of switching angles. Based on the switching angles selected, the harmonic spectrum is defined. The analytical expression can be used in a variety of ways to produce PWM waveforms which are optimized with respect to particular performance criteria; e.g. the elimination of low-frequency harmonics, or the minimization of harmonic current distortion or peak current. The defined performance criterion results in a set of nonlinear equations in terms of the unknown switching angles. These equations can be solved using the mainframe computer and numerical minimization techniques to determine the optimized switching angles. These angles can subsequently be preprogrammed into the memory of the microprocessor controlling the inverter and used to generate the PWM waveform in real-time.

2.5 Generation of Naturally and Regularly Sampled Waveforms

2.5.1 Naturally Sampled PWM

As mentioned above, there are no analytic expressions for the switching points of naturally sampled PWM waves. Each switching point is implicitly defined through a nonlinear equation expressing the equality, at the switching point, of the carrier and the modulating sine waves. For a wave with a frequency ratio, R, the equation of the j^{th} downstroke (j^{th} falling edge, Figure 4) of the carrier in terms of the phase variable, ϕ, of the modulating wave is [12]:

$$y = 4j - 3 - (2R/\pi)\phi \tag{2.2}$$

and the j^{th} upstroke is:

$$y = 1 - 4j + (2R/\pi)\phi \tag{2.3}$$

The equation of a modulating wave of modulation depth M is:

$$y = M\sin\phi \tag{2.4}$$

The 2R switching points of the naturally sampled PWM wave are therefore given by the solutions of the 2R equations:

$$M\sin\phi = 4j - 3 - (2R/\pi)\phi \tag{2.5}$$

$$M\sin\phi = 1 - 4j + (2R/\pi)\phi, \text{ for } j = 1,2....R \tag{2.6}$$

These equations can be solved by Newton-Raphson iteration.

2.5.2 Regularly Sampled PWM

In regular symmetric PWM, the switching angles can be analytically specified. For a frequency ratio, R, the transitions to +1 occur at points:

$$\alpha_{2j-1} = ((4j - 3 - M\sin(2j-1)(\pi/R))(\pi/2R) \tag{2.7}$$

and to -1 at points:

$$\alpha_{2j} = ((4j - 1 + M\sin(2j-1)(\pi/R))(\pi/2R), \text{ for } j = 1,2...R \quad (2.8)$$

In regular asymmetric PWM also, the switching angles are definable by analytical expressions.

2.6 Harmonic Analysis

A periodic waveform may be represented as [10]:

$$y(\phi) = y_1\ (H(\phi) - H(\phi-\alpha_1)) + \sum_{j=2}^{n} y_j(H(\phi-\alpha_j-1)$$

$$- H(\phi-\alpha_j)) + y_1\ ((H(\phi-\alpha_n) - H(\phi-2\pi)), \text{ for } 0 \leq \phi \leq 2\pi \quad (2.9)$$

where $H(\phi)$ is the Heaviside unit function, i.e. a waveform, periodic with period 2π, containing, in the reference wavelength, n switching points $\alpha_1, \alpha_2, \ldots \alpha_n$ between each pair of which the waveform has a fixed constant level. The level between the switching points, α_{j-1} and α_j is y_j. The Fourier components of the waveform of equation (2.9) are given by:

$$A_m = (1/m\pi)[y(1)(\sin m\alpha_1 - \sin m\alpha_n) +$$

$$\sum_{j=2}^{n} [y(j)(\sin m\alpha_j - \sin m\alpha_{j-1})] \quad (2.10)$$

$$B_m = (1/m\pi)[y(1)(\cos m\alpha_1 - \cos m\alpha_n) +$$

$$\sum_{j=2}^{n} [y(j)(\cos m\alpha_j - \cos m\alpha_{j-1})] \quad (2.11)$$

where n = number of switching points

m = harmonic number

α = switching angle.

The harmonic coefficients can be computed for any number of m.

2.6.1 Simulation of Three-Phase PWM Inverters

As we required the harmonic spectra produced by three-phase inverters to study time harmonic effects (see Chapter 4), a capability to generate the output waveforms corresponding to a particular modulation strategy and to evaluate the harmonic spectra by digital computer was developed. The inverter line voltages can be generated by subtracting the appropriate pole voltages. As an example, the inverter line voltage corresponding to the two-level voltage shown in Figure 6(a) and a similar 120° phase shifted two-level voltage is illustrated in Figure 6(b). The corresponding phase voltage for a star-connected load can be generated using the relationship:

$$V_{ph} = (2V_a - V_b - V_c)/3 \qquad (2.12)$$

where V_a, V_b, and V_c are the pole voltages. The results of this operation are shown in Figure 6(c). The comparison of harmonic spectra of pole, line and phase voltages, as shown in Figure 7, demonstrates that the carrier frequency harmonics are eliminated in the three-phase connection when a single-phase carrier is used for all three phases, and when a triple-integer frequency ratio is used. Note also that the percentage harmonic content of the line and phase voltages are the same.

2.7 Simulation of 200 kVA Inverter System

A Reliance 200 kVA inverter was used for the experimental evaluation of time harmonic effects in LIM drives. This inverter is equipped with a regulator system that acts on the three-phase power bridge to adjust inverter output frequency and to provide automatic V/Hz control. Output voltage compensation produces high-quality waveforms with low harmonic content. The controller has the ability to adjust the inverter bridge over a frequency range of 0 to 200 Hz, within the operating limits of maximum commutation rate and minimum modulation notch-width constraints. A brief description of these constraints will enable one to understand the PWM strategy employed and the subsequent harmonic analysis of the inverter output waveforms.

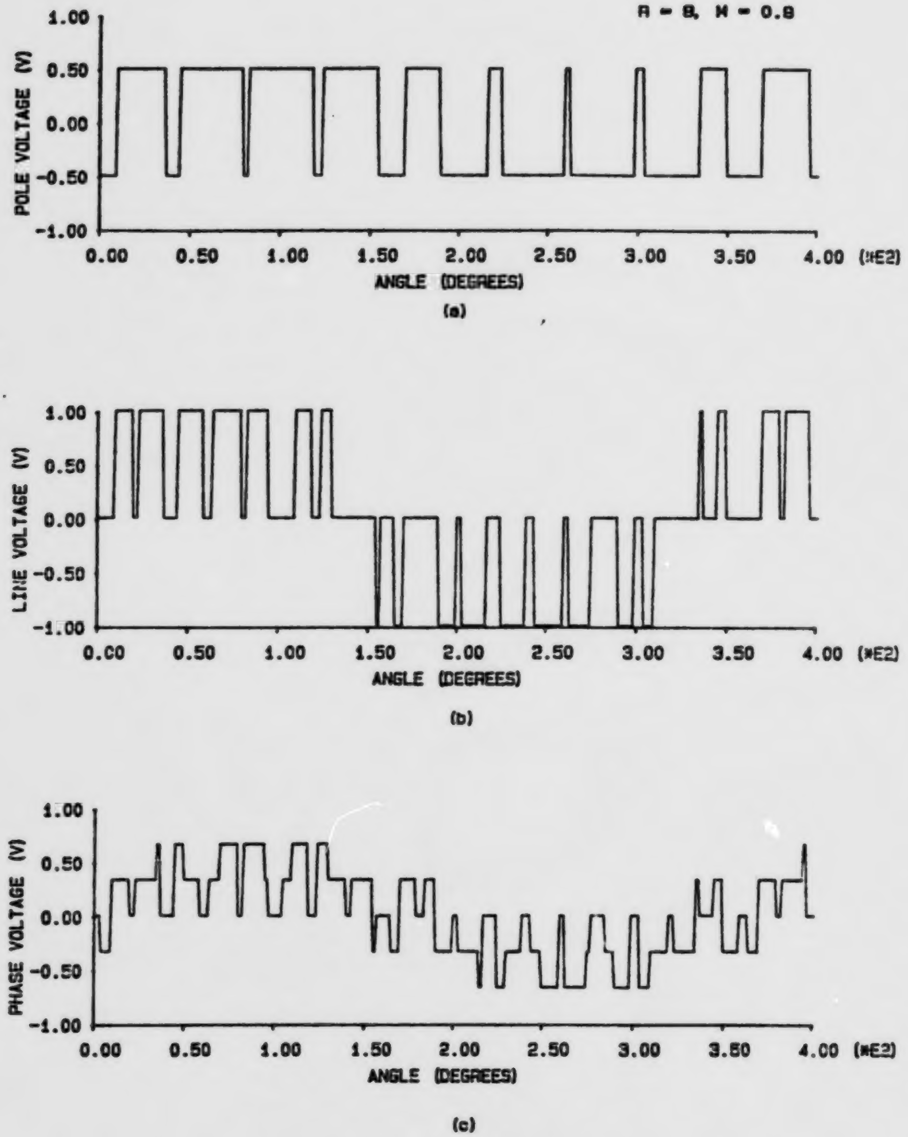

$$R = \frac{\text{frequency of carrier signal}}{\text{frequency of modulating signal}}$$

$$M = \frac{\text{amplitude of modulating signal}}{\text{amplitude of carrier signal}}$$

Figure 6 Output voltage waveforms:
(a) pole voltage
(b) line voltage
(c) phase voltage

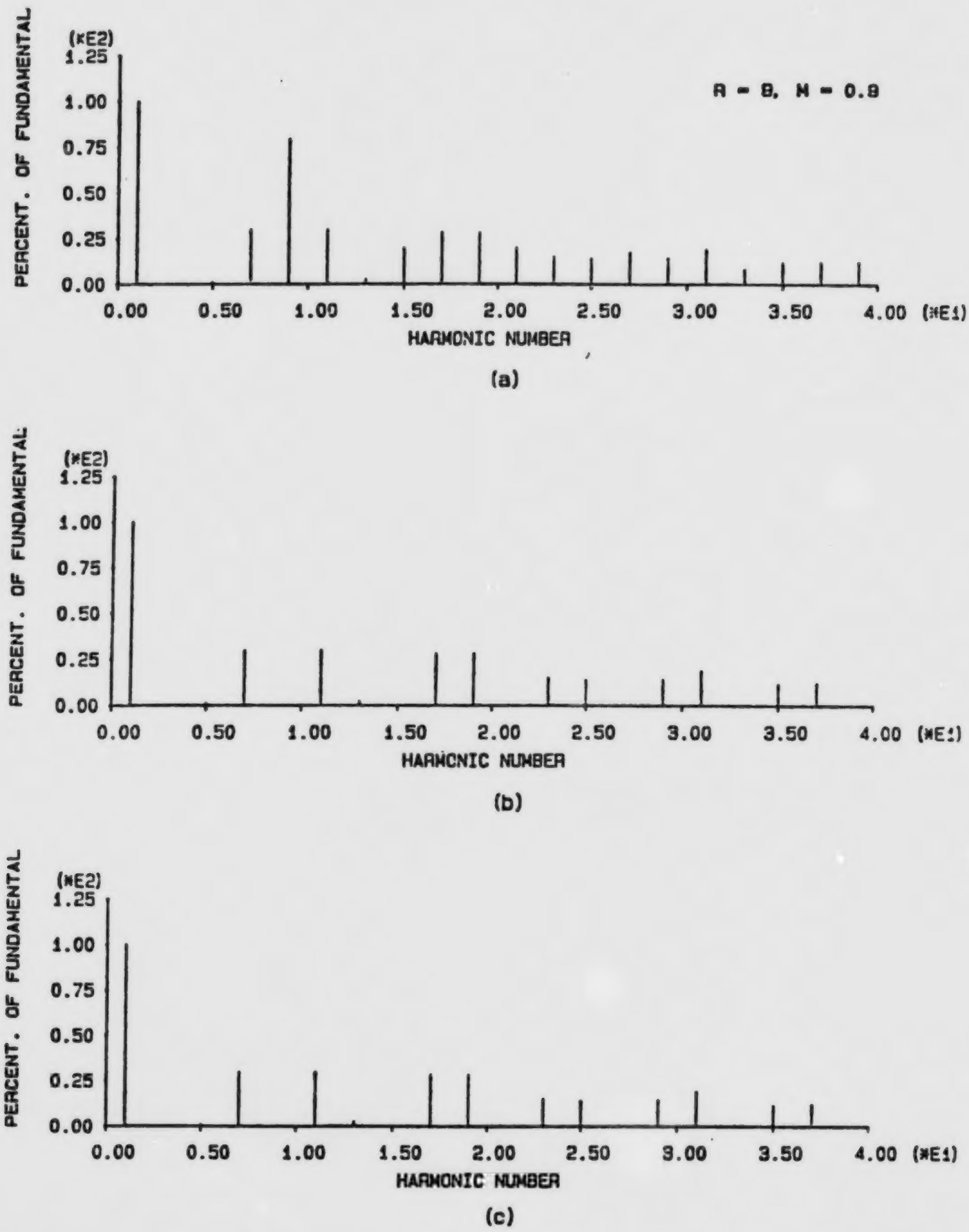

Figure 7 Harmonic spectra of the naturally sampled waveforms:
(a) pole voltage
(b) line voltage
(c) phase voltage

2.7.1 Commutation Rate and Frequency Ratio Control

When a PWM inverter is used as a power supply for a variable-frequency, variable-speed drive, it is desirable that the carrier be synchronized to the modulating signal and that the ratio of the two frequencies be chosen to maintain the highest possible inverter frequency consistent with reliable operation [16]. This requires that the ratio be changed as the drive speed changes and, for smooth operation, this must be accomplished without transients in the inverter output. The highest possible inverter frequency is set by the maximum commutation rate limitation imposed by switching losses and thermal considerations of the power bridge components. For the Reliance inverter, the maximum switching or commutation rate is 1000 Hz.

Consider a system with frequency ratios 3:1, 9:1, 15:1, 21:1 and 27:1, i.e. odd multiples of three, ratios which are desirable for a three-phase system. This frequency ratio control requirement can be represented graphically as in Figure 8. Also shown are the maximum value of the carrier frequency, R_{max} (determined by the maximum operating frequency of the inverter), and the minimum carrier frequency, R_{min}, below which operation is undesirable (but necessary at high motor speeds), due to the harmonic content in the PWM output causing large motor losses. In Figure 8, R_{max} is taken as 1200 Hz and R_{min} as 600 Hz. For an output frequency of 200 Hz, it is seen that the maximum possible ratio is 3 with the carrier at 600 Hz. As the output frequency is reduced, the carrier frequency is correspondingly reduced. At, for example, an output of 140 Hz, the carrier would be at 420 Hz. This whole high frequency range represents poor operating conditions so that at an output frequency of 140 Hz, a frequency ratio of 9 is now selected, giving a carrier frequency of 1260 Hz. The other output switching frequencies are chosen to be at 80, 57.14 and 44.44 Hz so that the carrier frequency switches up to 1200 Hz. The lower carrier switching frequencies are at 720 Hz, 857 Hz, and 933 Hz (i.e. all above 600 Hz), as shown in Figure 8.

2.7.2 Mimimum Notch Width

Modulation limitations define the minimum time for a given inverter output line to switch from one dc bus to the other and back. A pulse or notch is generated by two successive switches of a given thyristor

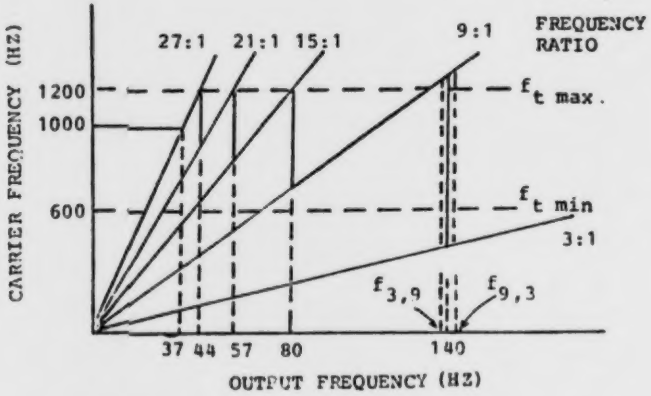

Figure 8 Frequency control of PWM inverters

pair. For the Reliance inverter [17], the minimum allowable notch-width is 176 microseconds. Referring to Figure 9(a), it can be seen that the phase A waveshape is being generated with a 176 microsecond notch within the time intervals t_1 and t_3. There are similar conditions in both phase B and phase C generated waves. The resulting line-to-line waveform represents an ac voltage of a given fundamental frequency. If the inverter output voltage were to increase under these operating conditions, it would require the generation of a pulse and notch in each phase output of less than the minimum allowable duration. This necessitates the use of less sophisticated wave shapes (modulating signal) above a given operating frequency. Likewise, any attempt to increase inverter output frequency at constant voltage would be unacceptable with the above waveshape.

The regulator allows the generation of an unmodulated 6-step waveform, together with symmetrically pulse-width-modulated 6-, 12- and 24-step waveforms. An adaptive waveform control circuit monitors the two constraints described above, and selects the proper carrier ratio so as to produce the best inverter waveform possible within the operating limits of bridge components. It also determines whether a 6-, 12- or 24-step waveshape will be produced, depending on the notch-width constraint.

2.7.3 Generation of the Output Waveform

In the pulse-width modulator, the 6-, 12- and 24-step modulated waveforms are generated using an analog V/Hz signal and a triangular carrier signal. The two signals are compared within the modulator by the action of four comparators. The switching level of each comparator is set at a predetermined fraction of the V/Hz signal magnitude. The output of the PWM, i.e. four pulse trains, a, b, c and d, shown in Figure 9(b), are synchronized with the carrier wave, but with differing relative duty cycles (ratio of pulse to notch-width).

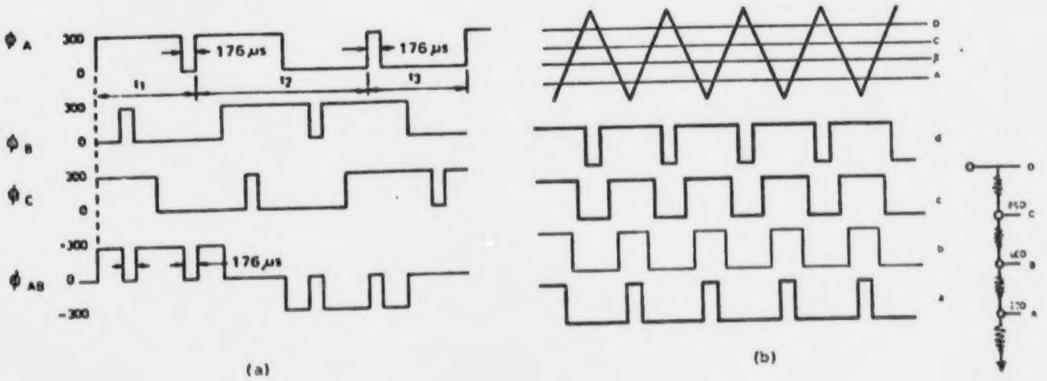

Figure 9 Reliance inverter waveforms: (a) minimum notch-width, (b) generation of modulated pulse trains

In generating a 24-step waveform, all the reference pulses are utilized. Pulses, a, b and c, are each applied for 15° of the inverter output waveform and d is applied for 90°. For 12-step generation, signals b and d only are applied. The method explained above is employed for the digital simulation of the PWM waveforms.

The PWM model can be combined with an electrical machine model to simulate the dynamic operation of a variable-speed drive system; or alternatively it can be combined with a filter-load model and feedback control to simulate voltage regulating systems.

2.7.4 Verification of the Harmonic Spectrum of the Inverter

For the time harmonic test program reported here, the inverter was operated at a frequency of 60 Hz, from 200 V to 400 V, using a Y-connected LIM load. As the output voltage is increased, the adaptive waveform control selects the proper waveform and carrier ratio, depending on the operating point. For line-to-line voltages of 200 V, 300 V and 400 V, the harmonic spectra of line voltages were measured using a power spectrum analyzer (HP 3582A). Also, the carrier ratio and value of the V/Hz signal were noted in each case. These values were used by the simulation program, and the harmonic spectra were then generated using the Fast Fourier Transform (FFT) technique taking 512 samples per cycle. The spectra for two of the output waveforms are shown in Figure 10. It was found that the generated spectra were very similar to those measured directly from the inverter output, as shown in Figure 11. As noted previously, since the percentage harmonic content of the line and phase voltages are the same, the harmonic content of the phase voltages can be obtained directly from the line voltage spectra.

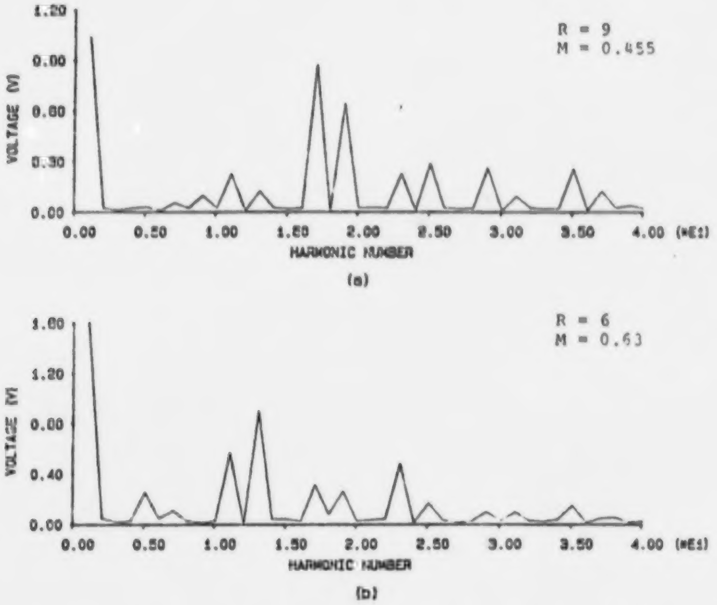

(Note that the above spectra are represented by simple linear interpolation between amplitudes at each harmonic number.)

Figure 10 Computed harmonic spectra of the inverter waveforms: (a) V_{LL} = 200 V, (b) V_{LL} = 300 V

It has therefore been shown that the inverter output waveform can be accurately simulated by computer for a particular modulation strategy, and that the harmonic content of LIM excitation voltages can be analytically derived in good agreement with those observed experimentally.

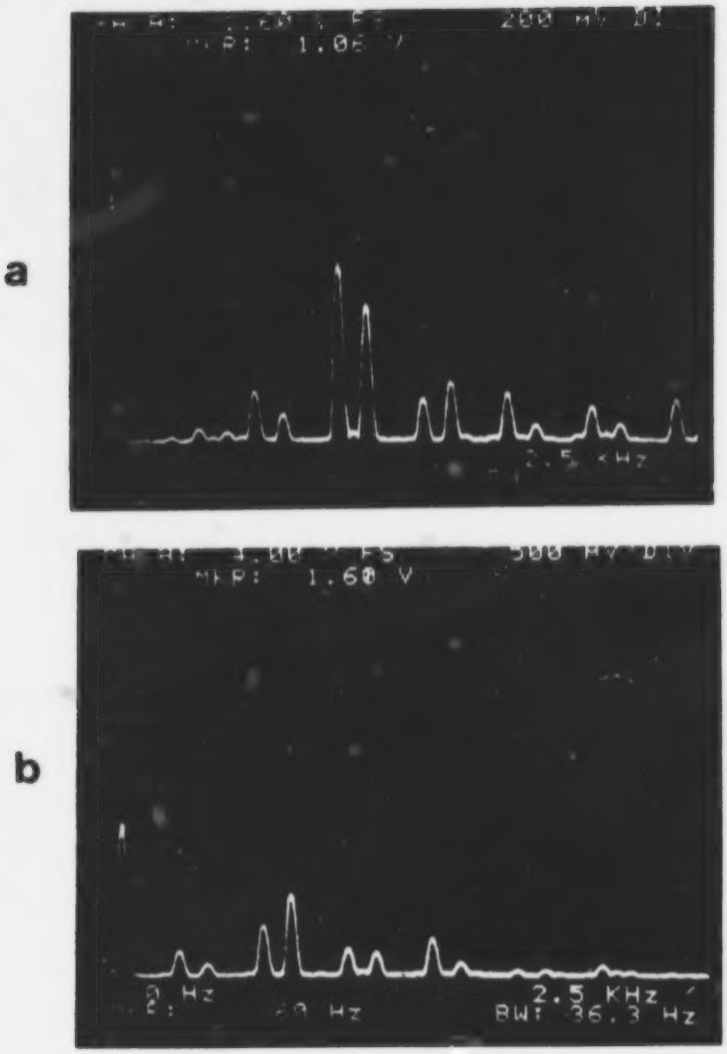

R = 9

M = 0.455

R = 6

M = 0.63

In the above traces, the following information is given:

MKR:	position of marker along frequency axis and amplitude of signal at that frequency
BW:	bandwidth, i.e. frequency resolution limit
0-2.5 kHz:	range of analysis

Figure 11 Measured harmonic spectra of the inverted waveforms:
(a) V_{LL} = 200 V
(b) V_{LL} = 300 V

3. HARMONIC BEHAVIOUR OF ROTARY INDUCTION MACHINES

3.1 Introduction

Before discussing time harmonic effects in linear induction motors, the effects in conventional rotary drives will be reviewed. A simulation of the harmonic performance of a rotary induction motor will then be presented.

The increasing use of variable-frequency drive systems has resulted in new application problems relating to the performance of an induction motor. One problem of importance in the application of a rectifier-inverter induction motor drive is that of system instability which may occur at low frequencies. It can be shown that instability can occur over a wide speed range if the system parameters are improperly selected [18]. Other problems are related to the fact that most solid-state variable frequency power supplies provide a voltage source that is rich in harmonics. One obvious concern is the resulting increase in losses. This problem has been discussed in detail by Klingshirn and Jordan [19] who used an analysis based on a Fourier series approach in which the motor is modelled by the conventional equivalent-T circuit for each of the harmonic frequencies, using the appropriate value of slip for each frequency. Such circuits are adequate if the motor is operated in the magnetically linear region. It may however be desirable to drive the motor well into saturation, temporarily, to obtain maximum torque for a given frame size. Means for predicting the voltage and current harmonics under saturated conditions have been examined by Slemon and Dewan [20].

Another concern which can prove equally troublesome is the pulsation of rotor speed due to the voltage harmonics applied to the machine when driven from an inverter supply. In applications for which uniform speed of rotation is mandatory, such as machine tools, it is important to establish a method for evaluating the magnitude of these speed oscillations. This problem differs from that of system instability in that the torque pulsation and the resulting speed oscillation are natural consequences of the inverter voltage waveshape rather than a result of an improper choice of system parameters. While the system instability can be overcome by a suitable choice of parameters, the steady-state torque pulsations cannot be eliminated. In many cases these torque pulsations define the lower limit of the speed range which yields satisfactory system performance.

In previous studies, considerable attention has been given to calculating these electromagnetic torque harmonics. Jain [21], by neglecting stator resistance, has established a general equation for the average torque for an arbitrary balanced set of applied voltages. Lipo and Krause [22,23] have developed the dq axis representation of several types of inverter-driven induction machines for both transient and steady-state operation.

3.2 Nature of Input Waveforms

Typical waveforms of voltage-source inverters are shown in Figure 12. Figure 12(a) shows the classical six-step waveform, while the waveform of 12(b) exhibits the high frequency chopping effects of typical PWM inverters. It is evident from the waveforms that they contain a host of higher harmonics in addition to the fundamental. Many other combinations of waveforms are possible depending upon the design of the inverter. However, certain common features are found in all of these waveforms, namely they are periodic, having a finite number of maxima and minima and discontinuities within a given period. The harmonic analysis of such waveforms has been discussed in Chapter 2.

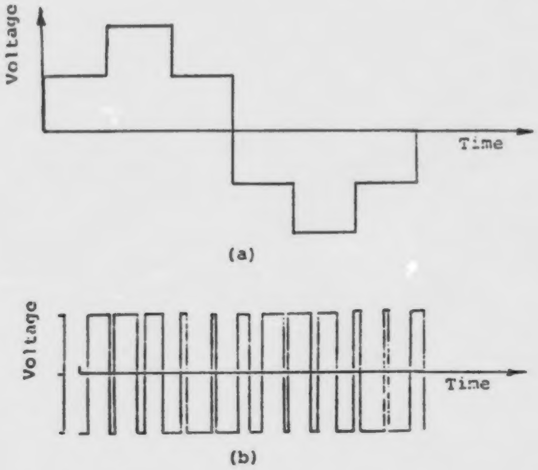

Figure 12 Typical waveforms of a voltage source inverter:
(a) six-step inverter
(b) PWM inverter

3.3 Harmonic Equivalent Circuits

When an ac motor is operated with a non-sinusoidal supply, the stator voltage can be analyzed into a fundamental component and a series of harmonics. If magnetic saturation is neglected, the motor may be regarded as a linear device, and the principle of superposition can be applied. This means that the motor behaviour can be analyzed independently for the fundamental and for each harmonic content of excitation. The overall response to the non-sinusoidal voltage is then obtained as a summation of the responses to the individual components. Hence, the net motor current or torque is equal to the sum of the current or torque contributions of each voltage components in the supply waveform. Analysis of the performance of the motor can then proceed as if there were a series of independent harmonic sources all connected in series supplying the motor.

The equivalent circuit used is the well-known equivalent T, with core loss and saturation effects neglected. X_1 and X_2 are the stator and rotor leakage reactances at the supply frequency, and X_m is the corresponding magnetizing reactance. The k^{th} harmonic slip, s_k, in terms of fundamental slip, s_1, is given by:

$$s_k = ((k \mp 1) \pm s_1)/k \qquad (3.1)$$

The fundamental equivalent circuit of Figure 13 may be adapted for the k_{th} harmonic voltage and current as shown in Figure 14(a). From equation (3.1) it can be noted that there is very little variation in s_k for normal motor operation. If the motor speed varies from synchronous speed to standstill, the fundamental slip, s_1, varies from 0 to 1, but the fifth harmonic slip, s_k, only varies from 1.2 to 1. For higher harmonics, s_k is even closer to unity. The harmonic equivalent circuit of Figure 14(a) can therefore be simplified to a good approximation as shown in Figure 14(b). Since s_k is close to unity, the effective rotor resistance can be neglected in comparison with the reactance, kX_2 at harmonic frequencies. The shunt magnetizing reactance is much greater than the rotor leakage reactance and can be omitted. The motor impedance presented to the harmonic currents is therefore approximately $k(X_1+X_2)$.

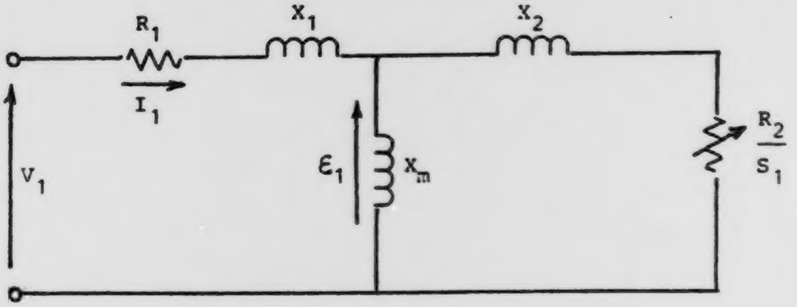
R1
X1
X2
I1
V1
ε1
Xm
R2/s1

Figure 13 Fundamental frequency equivalent circuit

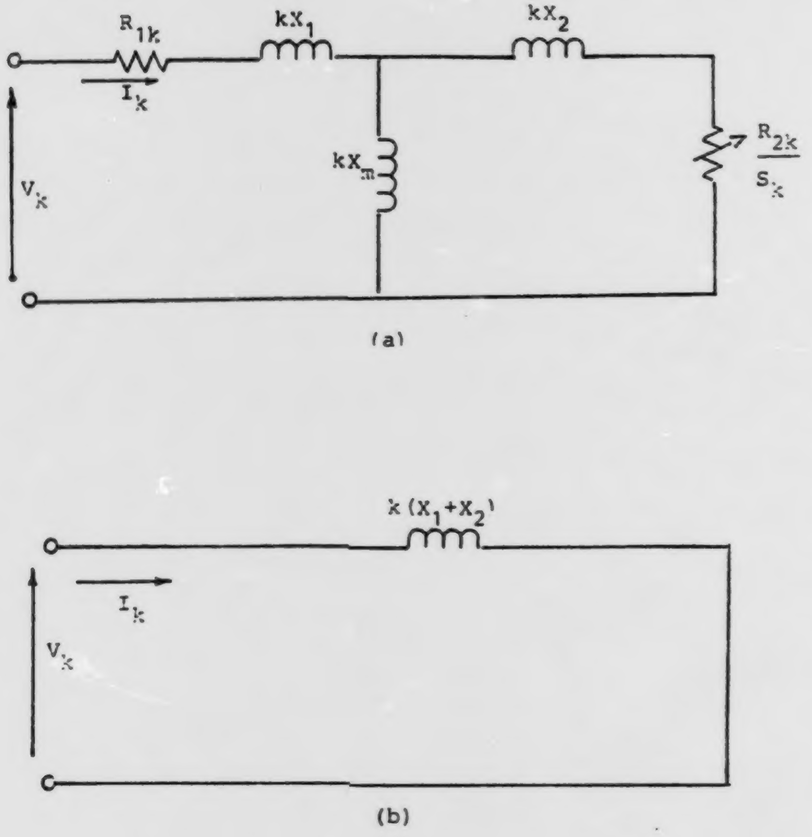
R1k
kX1
kX2
Ik
Vk
kXm
R2k/sk
k(X1+X2)
Ik
Vk

(a)

(b)

Figure 14 Equivalent circuit for harmonic current calculation

In order to arrive at appropriate values for the inductances in the circuit with the motor operating on nonsinusoidal voltage, the effects of harmonic voltages and currents on the degree of saturation of the iron must be taken into account. It may be note that:

- Experimental tests at no-load indicate that the fundamental component of magnetizing current is larger when harmonics are present, indicating a reduced value of L_m. Also, the measured amplitudes of harmonic currents provide evidence of lower values of leakage inductances when harmonics are present. It can be shown that when time harmonics are present, the peak of the rotating flux density varies, but its time average value is the same as without harmonics [19]. If the voltage is such that the operation is near the knee of the saturation curve, the no-load current will be correspondingly increased.

- A major contributing cause of the reduction in inductances is the increased leakage flux produced by the harmonic currents, resulting in higher saturation of portions of the magnetic circuit. The change in the amount of saturation is related to the instantaneous sum of all the harmonic currents, and in particular to the peak amplitude of this sum. Precise calculation of the effect of magnetic saturation is complex and a semi-empirical method is adequate to calculate a saturated value of L_m for nonsinusoidal excitation. The equivalent per-phase voltage can be approximated as [19]:

$$V_{eq} = V_1 \, (1 + C_f \times H_f) \qquad (3.2)$$

where: V_1 is the fundamental voltage

H_f is the harmonic factor [19]

C_f is an empirical factor equal to 0.5.

Then, with a no-load saturation curve for sinusoidal excitation available, the no-load current at this equivalent voltage is found, and from this, L_m can be computed. The leakage inductances are also influenced by these harmonic current peaks. Lower leakage inductances of from 15 to 20 percent are common for typical nonsinusoidal waveforms.

3.4 Harmonic Currents

Since s_k is nearly unity for all significant higher harmonics at all motor speeds from standstill to synchronism, the harmonic equivalent circuit of Figure 14(b) is practically independent of motor speed. Thus, harmonic currents remain approximately constant for all operating conditions of the motor from no-load to full load, and even down to standstill. The fundamental stator current is determined by the motor loading and, as a result, the relative harmonic content of the machine current is considerably greater for light-load operation than for full-load or starting conditions. Consequently, there is a significant increase in the no-load losses of the machine as compared with normal sine wave operation.

The approximate equivalent circuit of Figure 14(b) is similar to that used for normal sinewave calculations with a locked-rotor induction motor, when the motor current is also limited by the total leakage reactance ($X_1 + X_2$). The standstill or starting behaviour of the induction motor on a sinewave supply is therefore a measure of its harmonic performance. If the motor draws a large starting current, it will also draw substantial harmonic currents on non-sinusoidal supplies. If the motor has a very low leakage reactance, it should be used with caution on non-sinusoidal supplies, as excessive harmonic currents may flow and overheat the motor.

There is, of course, some lower limit of the fundamental frequency below which these approximations are no longer valid. If operation at very low frequencies, for example below 10 Hz, is being considered, the complete harmonic circuits of Figure 14(a) should be used for performance evaluation.

3.5 Motor Losses

An induction motor operated with non-sinusoidal supply voltage has the usual fundamental motor losses (i.e. stator and rotor copper and magnetic core losses). Additional losses appear due to the harmonic excitation [24].

3.5.1 Stator Copper Loss

The presence of harmonic currents in the stator windings causes an increased I^2R loss. If m is the number of stator phases and R_1 is the stator resistance per phase, the total stator copper loss becomes:

$$P_1 = m(I_1^2 + I_{har}^2)R_1 \qquad (3.3)$$

where I_1 is the fundamental current. The second term represents the harmonic copper loss. The presence of harmonic currents also increases the fundamental term slightly, due to the increased magnetizing current already described. For samll motors, skin effect at higher harmonic frequencies may be neglected. For large motors, when stator conductors have appreciable depth, skin effect should be taken into account.

3.5.2 Rotor Copper Loss

The rotor copper loss can, in many cases, be the largest loss directly attributable to the harmonic currents. It is appreciably increased for deep-bar rotors, due to the large skin effect at the rotor harmonic frequencies. At these frequencies, the rotor resistance is much greater than the dc value. The actual increase depends on the geometrical shape of the conductor cross-section and the rotor slot in which it is placed. Alger has presented curves for the factor by which the resistance is increased. Because of the variation of rotor resistance with frequency, the loss due to each harmonic current must be considered separately. For the k^{th} harmonic, the loss is:

$$P_{2k} = m(I_{2k})^2 R_{2k} \qquad (3.4)$$

where I_{2k} is the kth harmonic current, and R_{2k} is the corresponding rotor resistance, corrected for skin effect.

3.5.3 Core Loss

The stator core loss is a function of flux density in the stator core. It is larger with non-sinusoidal excitation due to the higher peak flux density previously discussed. The overall increase in core loss due to time harmonic main fluxes is a negligible part of the total iron loss. However, the end-leakage and skew-leakage fluxes, which normally contribute to the stray-load loss, may produce an appreciable core loss at the harmonic frequencies. Consequently, while no simple empirical expression is available for harmonic core losses, these effects must be taken into consideration when operating an induction machine on non-sinusoidal supplies.

3.6 Motor Efficiency

The magnitude of the harmonic losses obviously depends on the harmonic content of the applied voltage. Large harmonic voltages cause increased machine losses and reduced efficiency. However, most inverters do not generate harmonics of lower order than the fifth and the higher-order harmonics have smaller amplitudes. The approximate values of the three-phase, six-step voltages having a fundamental component equal to the rated sine-wave voltage of the machine are discussed below [24,25].

For a typical medium power induction motor, under six-step voltage excitation, the full load rms current is approximately 4 percent greater than the fundamental component. If skin effect is neglected, the motor copper loss is proportional to the square of the total rms current, and the harmonic copper loss is therefore 8 percent of the fundamental loss. Allowing an average threefold increase in rotor resistance due to skin effect at harmonic frequencies, the harmonic copper loss in the motor can be conservatively estimated at 24 percent of the fundamental loss. If the copper loss constitutes 50 percent of the total machine loss, this causes an increase of approximately 12 percent in the overall machine loss.

The increase in core loss is less predictable, as it is influenced by machine construction and the magnetic materials used. If the higher order harmonic content of the stator voltage waveform is low, the harmonic core loss should not exceed 10 percent. If the iron loss and stray-load loss constitute approximately 40 percent of the machine losses, then the harmonic contribution to the total machine losses is only 4 percent. Friction and windage losses are unaffected, and consequently the overall increase in the motor losses due to harmonic supplies is generally less than 20 percent. If the motor has a normal efficiency of 90 percent on a sinusoidal supply, the presence of harmonics increases the machine losses from 10 to 12 percent, and the overall motor efficiency falls typically by only 2 percent.

Thus the additional losses arising from the higher harmonic content of non-sinusoidal waveforms act as a marginal detriment to the efficiency of inverter-fed induction motors. Figure 15 [25] shows the typical efficiency ranges of standard three-phase, four-pole induction motors with excitation from 60 Hz mains and with typical non-sinusoidal excitation from inverter sources. It should be noted, however, that actual efficiencies may vary appreciably with the manufacturers of both the induction motor and the inverter supplies.

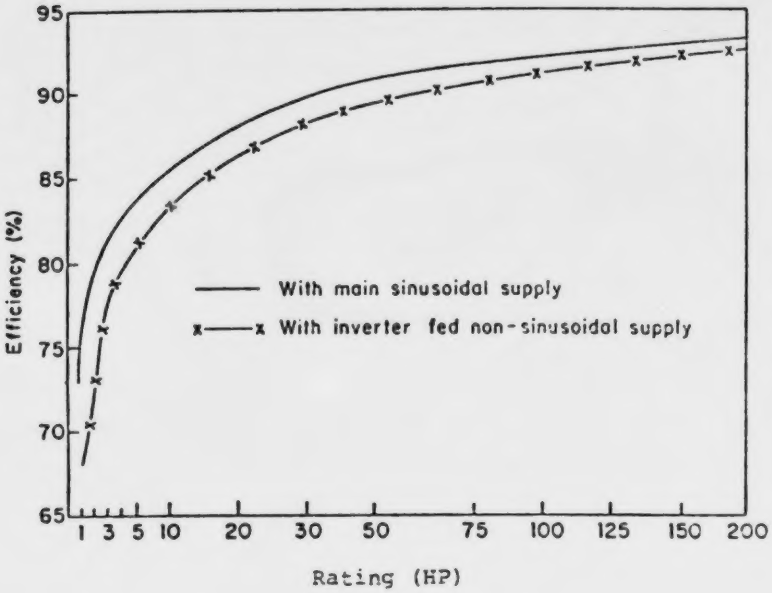

Figure 15 Efficiency of medium hp induction motors

3.7 Harmonic Torques

The presence of time harmonic mmf waves in the airgap of an induction motor results in harmonic torques on the rotor. These torques are of two types [24]:

- steady harmonic torque
- pulsating harmonic torque.

In an ideal symmetrical three-phase machine, the triplen harmonics cannot produce net airgap flux, and hence it is necessary to consider only harmonics of order $(6n\pm1)$. If the inverter supplies balanced voltages to the machine, each $(6n-1)^{th}$ harmonic produces a flux rotating in the opposite direction to that produced by the fundamental, while each $(6n+1)^{th}$ harmonic produces a flux rotating in the same direction as the fundamental.

Torque can be considered to be produced by the interaction between the mutual flux and the rotor MMF vectors. Constant or steady torques are developed by the reaction of harmonic airgap fluxes with harmonic rotor currents of the same order. This is because the angle between the flux and the current of the same harmonic remains constant under steady-state conditions. However, these steady harmonic torques are a very small fraction of the rated torque, and have negligible effect on the motor operation. This may be verified by calculating the torque contribution from the harmonic equivalent circuit.

Pulsating torques are produced by the reaction of harmonic rotating fluxes with fundamental and harmonic rotor currents of a different order, i.e. when the flux of one frequency interacts with the rotor mmf of another frequency, the relative angle varies as the difference between the speeds of the two rotating vectors and pulsating torques are produced. The principal pulsating torques arise from the interaction between the fundamental rotating flux and the harmonic rotor currents.

Fifth harmonic stator currents, for example, form a negative sequence set and produce a space mmf wave which rotates at five times the fundamental synchronous speed in the opposite direction to the fundamental field. The rotor currents induced by this time harmonic field react with the fundamental rotating field to produce a pulsating torque at six times findamental frequency, since the relative speed of the rotor current wave and the fundamental mmf wave is six times synchronous speed. The seventh harmonic stator current also produces a pulsating torque at six times fundamental frequency. The seventh harmonic has positive phase sequence and therefore produces a time harmonic field rotating at seven times synchronous speed in the same direction as the fundamental field. The relative speed of the main airgap field and the harmonic current wave in the rotor is again six times fundamental frequency. The two pulsating torques at six times fundamental frequency combine to produce a fluctuation in the electromagnetic torque developed by the motor. The transient and sixth harmonic torque developed on start-up of a typical induction machine by a six-stepped waveform is shown in Figure 16. This was obtained using a digital simulation model of the machine. The instantaneous value of the applied voltage was computed as $V_1 \sin \omega t + V_5 \sin 5 \omega t + V_7 \sin 7 \omega t$, where V_1, V_5, and V_7 are the peak values of the fundamental, fifth, and seventh harmonics respectively. Similarly, the eleventh and thirteenth harmonics in stator current produce a twelfth harmonic pulsating torque.

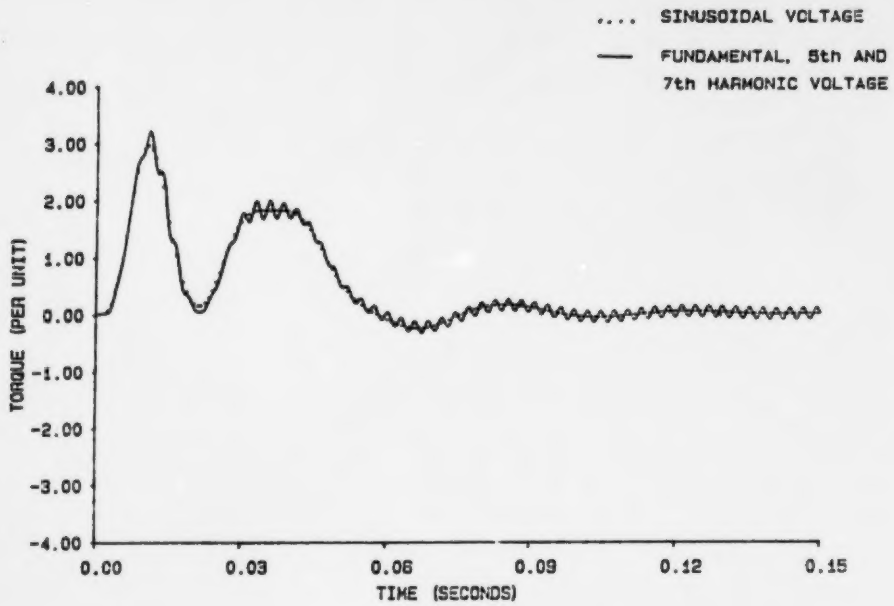

Figure 16 Sixth harmonic torque pulsation

If a PWM inverter with a low switching frequency is employed, severe torque pulsations can occur at the switching frequency. Their presence can cause the angular speed of the rotor to vary during a revolution. At very low speeds, the motor revolution may take place in a series of jerks or steps, and the presence of these pulsating torques may set a lower limit to the useful speed range of the motor. The point at which the speed pulsations become objectionable in a variable-speed drive depends on the inertia of the rotating system and the nature of the application.

This review of the known effects of time harmonics in rotary induction drives, provided a base from which linear induction could be studied. Clearly, similar effects are anticipated in LIMs. The relative significance of these effects will, however, be influenced by the specific geometry of the LIM. Analytical and experimental results on time harmonic effects in LIM's are presented in the next chapter.

4. TIME HARMONIC EFFECTS IN LINEAR INDUCTION DRIVES

4.1 Analysis

The contribution of higher time harmonics to core and copper loss in rotary machines has been evaluated both analytically and experimentally by many investigators [19,24,26], and has been discussed in Chapter 3. The effect of time harmonics produced by the power-conditioners on thrust and normal force in an LIM had not been investigated in detail. Very few papers in the literature have examined this aspect of LIM operation [27, 28]. To study this problem, a computationally efficient and accurate method using electromagnetic theory for calculating the performance of a SLIM with a double-layer secondary and excited from a power-conditioner was developed.

The method of analysis is described in Appendix A. In this published paper, the analysis of an LIM with double-layer secondary is presented for the fundamental time harmonic and for the full spectral distribution of space harmonics in the machine. It has been shown that a PWM waveform may be disassociated into harmonic components. The mechanical performance of an LIM with PWM excitation can then be determined by evaluating and summing the force due to each harmonic component [29].

In using the analysis in Appendix A, it should be noted that, for time harmonics of order n, only those of order $n = 6k \pm 1$ for $k = 0, 1, 2, \ldots$ exist for a y-connected machine with floating neutral.

. $n = 6k + 1$ produces forward travelling fields with slip s_n+ :

$$s_n+ = 1 - (1-s)/n$$

. $n = 6k - 1$ produces backward tunnelling fields with slip s_n-:

$$s_n- = 1 + (1-s)/n$$

4.2 Computation

On the basis of the analysis presented in Appendix A, a computer program for calculating the performance of an LIM with double-layer secondary was established. The magnetic properties of solid steel reaction rail are specified by twelve points on the magnetization curve (B vs H) and stored in a look-up table. Firstly, all slip independent parameters are calculated. Iterative loops are included for calculation of airgap, EMF, and magnetic field intensity, H, at the surface of the rail steel core, as indicated in the flow chart of Figure 17.

Initially, H is taken to be equal to the line current density of the primary, according to equation (A.15) in Appendix A for $n = 1$. This represents the highest possible value (for zero slip). After computation of the electromagnetic field distribution and of the equivalent circuit impedances, H is iteratively brought to the correct value for any finite slip. The most appropriate relaxation factor for H was found to be 1, and the iteration was pursued until the change in H between successive iterations was less than 0.1 percent. The program computes the thrust and normal forces, for the fundamental and higher harmonic input voltages for each value of slip.

4.3 Experimental Machine

In order to validate this analytical approach for performance calculation of a SLIM with (a) aluminum-capped and (b) solid-steel reaction rail, the computed performance was compared with test results on a large-scale LIM, using the CIGGT test facility.

4.3.1 Test Equipment

The SLIM tests were conducted using a 7.6 m diameter rotating wheel, with rim speeds of up to 25 m/sec. The reaction rails were mounted on the vertical rim surface of the wheel. The SLIM primary was mounted in a six-component force balance, and its position relative to the secondary could be finely adjusted and monitored by means of inductive gap sensors. The SLIM had a curved pole face (to match the rail surface curvature), and was instrumented with the thermocouples and search coils to monitor the temperature distribution and magnetic state of the motor. The machine was designed for an evaluation of the use of SLIMs for integrated suspension and propulsion of vehicles [30]. Design data for the LIM, used as input parameters for performance computation, are listed in Table 1. The tests were conducted with solid-steel and aluminum-capped reaction rails, shown schematically in

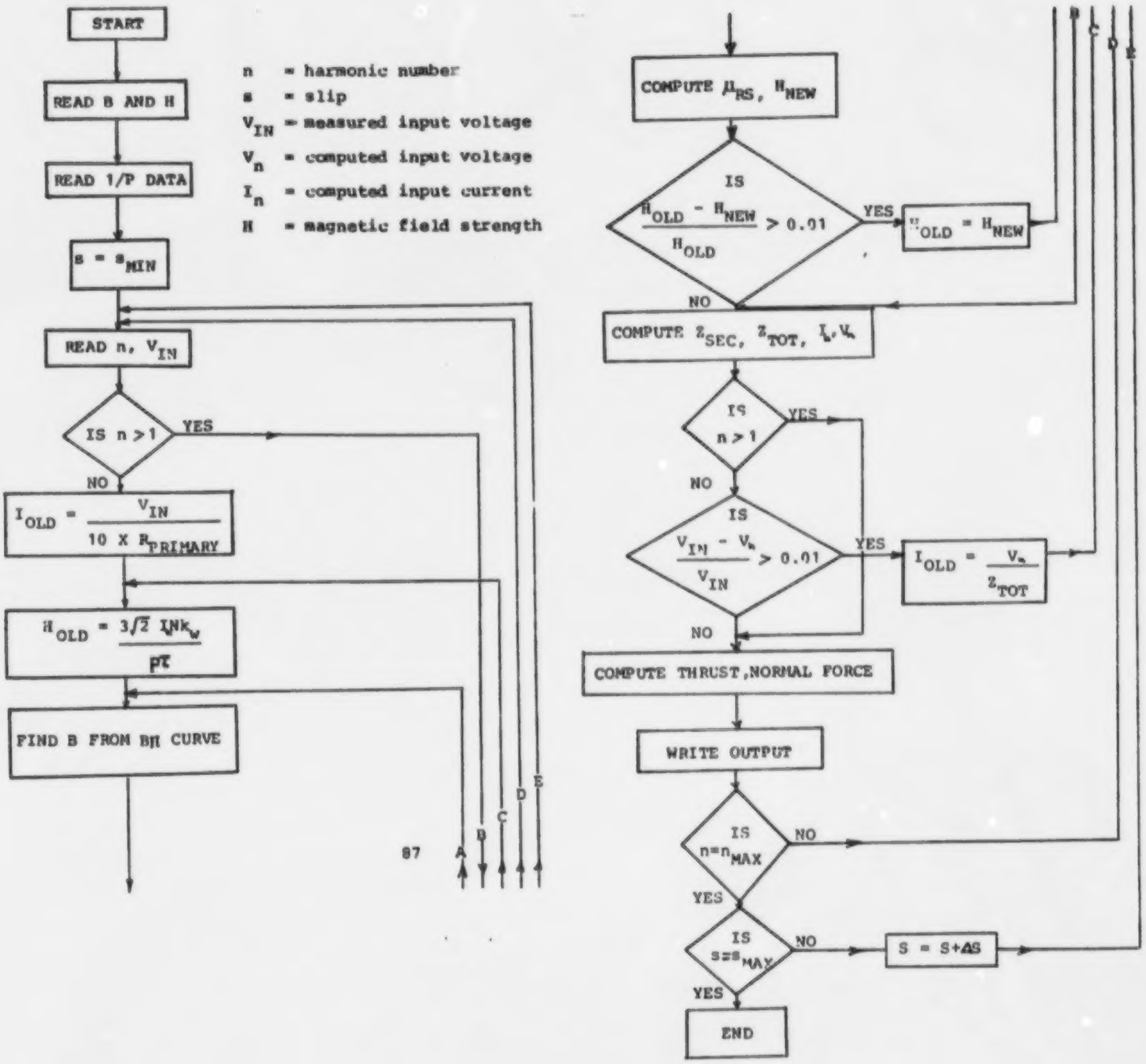
START
READ B AND H
READ 1/P DATA
$s = s_{MIN}$
READ n, V_{IN}
IS n > 1
YES
NO
$I_{OLD} = \frac{V_{IN}}{10 \times R_{PRIMARY}}$
$H_{OLD} = \frac{3\sqrt{2}\, INk_w}{p\tau}$
FIND B FROM BH CURVE
87
A
B
C
D
E
n = harmonic number
s = slip
V_{IN} = measured input voltage
V_n = computed input voltage
I_n = computed input current
H = magnetic field strength
COMPUTE μ_{RS}, H_{NEW}
IS $\frac{H_{OLD} - H_{NEW}}{H_{OLD}} > 0.01$
YES
$H_{OLD} = H_{NEW}$
NO
COMPUTE Z_{SEC}, Z_{TOT}, I_n, V_n
IS n > 1
YES
NO
IS $\frac{V_{IN} - V_n}{V_{IN}} > 0.01$
YES
$I_{OLD} = \frac{V_n}{Z_{TOT}}$
NO
COMPUTE THRUST, NORMAL FORCE
WRITE OUTPUT
IS $n = n_{MAX}$
NO
YES
IS $s = s_{MAX}$
NO
$S = S + \Delta S$
YES
END

Figure 17 Flowchart for computation of thrust and normal force in LIM

Figure 18. The rails were mounted on the wheel rim in 2.5 m long curved sections, and were connected by full-depth welded joints.

TABLE 1

DESIGN PARAMETERS OF TEST LIM

Primary:	
number of phases	$m = 3$
number of pole pairs	$p = 3$
pole pitch	$\tau = 0.25$ m
width of primary stack	$L = 0.101$ m
number of slots per pole per phase	$q = 3$
coil pitch	$w_c = 0.1994$ m
number of series turns/phase	$N = 108$
nominal (mean) phase current	$I = 200$ A
nominal airgap	$g = 15$ mm
Secondary:	
width of solid-steel core	$W = 0.111$ mm
depth of solid-steel core	$h_{sec} = 25.4$ mm
thickness of aluminum cap over core	$d = 4.5$ mm
thickness of overhang	$t_{ov} = 12.7$
width of secondary overhang	$h_{ov} = 45$ mm
conductivity of aluminum cap (at 20°C)	σAl = 32.3 x 10^6 S/m

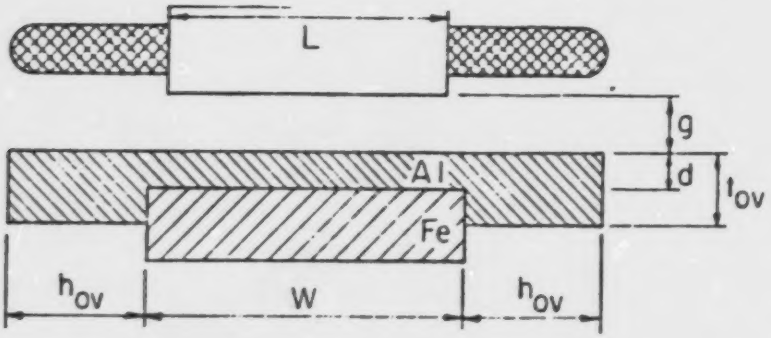

Figure 18 SLIM rail configuration

The SLIM was energized by:

- a 200 kVA, three-phase, variable-voltage auto transformer
- a Reliance 200 kVA, voltage source inverter drive, consisting of a rectifier, three-phase inverter bridge, and regulator. Fundamental output frequency was continously adjustable from 2 to 120 Hz, with voltage (fundamental rms line) up to 460 V, and a full load output current of 250 A.

In order to determine the performance of the SLIM over a wide range of steady-state operating conditions, a 64-channel microcomputer-based (PDP 11/03) data acquisition system (DAS) was used. Analog signals corresponding to the three-phase voltages and currents, frequency, wheel-speed, interaction forces, airgap and flux distribution in the machine were multiplexed into a 16-channel A/D converter. The sampled data was stored and processed to determine the rms of the fundamental components of the periodic quantities and the average values of other performance parameters.

4.3.2 Test Programs

In order to evaluate the effects of higher time harmonics, the SLIM was tested over a range of speeds and voltages at 60 Hz, employing both the PWM inverter and the sinusoidal source. Tests were conducted with both aluminum-capped and solid steel reaction rails under the following conditions:

. aluminum-capped secondary:	160 V and 200 V(L-L) at 60 Hz air gap = 15 mm aluminum thickness = 4.5 mm slip = 0.3-1.7
. solid steel secondary:	200 V, 300 V and 400 V(L-L) at 60 Hz air gap = 15 mm slip = 0.3-1.7

The 200 kVA transformer was used to excite the LIM with a pure sinusoidal voltage waveform of controllable magnitude. When using the inverter to drive the machine, the fundamental rms value of the input voltage was adjusted to the same value as the sinusoidal voltage excitation. This was achieved by observing the harmonic spectrum of the inverter output voltage waveform on a spectrum analyzer and adjusting the V/Hz control of the inverter until the required rms fundamental voltage was obtained. This method allowed the time harmonic effects to be separated from those attributed to the fundamental component of the excitation.

The tests were conducted only in the motoring and plugging regimes due to the maximum speed limitation (20 m/sec, as compared with a synchronous speed at 60 Hz of 30 m/sec) of the test wheel. For motoring tests, steady-state operation was achieved by counteracting the SLIM thrust by means of pneumatic brake on the test wheel. For plugging operation, a 110 kW dc motor, coupled to the wheel shaft through a gearbox, counteracted the SLIM braking action.

4.4 Comparison of Computed and Test Results

4.4.1 Time Harmonic Effects for Aluminum-Capped Rail

The computations were performed for the test conditions given in Section 4.3.2. The thrust and normal forces were calculated both for sinusoidal input voltage at 60 Hz and for a voltage provided by the PWM inverter having the same rms fundamental component. The PWM waveform and harmonic spectrum are given in Figure 19 for a phase voltage of 115.5 V rms (200 V rms line), and shows that for the particular modulation ratio used, the most significant harmonics are the 17th (72 percent of the fundamental) and 19th (55 percent of the fundamental). Figures 20 and 21 compare analytical and test results for thrust and normal forces as a function of speed at 60 Hz for two voltages (200 V and 160 V line-line). The calculated curves for sinusoidal and inverter excitation are virtually indistinguishable, and a similar overlapping was found for the measured thrust and normal force curves.

The calculated total thrust and normal forces due to odd higher time harmonics from $n = 5$ to 37 is very small, as is shown in Figure 22. For the same harmonic spectrum as in Figure 19, the net thrust is negative. The contributions of the forward and backward rotating fields of the higher time harmonic voltages (5 to 37) to the thrust are each shown in Figure 22. Note that the net harmonic forces are

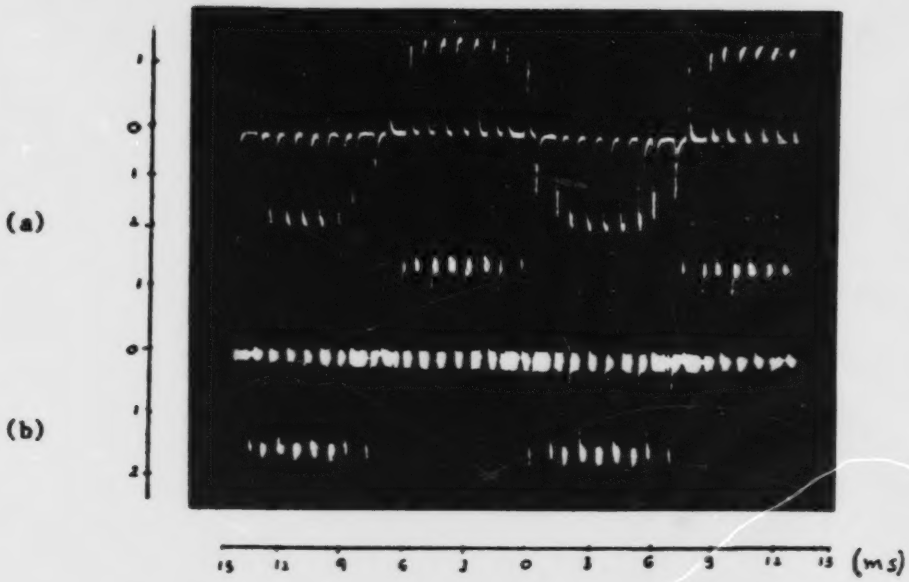

(a) Waveform with an isolation amplifier at the output of the inverter.

(b) Waveform without connecting the isolation amplifier.

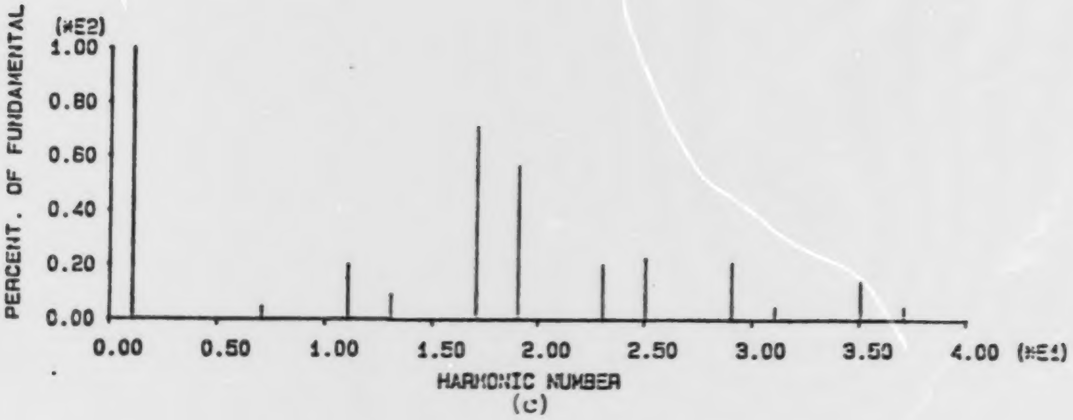

Figure 19 Waveform and harmonic spectrum of reliance inverter output

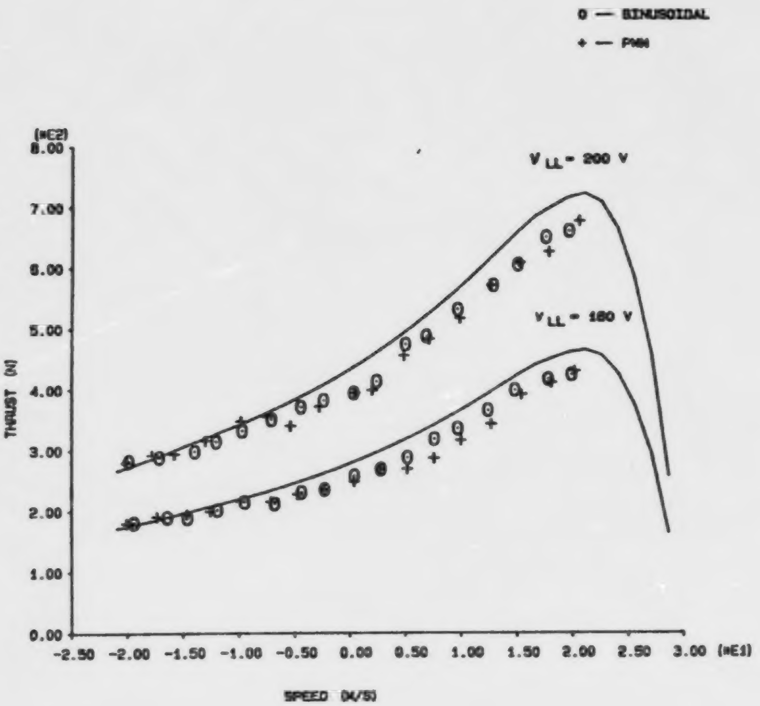

◄ **Figure 20**

LIM thrust for the Al-capped reaction rail (g = 15 mm). Test results (points) for sinusoidal and PWM excitation are compared with computation (curves)

Figure 21 ►

Normal force for the Al-capped reaction rail (g = 15 mm). Test results points) for sinusoidal and PWM excitation are compared with computation (curves)

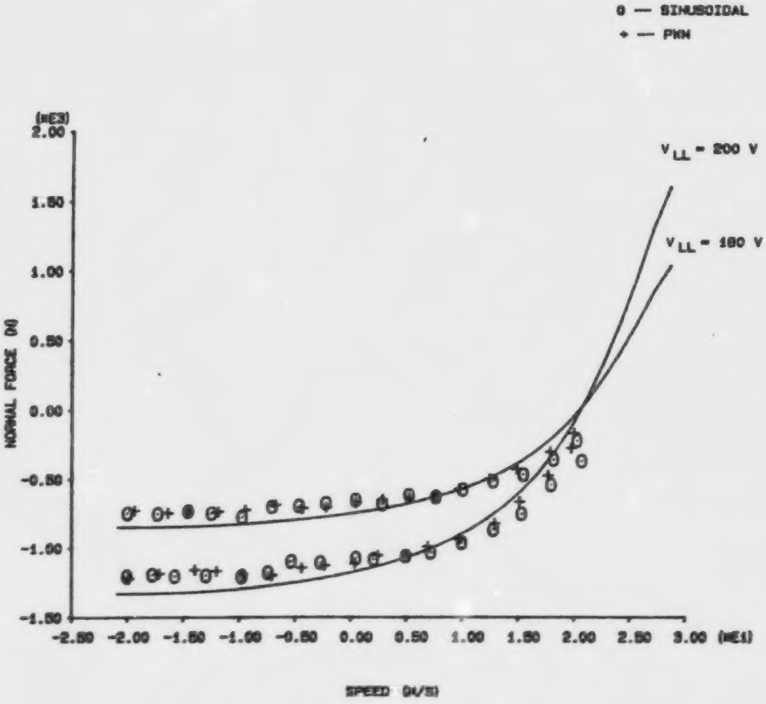

typically less than 0.1 percent of the forces due to the fundamental of the field.

To provide further examples of the effect of time harmonics, some of the spectral distributions obtained using the technique described in Chapter 2 are applied to the analytical model of the LIM.

Case 1. The harmonic spectrum of a natural sampled PWM, with a carrier ratio of 3, as shown in Figure 23(a) is considered. Keeping the fundamental rms value of the phase voltage at 115.5 (200 V, L-L), the harmonic voltages can be calculated. The total thrust due to the odd time harmonics from n = 5 to 37 is again found to be negative (and of magnitude less than 1 N), as shown in Figure 23(b), in agreement with the results obtained earlier

Case 2. A carrier ratio of 9 gave a harmonic spectrum in which the 5th harmonic is negligible and the 7th harmonic is quite high (about 21 percent of fundamental), as illustrated in Figure 24(a). In this case, it is found that the harmonic voltages from n = 5 to 37 produce a net positive thrust, as shown in Figure 24(b). However, the magnitude is again very small as compared to that produced by the fundamental.

4.4.2 Time Harmonic Effects for Solid-Steel Rail

With regard to the solid steel reaction rail, the effect of time harmonics was found to be similar to that for the aluminum-capped rail, as shown in Figures 25 and 26. It is observed that higher time harmonics can slightly augment the thrust, particularly when the magnitude of the 7th harmonic is high. This situation was observed for a PWM waveform, with rms fundamental line voltage equal to 400 V. The spectral distribution shows that the 7th harmonic in phase voltage is equal to 34 percent of the fundamental. Total thrust and normal force due to higher time harmonics from n = 5 to 37 are shown in Figure 27. The maximum value of the thrust is about 5 N, which is again less than 1 percent of the thrust due to the fundamental at that speed.

Thus, from the analytical and experimental results outlined in this chapter, one can infer that the net contribution of time harmonic voltage to the thrust and normal force in an LIM is negligible, in the case of both aluminum-capped and solid-steel reaction rails.

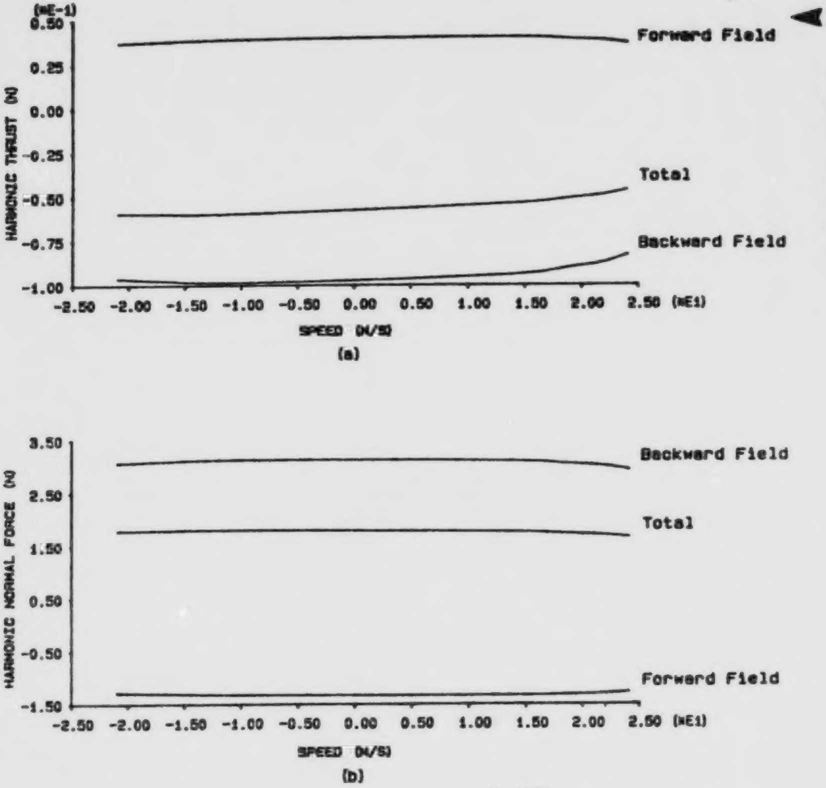

Figure 22

Computed thrust and normal forces for the harmonic voltages in Figure 19 for Al-capped reaction rail (n = 5 to 37)

Figure 23

Typical harmonic spectrum and performance curves for the LIM with Al-capped reaction rail:
(a) R = 3, M = 0.6, voltage = 200 V (L-L)
(b) the total thrust due to the time harmonics

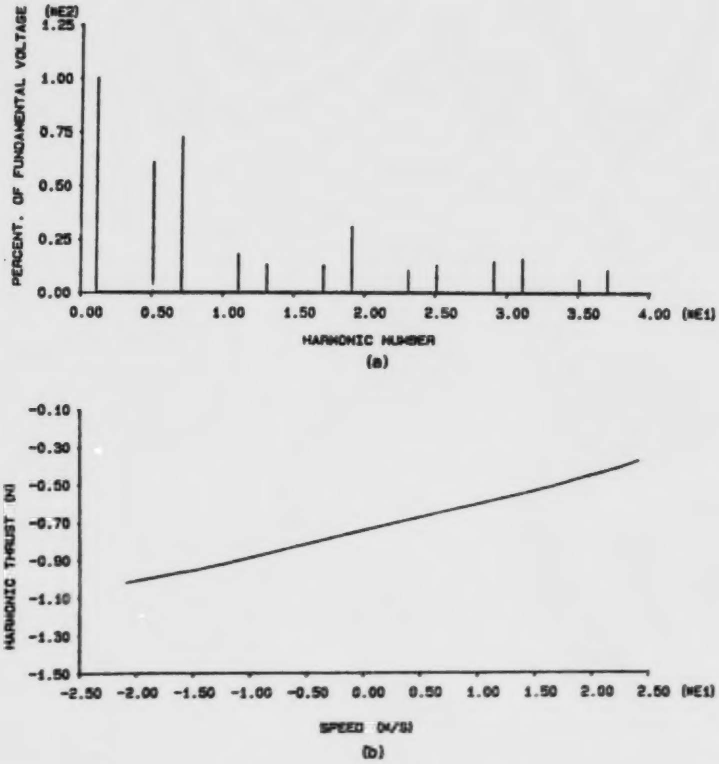

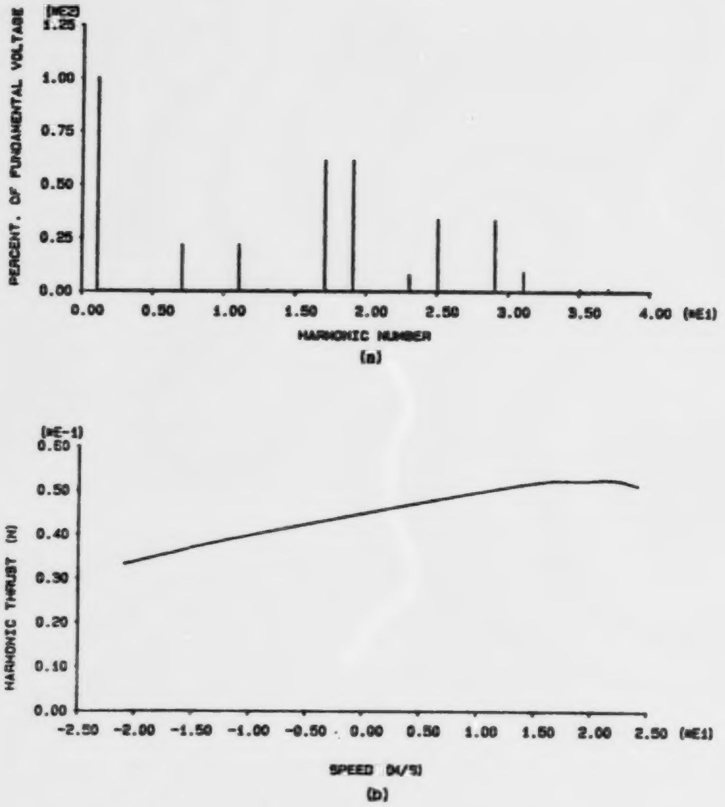

Figure 24

Typical harmonic spectrum and performance curves for the LIM with Al-capped reaction rail:

(a) R = 9,
M = 0.6,
voltage = 200 V (L-L)

(b) the total thrust due to the time harmonics

Figure 25

Thrust for the LIM with solid-steel reaction rail (g=15 mm). Test results (points) for sinusoidal and PWM excitation are compared with computation (curves)

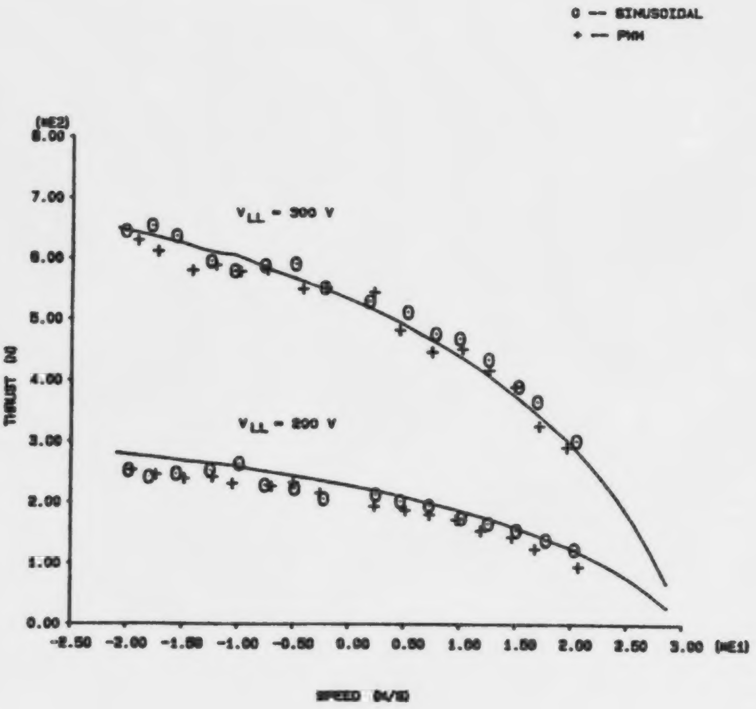

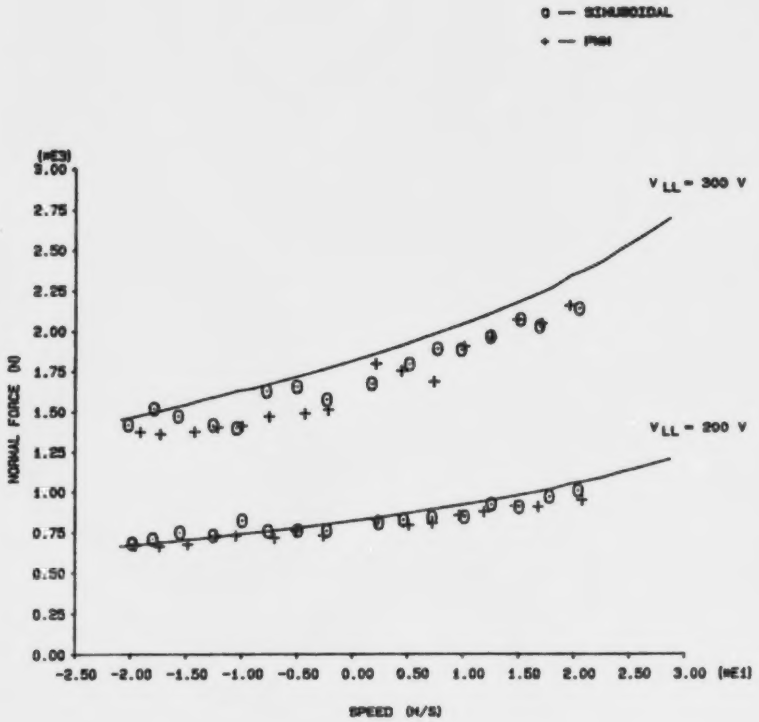

Figure 26

Normal force for the LIM with solid-steel reaction rail (g=15 mm). Test results (points) for sinusoidal and PWM excitation are compared with computation (curves)

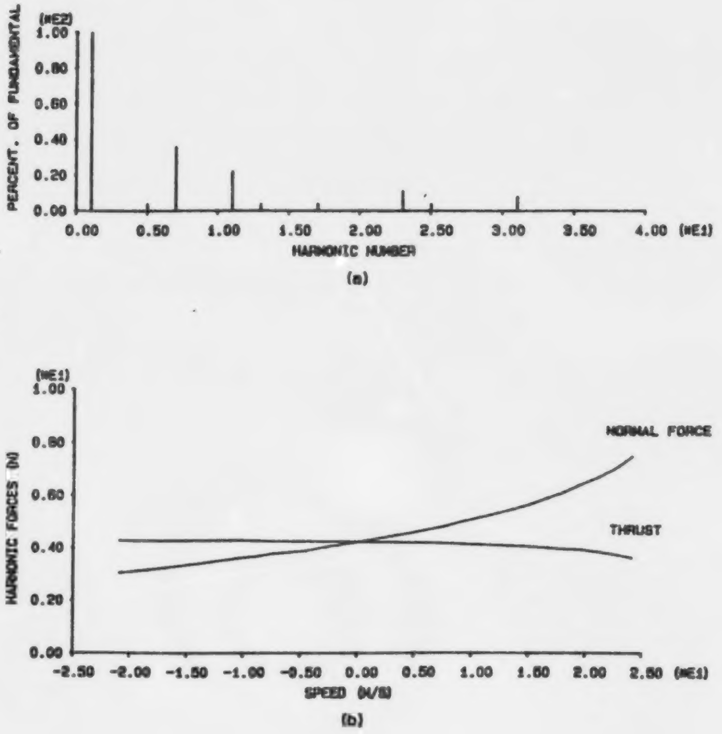

Figure 27

Harmonic spectrum of Reliance inverter and performance curves for the LIM with solid-steel reaction rail:
(a) R = 3, M = 0.856 voltage = 400 V (L-L)
(b) thrust and normal force due to the harmonics

5. FINITE ELEMENT ANALYSIS APPLIED TO LINEAR INDUCTION MACHINES

5.1 Phase Unbalance

Phase unbalance is considered here as an asymmetry in three-phase currents. In a rotary machine, if a balanced set of voltages is applied, the currents will also be closely balanced. In a linear machine, the currents will not, in general, be balanced, due to unequal phase impedances. This unbalance in the phase currents may be attributed to two factors:

- longitudinal end effect.
- unbalance in the primary resistance and leakage reactance.

The finite length of the LIM causes a non-uniform distribution of the peak magnetic flux density in the air gap. This effect, which increases with speed, has been shown to produce a degradation in the performance characteristics of an LIM. Though this longitudinal end effect has been studied in detail, in terms of mechanical performance, little attention has been paid to the phase unbalance produced. Most analytical approaches assume balanced three-phase current sources. The unbalance is caused by the delay in the establishment of the air gap flux at the entry end and the decay of the air gap flux at the exit end, which causes the flux to link differently in the different phases, thus producing an unbalance in the per-phase mutual reactance.

Unbalance in the currents can also be caused by an unbalance in the per-phase primary resistance and leakage reactance, especially in the end winding leakage component. Under standstill conditions, the longitudinal end effect is non-existent, and any unbalance in phase currents is caused by unbalance in the primary leakage reactance i.e., by the asymmetric distribution of phase windings along the length of the machine. This unbalance is typically 1-2 percent, and its effect is small compared to that due to the end effect under dynamic conditions. The unbalance in the currents due to unequal leakage reactances is also noticeable in deep rotor induction machines, where the unbalance is primarily in the slot leakage component. Small unbalance has also been noticed in the primary resistance. This unbalance is caused by small differences in the length of the phase windings, and may affect the low-frequency performance of the LIM under standstill conditions.

The consequence of unbalanced currents is the development of a negative sequence airgap field component, causing a degradation in the performance of the LIM. The effect of this negative-sequence component is to produce a parasitic braking thrust in the normal motoring regime and a motoring thrust in the normal braking regime. Another significant effect of unbalanced currents could be the overloading of one or two phases of the inverter feeding the machine.

Even though several investigators have studied the effect of supply voltage unbalance [31,32] on the performance of induction machines, little attention has been paid to current asymmetry. In reference [33], current asymmetry has been studied using a Fourier series technique, but extensive comparison with experiments was not made. In reference [34], unbalanced terminal voltages caused by unbalanced currents have been studied using the concept of balancing waves, but again no comparison with experimental results has been provided. The current unbalance caused by unbalance in the winding impedance has been treated in reference [35], using equivalent circuit methods, assuming that the unbalance in the primary leakage reactance can be approximated as an unbalance in the primary resistance. Reference [36] has treated current unbalance in a double-sided LIM using an equivalent circuit approach, but again no comparison between analysis and experiments was provided.

Interest was generated in this problem when significant unbalance of up to 10 percent was noticed during earlier experiments at the Queen's LIM test facility. There is also considerable industrial interest in this problem. Engineers at UTDC have noticed up to 20 percent unbalance under certain conditions during experiments on their urban transit linear induction motor.

One of the objectives of the work reported here was to find a suitable method to predict phase unbalance. Analytical electromagnetic field theory is not suitable for evaluating phase unbalance because it basically assumes a three-phase balanced source, and an excitation represented by a current sheet. The finite element method was chosen to study phase unbalance, because it is the only method which can provide an accurate picture of the flux linking the various phases, which can then be used to predict phase unbalance. Further, a modified finite element method was found to be the most suitable technique, because the flux distribution in the air gap can be determined without assuming that the currents are balanced.

5.2 The Finite Element Method

The finite element method is a general technique for constructing approximate solutions to boundary value problems. Since rigorous solution of field problems in electrical engineering are limited to simple geometric shapes and to linear properties of magnetic components, numerical methods such as the finite element method are becoming increasingly popular. The potential of numerical methods has been greatly enhanced by the introduction of fast, high memory capacity computing facilities.

The main advantage of the finite element method over other numerical techniques, such as the finite difference methods, is that complex boundary shapes can be accommodated quite easily. Finite difference methods are more easily applied to problems in which geometries are predominantly rectangular. Using the finite element method, complex contours can be approximated easily by linear segments of appropriate size. In addition, the computer implementation of the finite element method is simpler than for the finite difference method. The difference between the two numerical techniques has been discussed at length in the references [37], [38] and [39]. Finite element methods were first developed for civil and mechanical engineering applications but, as a result of research conducted over the past 10-15 years are equally being applied in electrical engineering, because of the generality and richness of the ideas underlying the method.

A review of the finite element method for evaluating the field distribution in electric machines is provided in Appendix B.

5.3 Discretization

The linear machine (the detailed specifications of which are given in Chapter 4, Table 1) was discretized as shown in Figure 28. A very fine discretization over the entire machine was not possible (or necessary)

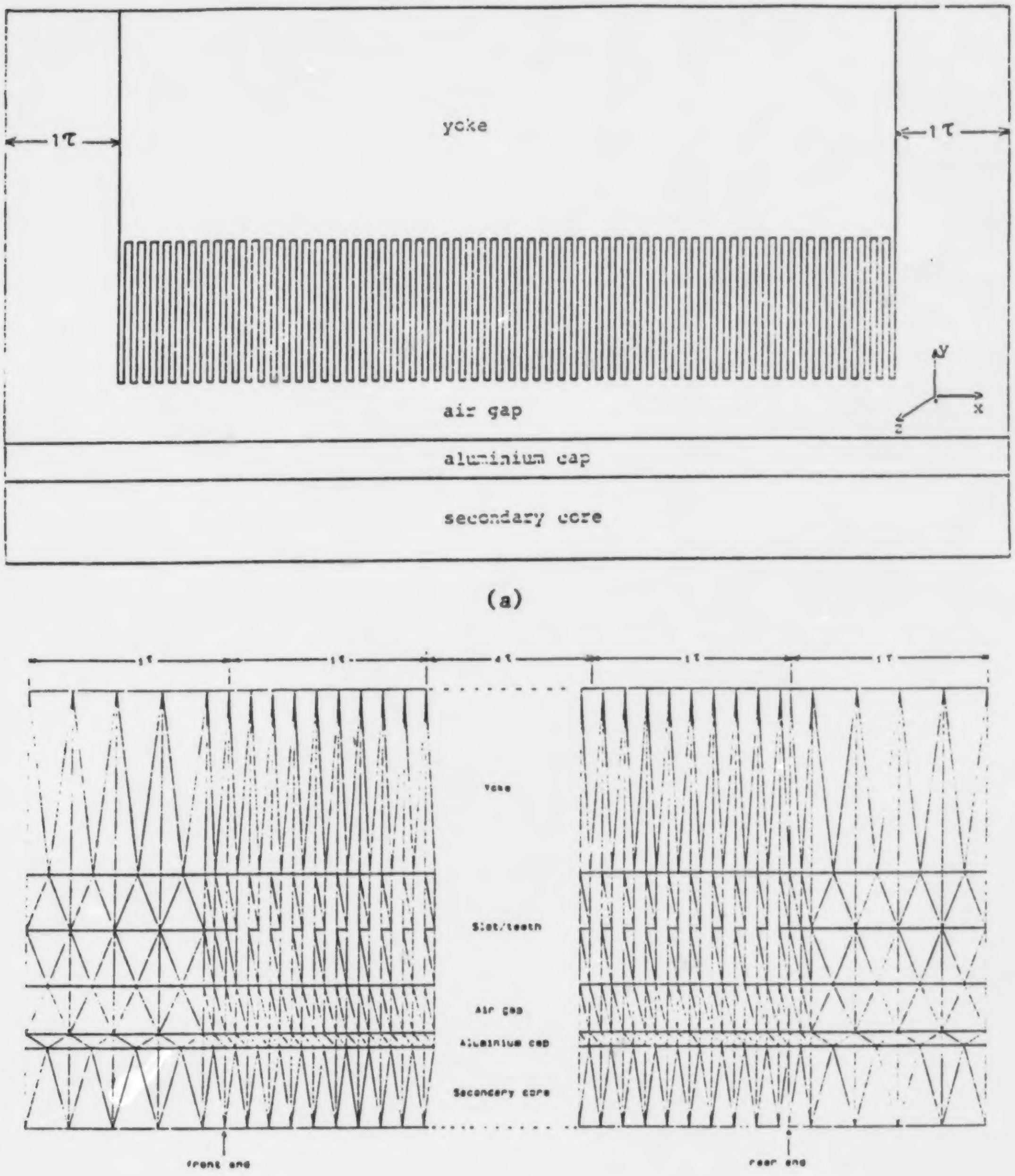
1τ
yoke
1τ
y
x
z
air gap
aluminium cap
secondary core
1τ
1τ
4τ
1τ
1τ
Yoke
Slot/teeth
Air gap
Aluminium cap
Secondary core
front end
rear end

(a)

(b)

Figure 28 (a) The geometry of the test LIM, with x-axis compressed relative to y-axis
(b) The finite element discretization used for analysis of field distribution

in view of the limited number of nodes which could be handled by the finite element solution (2000 to 3000). For a conventional-rotary induction machine, it is possible to analyse the field distribution on a per pole basis. For a linear induction machine, the entire machine must be discretized to allow representation of the end effect. In addition, appropriate lengths beyond the front and rear of the machine must be modelled to allow for representation of the establishment and decay of induced currents.

Figure 29 shows the discretization of a typical tooth/slot unit. First-order elements have been used in the formulation. Node numbering is an important criterion for bandwidth reduction. The nodes should be numbered such that the maximum difference between the node numbers of any element should be as small as possible. In this case the ordering sequence is obvious. The length of the machine is very large compared to the height and hence the nodes are numbered from bottom to top, as shown in Figure 29. The element numbering shown was chosen for ease of programming and does not affect the bandwidth.

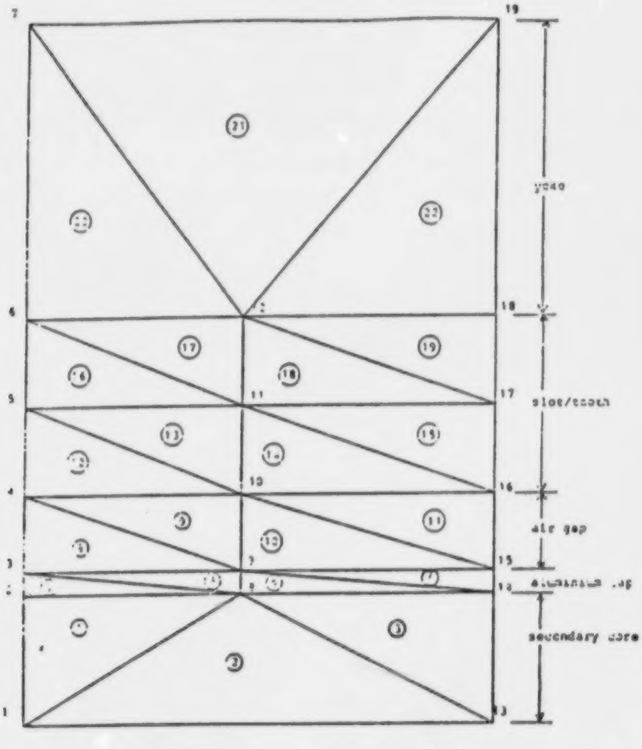

Figure 29 Discretization of a typical tooth-slot unit

5.4 Representation of Excitation

The currents are assigned to nodes to provide a good approximation to the excitation distribution in the actual machine. A typical discretization of the slot and the values assigned to the individual nodes are shown in Figure 30. It is convenient to choose the instant at which the current in phase A is at its peak value. Currents in phases B and C are then equal to -0.5 times their maximum values. The currents at the individual nodes of the slot element are assigned to make the total current in the slot equal to that in the actual machine, and hence the mmf in the airgap will be the same. A finer discretization of the slot would have permitted a more uniform distribution of the current, but is not necessary in order to accurately model the overall field distribution in an LIM.

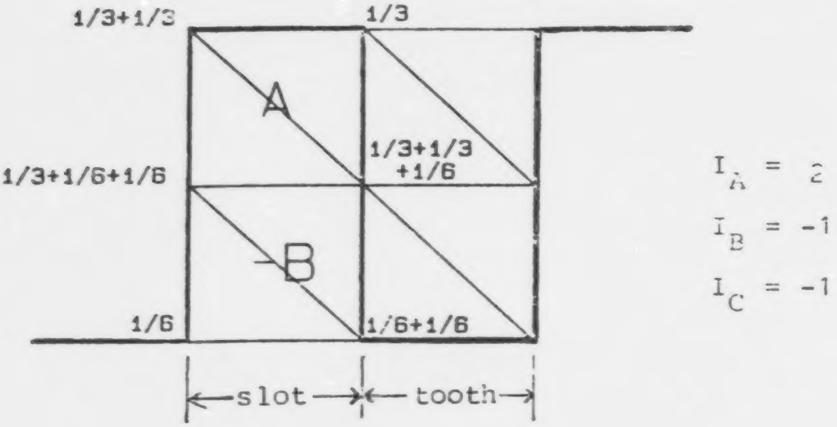

Figure 30 Distribution of normalized current at the nodes of a slot

5.5 Calculation of Performance

After the magnetic vector potentials are solved using the procedure described above, the performance characteristics such as the thrust and normal force can be calculated. The flux density in each element is calculated using Equation (B.6).

The thrust and normal forces are evaluated using the Lorentz equation. For the time-stepping technique, the Lorentz equation can be expressed as:

$$\text{Force} = \iiint J \times B \, dV \qquad (5.1)$$

where J, the local induced current density in the secondary, is given by:

$$J = \sigma(\partial A/\partial t + u \times B) \qquad (5.2)$$

For the analysis of LIMs, a reference frame is selected such that the secondary is assumed to be moving with a velocity of u in the x-direction (the LIM itself being stationary). Hence, $u = u_x$. Therefore, evaluating the cross product in Equation (5.2), we obtain:

$$J = \sigma(\partial A/\partial t + u_x B_y) \qquad (5.3)$$

Now Equation (5.1) can be split into its components, giving the thrust and normal force as:

$$\text{Thrust} = \iiint J B_y dV \qquad (5.4)$$

$$\text{Normal force} = -\iiint J B_x dV \qquad (5.5)$$

The above equation for normal force is incomplete because it includes only the reaction force and does not include the attractive force between the primary and secondary. The correct expression for the normal force, including the attractive component, is as follows:

$$\text{Normal force} = -\iiint J B_x \, dV + 1/(2\mu_0) \iint B_s^2 \, dxdz \qquad (5.6)$$

where B_s is the normal component of the flux density at the surface of the secondary.

The field is assumed to be uniform in the z-direction, hence the expressions for thrust and normal force reduce to:

$$\text{Thrust} = w' \iiint J B_y \, dS \qquad (5.7)$$

$$\text{Normal force} = -w' \iint J B_x + w'/2\mu_0 \int B_s^2 \, dx \qquad (5.8)$$

where w' is the primary stack width. This is corrected for fringing because the width of the secondary is usually greater than the primary width. As noted in Appendix A, w' is given by:

$$w' = w + 2(g + d) \qquad w > L + 2(g+d)$$

$$w' = w \qquad w \leq L + 2(g+d)$$

For the complex steady-state method, the expressions for the thrust and normal force are modified using complex conjugates, as:

$$\text{Thrust} = w'/2 \iint J B_y^* \, ds \tag{5.9}$$

$$\text{Normal force} = -w'/2 \iint J B_x^* \, dS + w'/4\mu_0 \; B_s^2 \, dx \tag{5.10}$$

5.6 Finite Element Analysis of Test LIM

The finite element method has been used to examine the performance of the CIGGT test LIM, with design parameters given in Table 1.

5.6.1 DC Magnetostatic Test

As a first step, a special test was performed under magnetostatic conditions in an attempt to validate the ability of the finite element method to predict air gap fields under steady-state (time invariant) conditions. The test was performed, after removing the aluminum cap, with an air gap of 15 mm.

To establish a magnetostatic condition corresponding to one instant of a three-phase ac excitation (conventionally when t=0), namely, when the current is a maximum in phase A and minus half the maximum in phases B and C, a dc current of 200 Amperes was passed throught phase A and -100 Amperes each through phases B and C. This was achieved by feeding the dc current into the linear machine connected as shown in Figure 31. A 50 V, 250 A stabilized dc power supply was used as the source. The normal component of the flux density was measured at 1 cm intervals along the entire length of the machine, using a Hall effect sensor.

Finite element analysis was conducted for the same conditions, by solving Equation (B.1), in which the induced current density component of the left-hand side will be absent. Figure 32(a) shows the mmf distribution for the current distribution selected. A comparison of the analytical and experimental airgap field distributions is shown in Figure 32(b). The finite element distribution, though somewhat lower

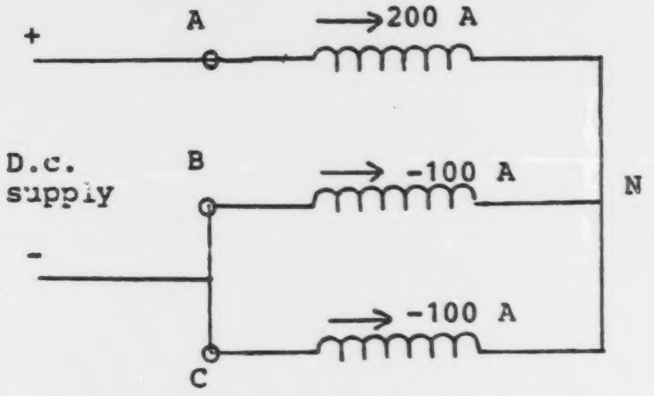

Figure 31 Terminal connections for the magnetostatic test

in magnitude compared to the experimental results, has the same shape. Both distributions show slot/tooth ripple. This ripple is considerably greater in the finite element distribution because of the coarse discretization. The peaks of lower flux density at the ends are because of half-filled end slots.

It can be seen that the flux distribution exactly follows the pattern of the mmf distribution. Note that the airgap field is quite sensitive to the magnitude of the gap. The nominal gap for the results in Figure 32(b) was 15 mm, and the discrepancy between test and analytical results could be caused by a deviation in the test gap of 1.5 mm. The above comparison is considered adequate to validate the finite element method under magnetostatic conditions.

5.6.2 Complex Steady-State Solution

The complex steady-state method [40,41] is a simple procedure for solving the time varying problem. The field variables, which are assumed to vary sinusoidally, are conveniently represented by complex space phasors of the form $e^{j\omega t}$. Hence the partial differential operator $\partial/\partial t$ may be replaced by the arithmetic factor $j\omega$. This procedure is similar to that used in one-dimensional phasor circuit analysis. The simple chord iteration method is used to find the appropriate permeability of each element, as described in Appendix B.

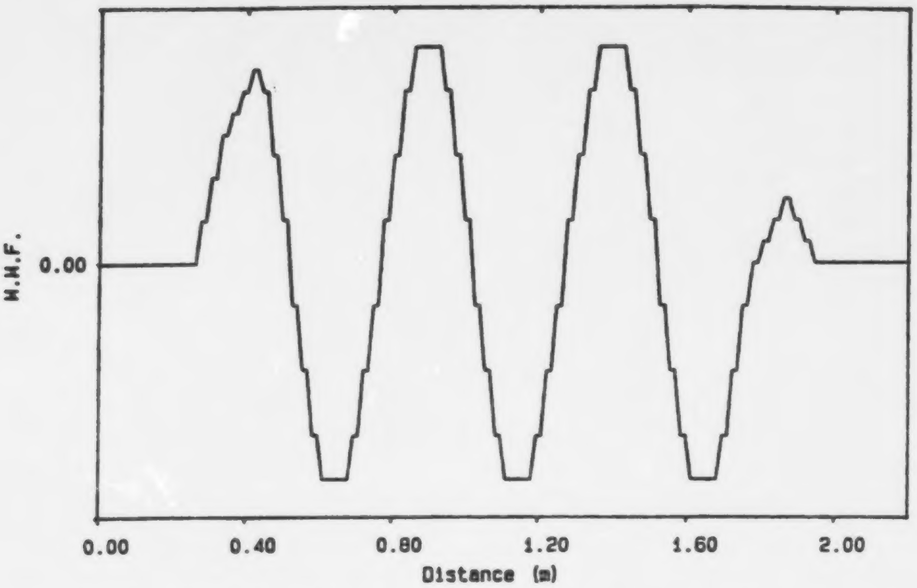

Figure 32(a) MMF distribution with 200, -100 and -100 Amperes in phases A, B and C, respectively

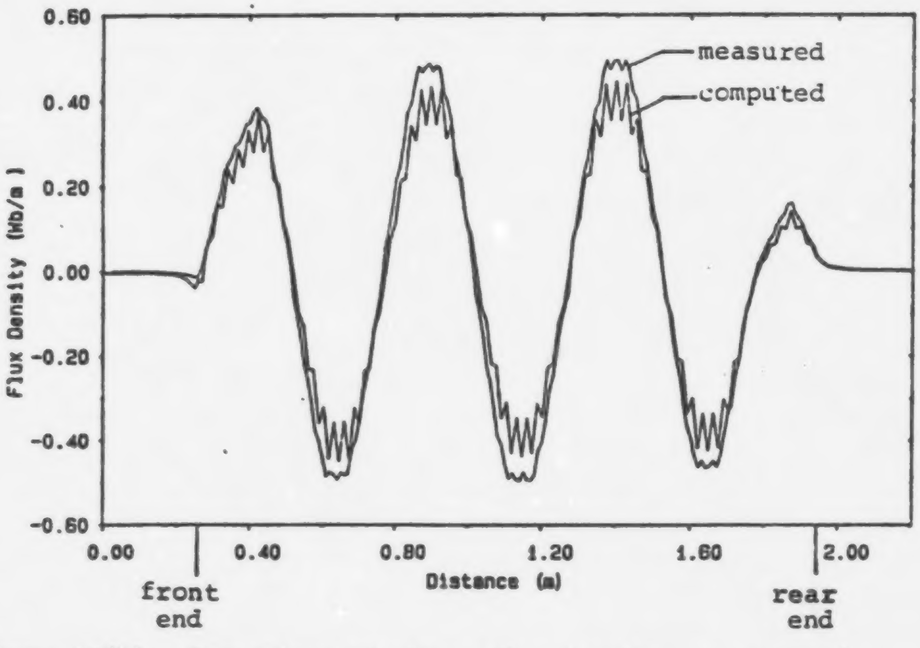

Figure 32(b) Comparison of airgap flux density, as measured and as computed using the finite element model

The complex steady-state analysis was applied to the linear machine under various operating conditions. For the analysis in this chapter, the nominal condition is defined as:

- phase current = 200 A rms
- airgap = 15 mm
- aluminium conductivity = 1.859×10^7 Siemens (this is the conductivity obtained after multiplying the actual conductivity by a Russell and Norsworthy factor of 0.57, calculated using Equation (B.3)
- secondary back-iron conductivity = 0.0
- secondary back-iron permeability = 1600
- stator iron permeability = 2500
- discretization as in Figure 28(b).

The results shown in this section were obtained under these nominal conditions, unless otherwise specified.

In the complex steady-state method, the solution is obtained by iteratively solving the nonlinear equations once. The solution has two components, real and imaginary. Figure 33 shows the distribution of the real and imaginary components of the field for an input frequency of 11 Hz. The real and imaginary components have a spatial phase displacement of 90 degrees.

Figure 34 shows the distribution of the real component of the field under the same conditions as above, but at slip frequencies of 22, 0 and -7 Hz. These represent each of the three distinct regions of LIM operation, namely plugging, motoring and regeneration. A schematic of the expected pattern of flux lines is shown in Figure 35. It is apparent that Figures 32 and 33 follow this expectation. The travelling wave nature of the field can also be seen from the above flux distributions. The coarse discretization in regions such as the stator core results in the ragged appearance of the flux lines. This is considered unimportant as the precise field distribution is not generally required in these regions. A good definition of the air gap field is necessary for the evaluation of mechanical performance.

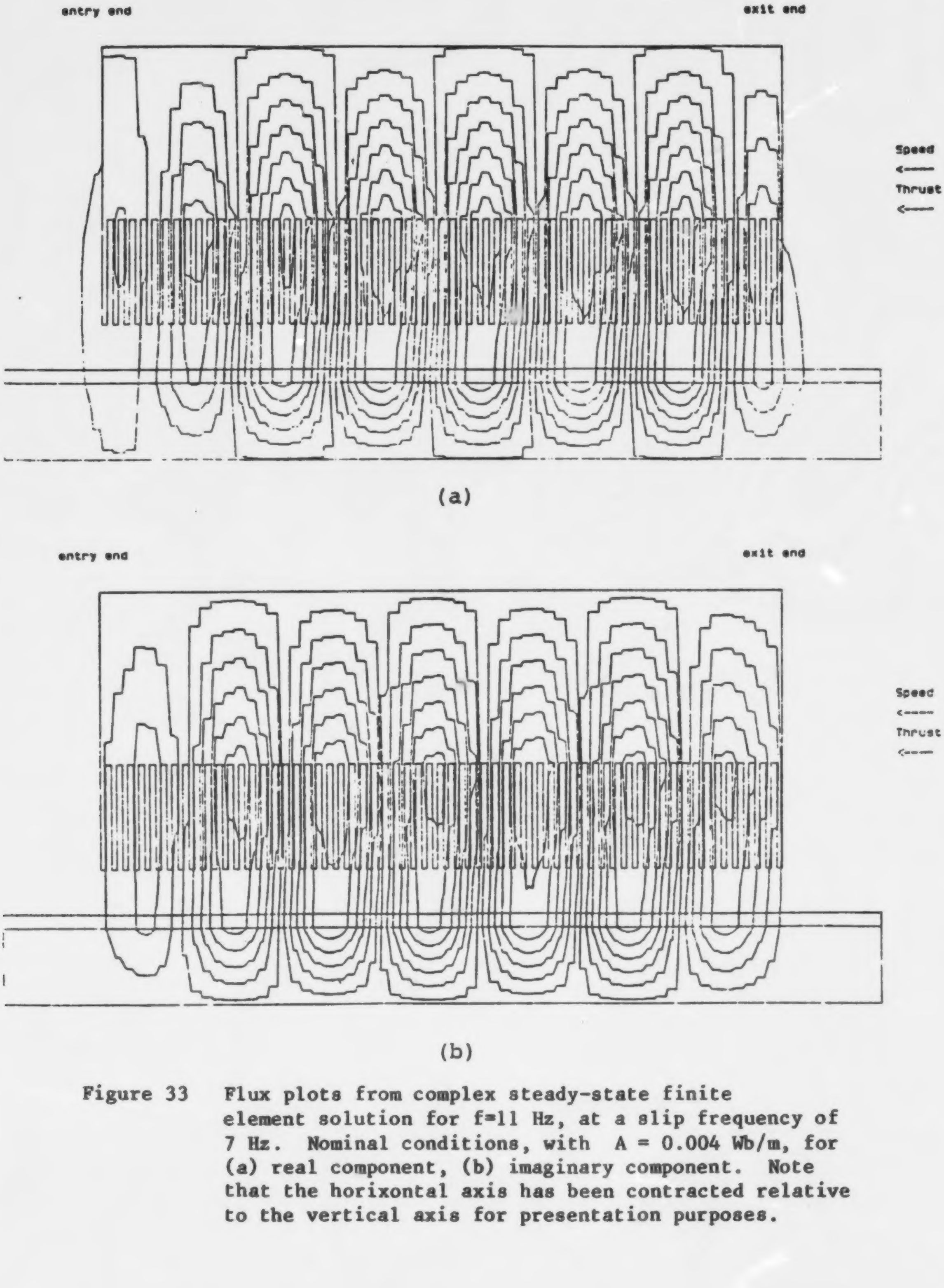

Figure 33 Flux plots from complex steady-state finite element solution for f=11 Hz, at a slip frequency of 7 Hz. Nominal conditions, with A = 0.004 Wb/m, for (a) real component, (b) imaginary component. Note that the horixontal axis has been contracted relative to the vertical axis for presentation purposes.

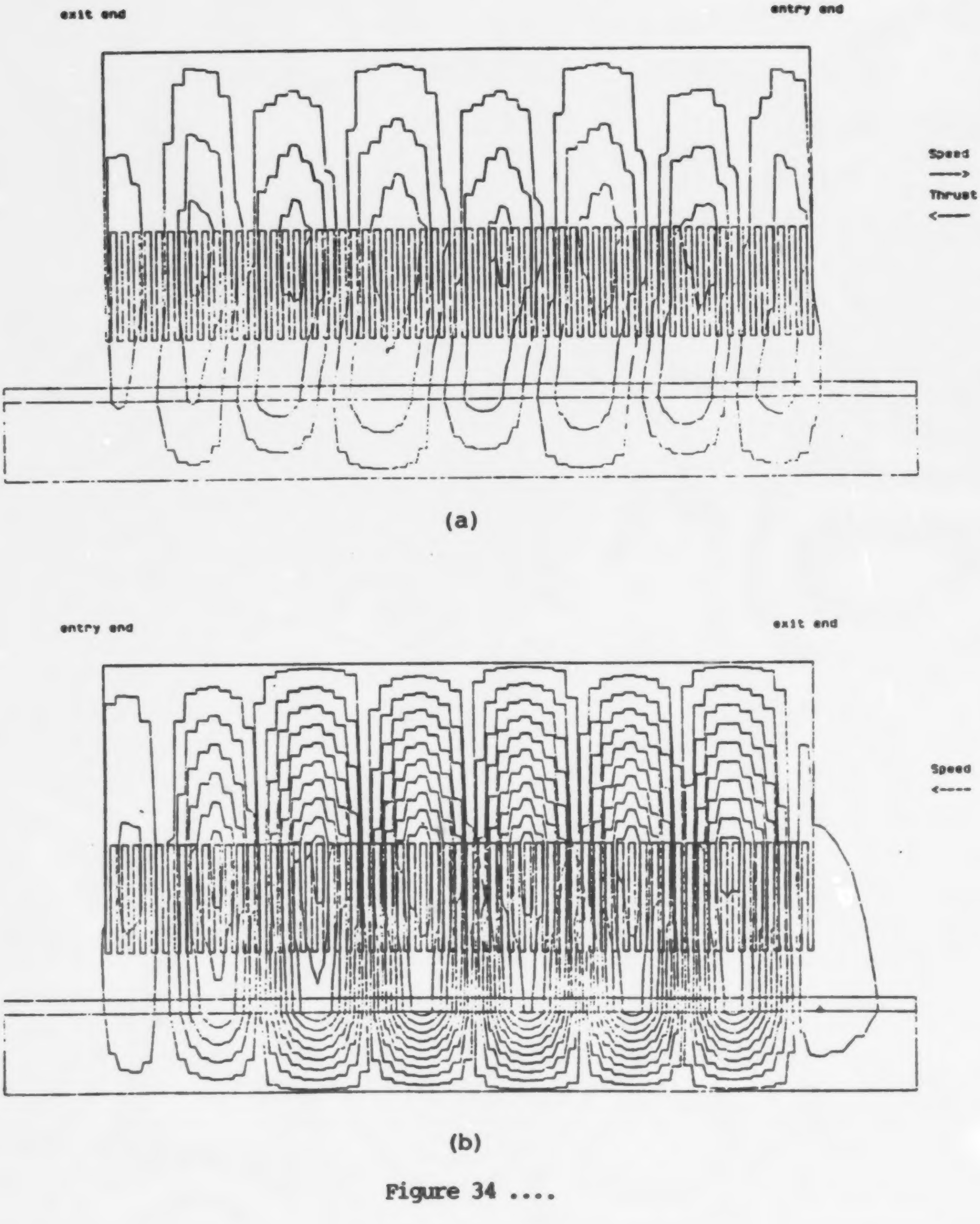
exit end
entry end
Speed
——>
Thrust
<——
entry end
exit end
Speed
<----

(a)

(b)

Figure 34 ....

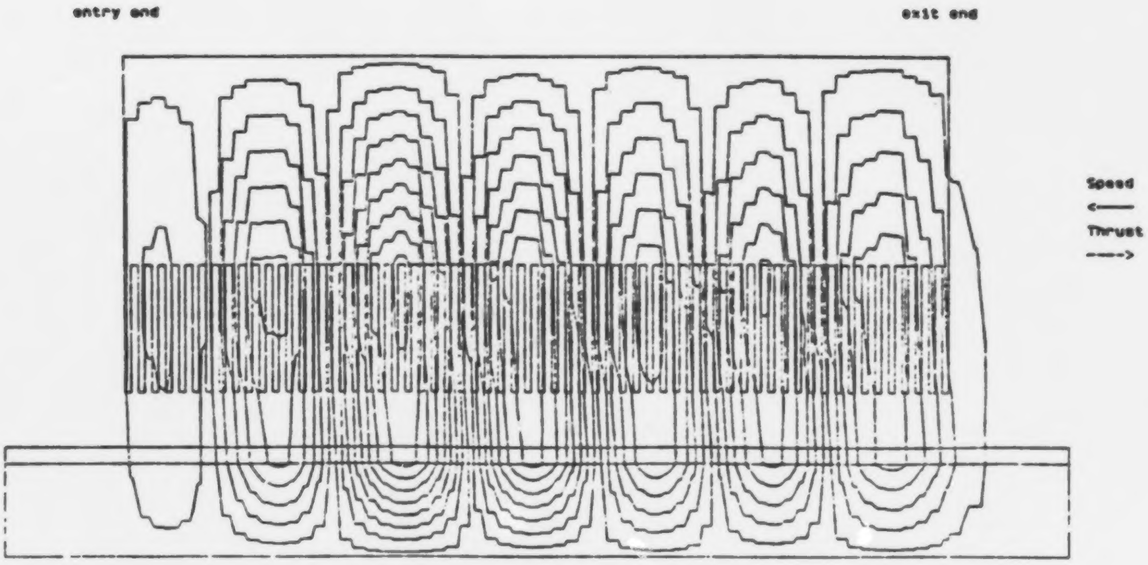

(c)

Figure 34 Flux plot for the real component of the complex steady-state finite element solution. Nominal conditions, with A=0.004 Wb/m, for slip frequencies of (a) 22 Hz (plugging), (b) 0 Hz (synchronous), and (c) -7Hz (regeneration)

Figures 36 and 37 show the real and imaginary components of the induced eddy current distribution in the aluminium cap due to transformer and velocity effects. The induced current density due to transformer effect is sinusoidal since it depends on the time variation of the vector potential, whereas the eddy current density due to the velocity effect is not sinusoidal since it depends on the space variation of the vector potential. The discretization used, being coarse, emphasizes the slot ripple on the space distribution of the vector potential.

Figures 38 through 41 illustrate the computed flux density in the air gap, the thrust density and the normal force density distributions for 11 Hz operating frequency, with slip frequencies of 22, 7, 0, and -7 Hz. Conforming to expectations, the flux density drops to a minimum at the slot opening, and rises to a maximum at the tooth, causing the slot ripple seen in the flux density distributions. The flux density and force density distributions emphasize the slot ripple because of the nature of the discretization. Under constant current conditions, the decrease in flux density as the machine goes into plugging and regeneration is evident from the plots. It can be noticed that the end effect increases as the speed approaches synchronous velocity. It is

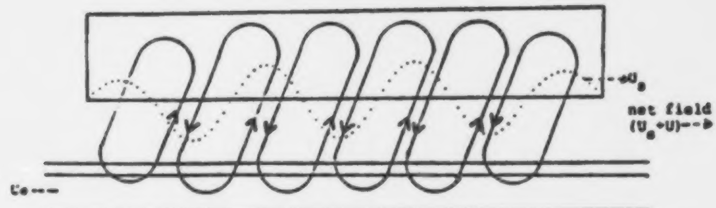
--→U_s
net field
(U_s+U)--→
U←--
Thrust--→

Plugging

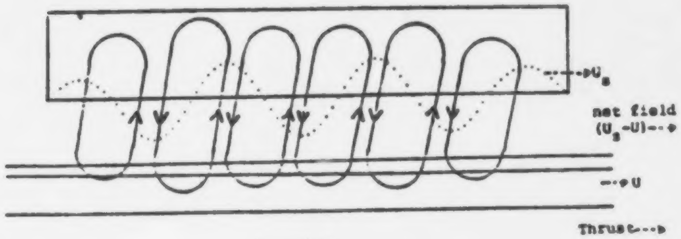
---→U_s
net field
(U_s-U)--→
--→U
Thrust--→

Motoring

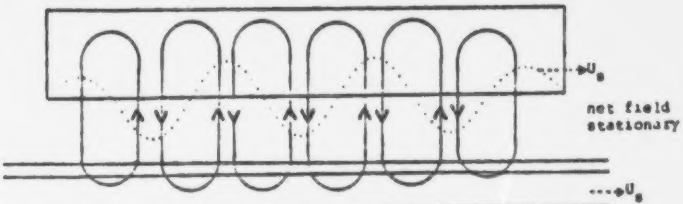
---→U_s
net field
stationary
---→U_s

Synchronous velocity

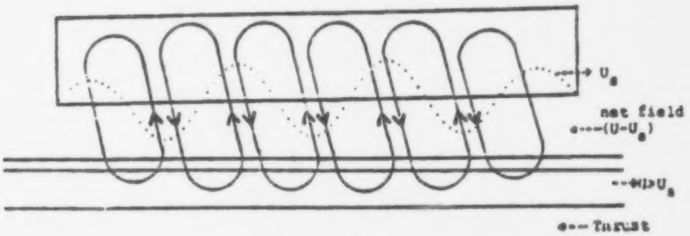
--→ U_s
net field
←---$(U-U_s)$
--→$U>U_s$
←-- Thrust

Regeneration

Figure 35 Schematic of expected pattern of flux lines

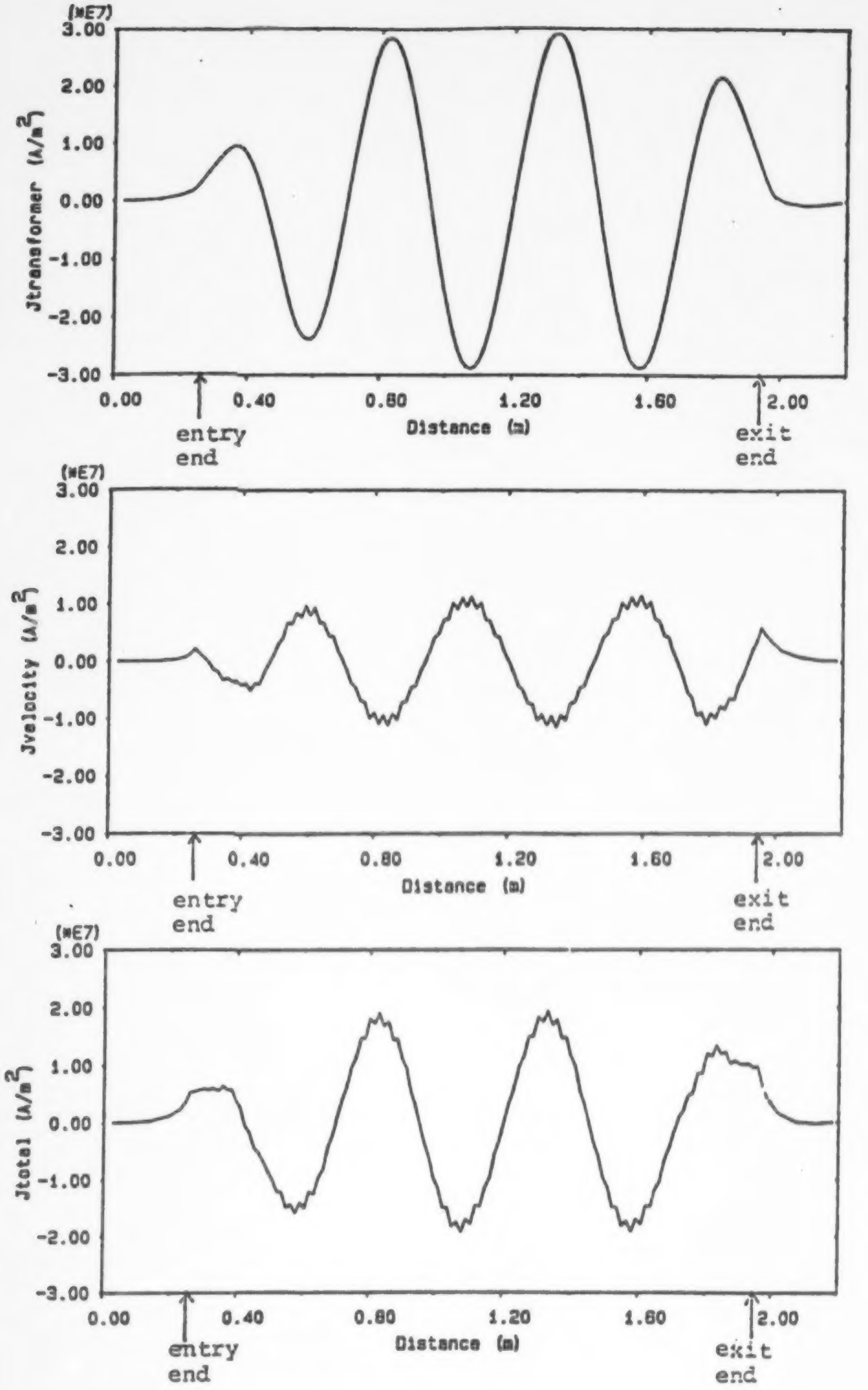

Figure 36 Induced current density curves (real component) for f=11 Hz, at a slip frequency of 7 Hz

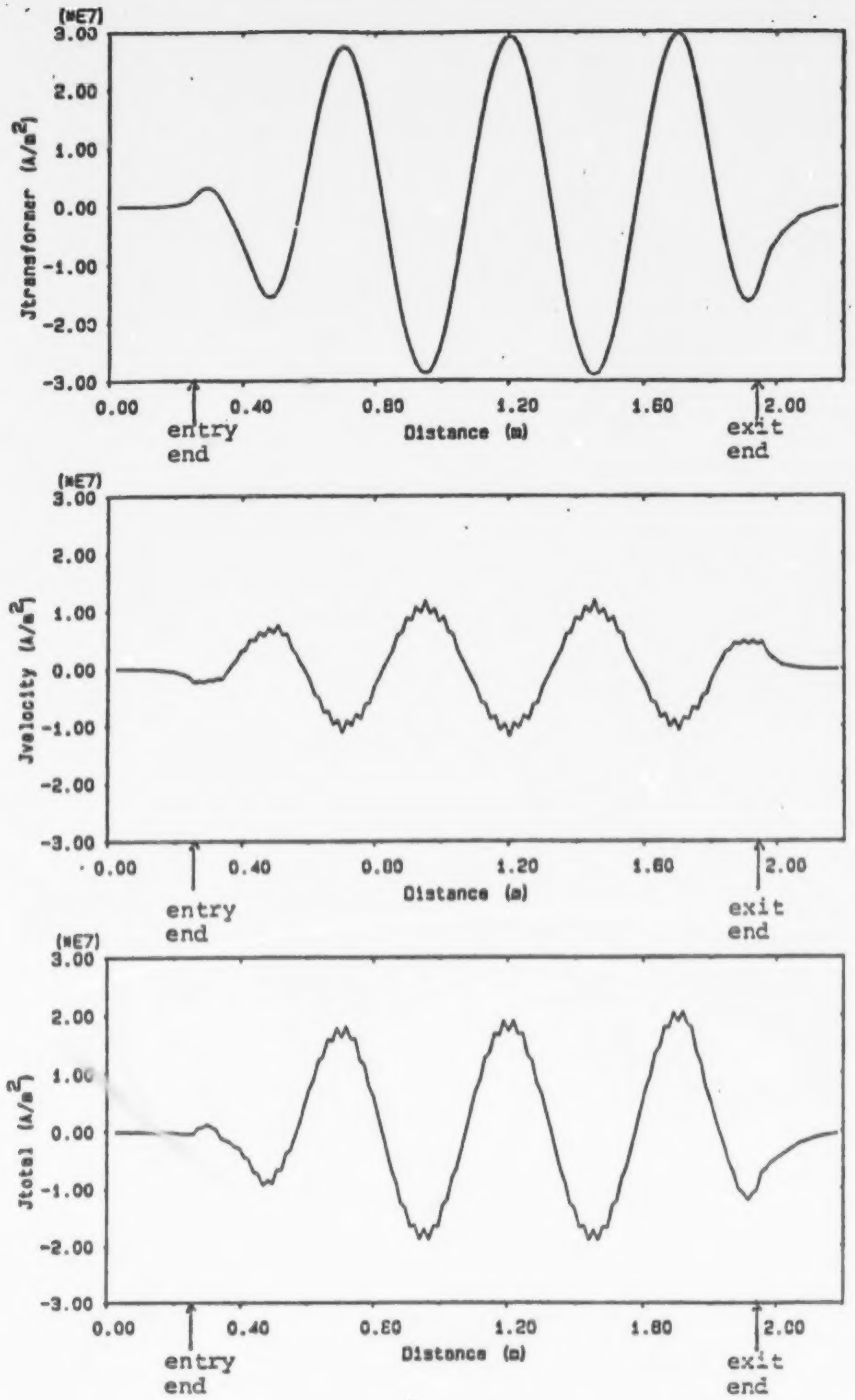

Figure 37 Induced current density curves (imaginary component) for f=11 Hz, at a slip frequency of 7 Hz

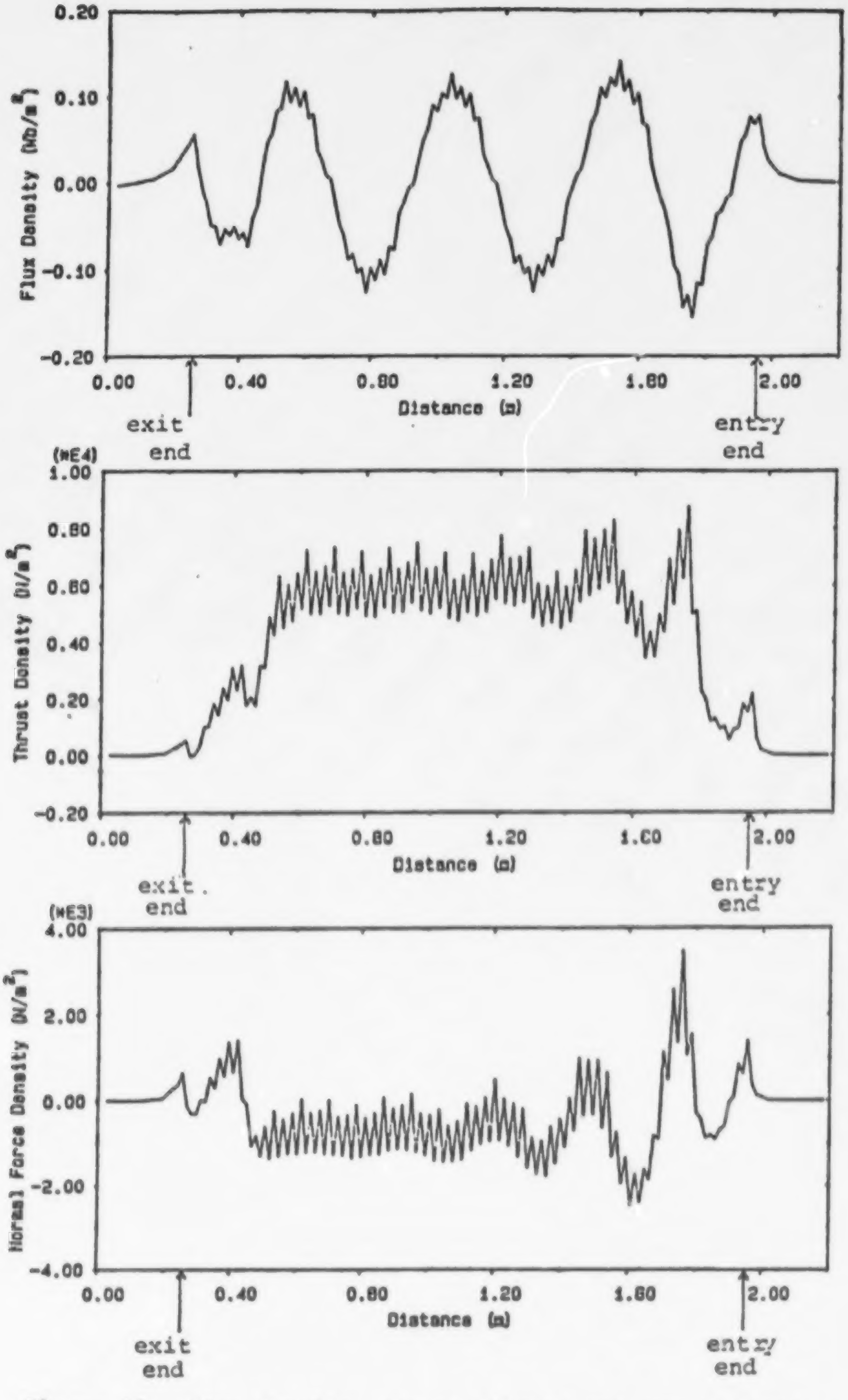

Figure 38 Flux density, thrust density and normal force density for f=11 Hz, at a slip frequency of 22 Hz

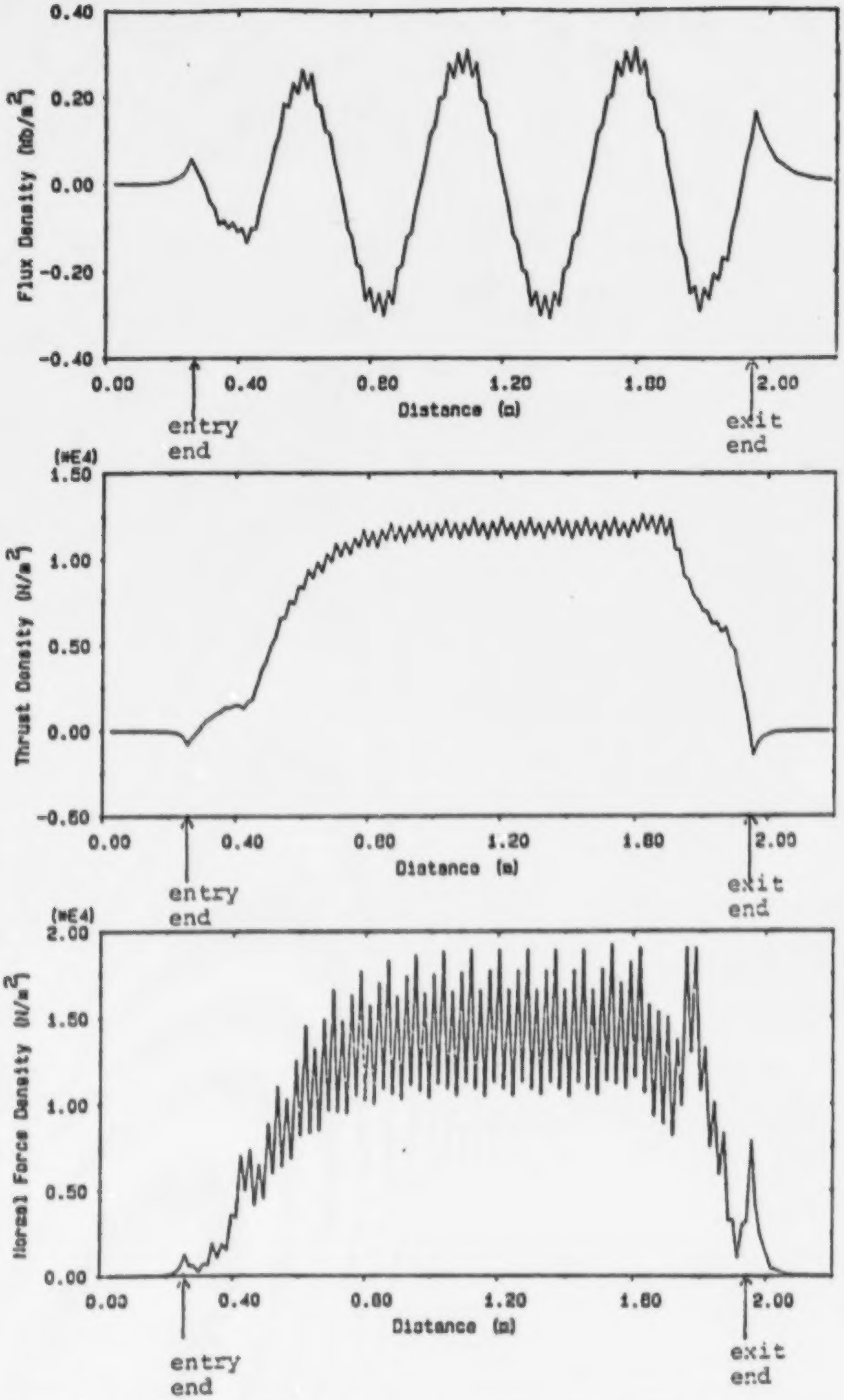

Figure 39 Flux density, thrust density and normal force density for f=11 Hz, at a slip frequency of 7 Hz

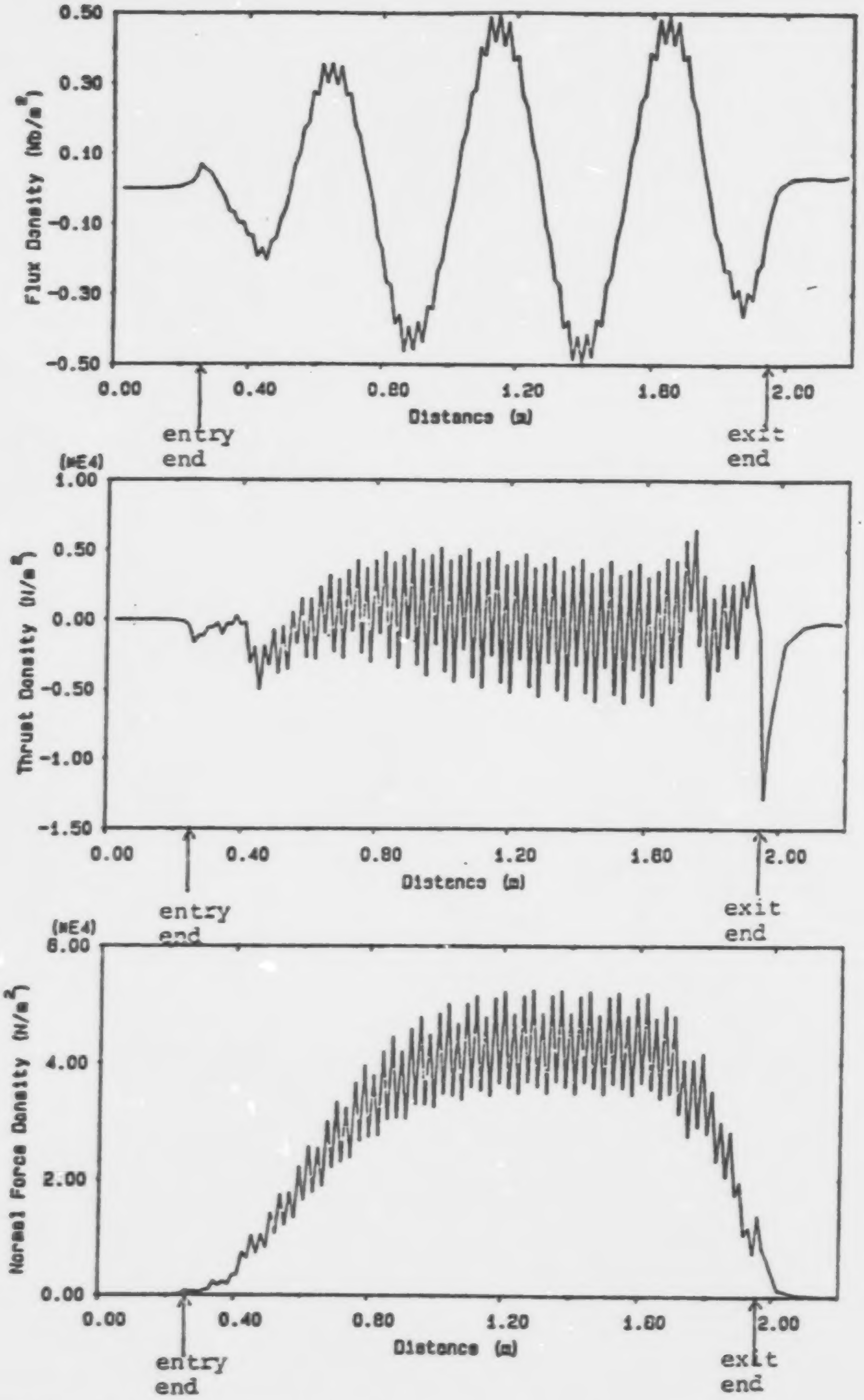

Figure 40 Flux density, thrust density and normal force density for f=11 Hz, at a slip frequency of 0 Hz

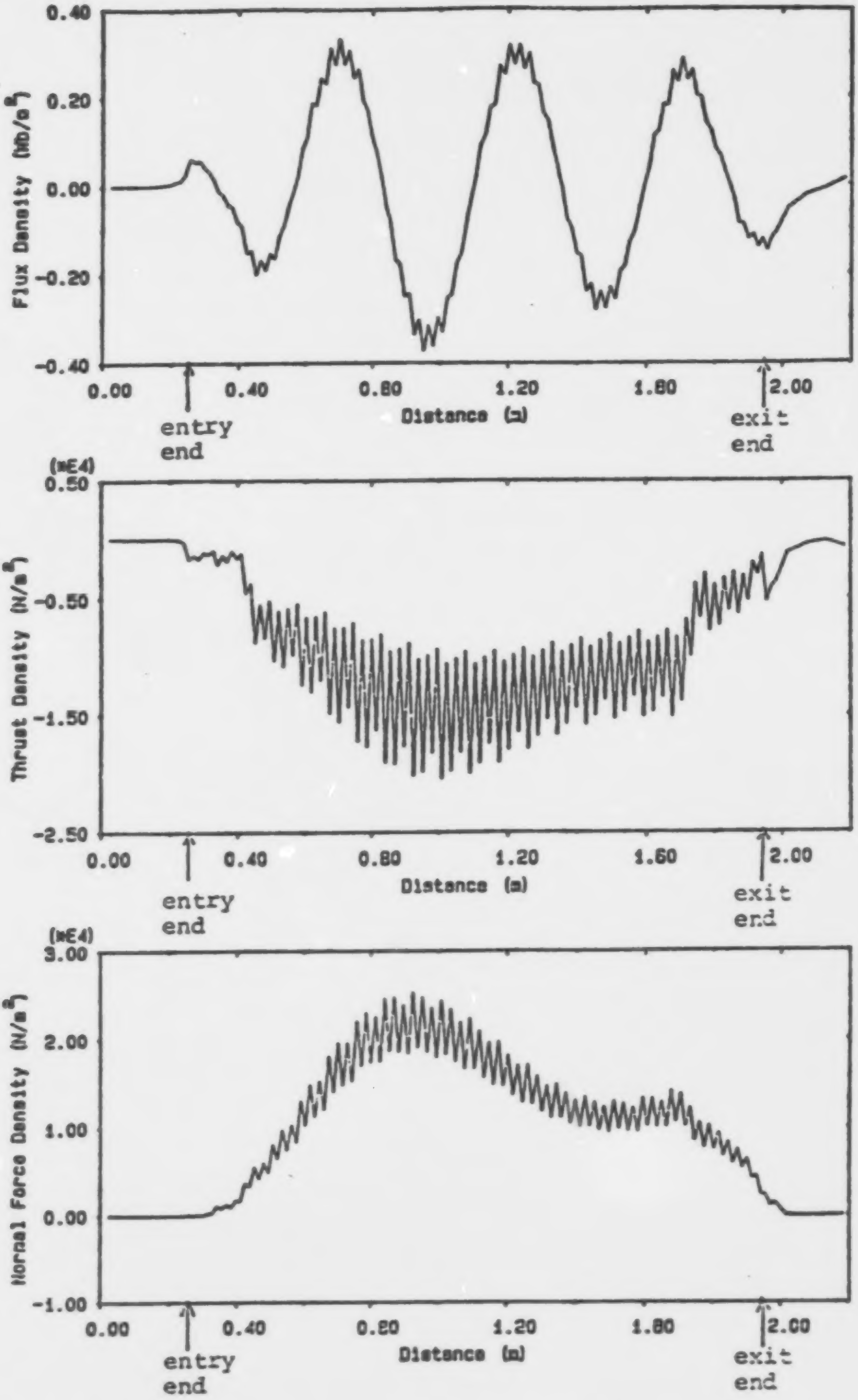

Figure 41 Flux density, thrust density and normal force density for f=11 Hz, at a slip frequency of -7 Hz

also evident that the intensity of the field outside the machine is very small. The attenuation of the thrust density curve at the entry clearly seen from the figures. The gradual build-up of the thrust and normal forces at the entry end is due to end effect. At synchronous velocity, the thrust density is very small and the magnitude of the ripple is relatively large, because the total induced current becomes very small. The repulsive component of the normal force is also very small, and hence the normal force is almost entirely attractive.

The flux plot and the density curves at a higher excitation frequency, namely 40 Hz, but at the same slip frequency (7 Hz) are shown in Figures 42 and 43. The increase in end effect as the frequency is increased is evident in both the flux plot and the density curves. The magnitude of the peak flux density at f=40 Hz is lower than at f=11 Hz, at the same slip frequency. Although the maximum thrust density is almost the same at f=11 Hz and at f=40 Hz, the total thrust is lower at 40 Hz, because of the increase in end effect. The normal force density shows a considerable decrease at the higher frequency, as expected.

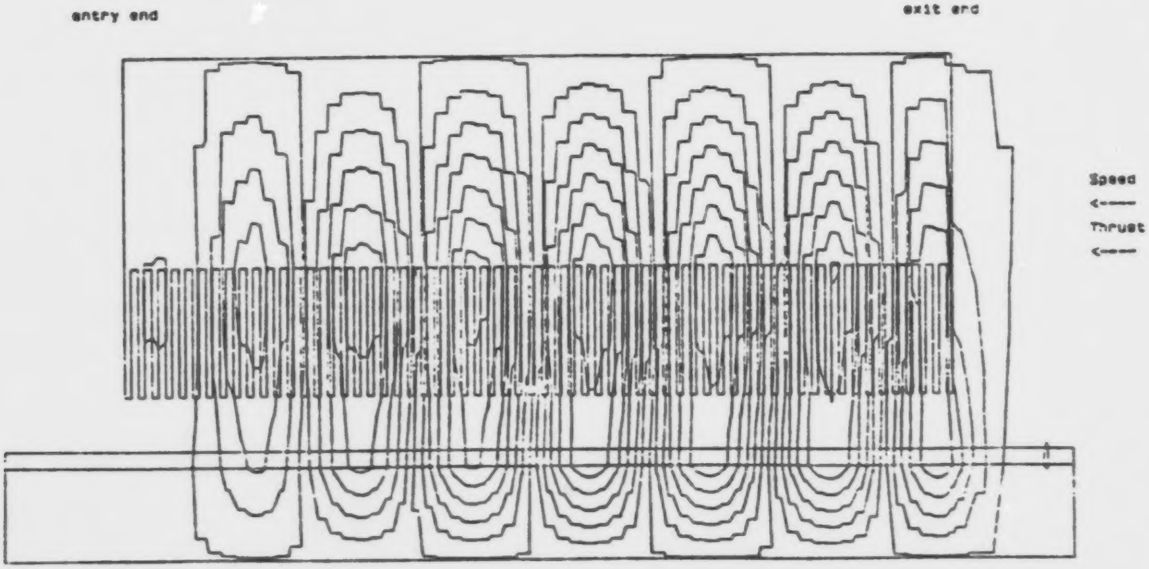

Figure 42 Flux plot for the real component of the complex steady-state finite element solution for f=40 Hz, at a slip frequency of 7 Hz. Nominal conditions, with A = 0.004 Wb/m

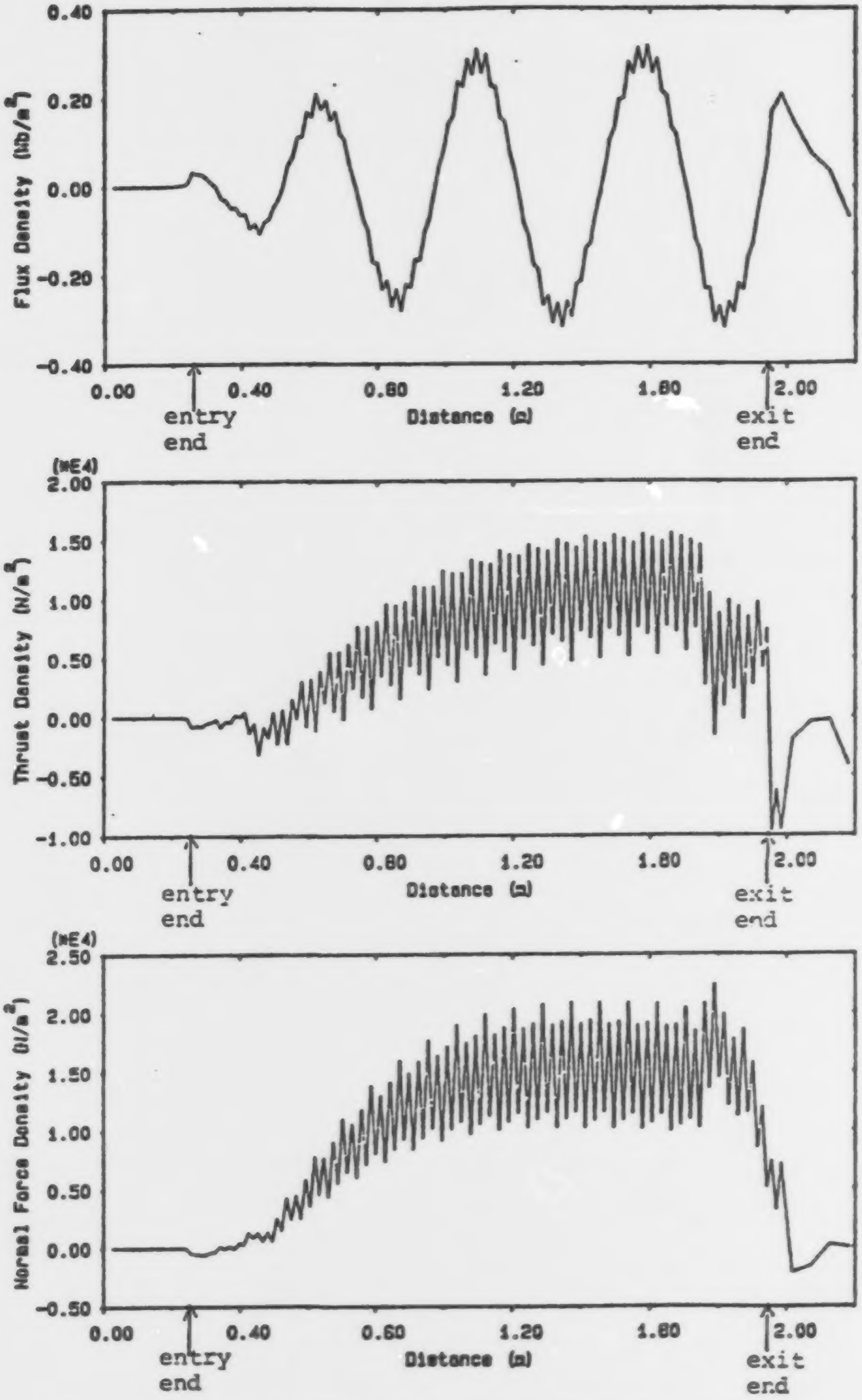

Figure 43 Flux density, thrust density and normal force density for f=40 Hz, at a slip frequency of 7 Hz

5.6.3 Comparison of Finite Element and Test Results

This section presents a comparison of the performance of the LIM as computed by the finite element method, using the model recommended above, and as measured during experiments conducted on the test LIM.

Figure 44 gives a comparison of the computed and experimental results for the thrust and normal forces as a function of speed for various frequencies. The finite element predictions are lower than the experimental results. The degradation of the peak thrust as the frequency of excitation is increased is due to longitudinal end effect. The finite element model predicts the thrust very well in the plugging region, but it is unable to follow the peak of the thrust speed curve in the motoring region. The difference in the results is larger at the higher frequency. The normal force predicted is also low and does not follow the experimental results closely. This is consistent with earlier analysis of normal force using other methods (see Appendix A).

These discrepancies can be attributed to the limitations of the two-dimensional model. While the computed magnitude of the peak thrust is lower, the computed slip at which the maximum thrust occurs compares very well with the experimental results. Similarly, the peak of the computed normal force occurs exactly at synchronous velocity, conforming to expectations. The peak of the thrust-speed curve occurs at 7 Hz slip frequency for the secondary used in the reported experiments, for which a 4.5 mm thick aluminum cap was used. In comparison, the peak of the thrust-speed curve for the LIM with a secondary which has a 2.5 mm thick aluminum cap occurs at 5 Hz slip frequency [7].

A comparison of the thrust and normal forces for three different currents at 28 Hz is presented in Figure 45. The finite-element results are again consistently lower than test results around peak thurst.

A comparison of the airgap flux density distribution at selected slips and frequencies is illustrated in Figures 46 through 48. The flux density obtained by the experiments is the envelope of the distribution over the length of the machine. Each search coil was placed such that it measures the flux density as the average over a tooth and slot. Under constant current conditions, the flux density increases as speed

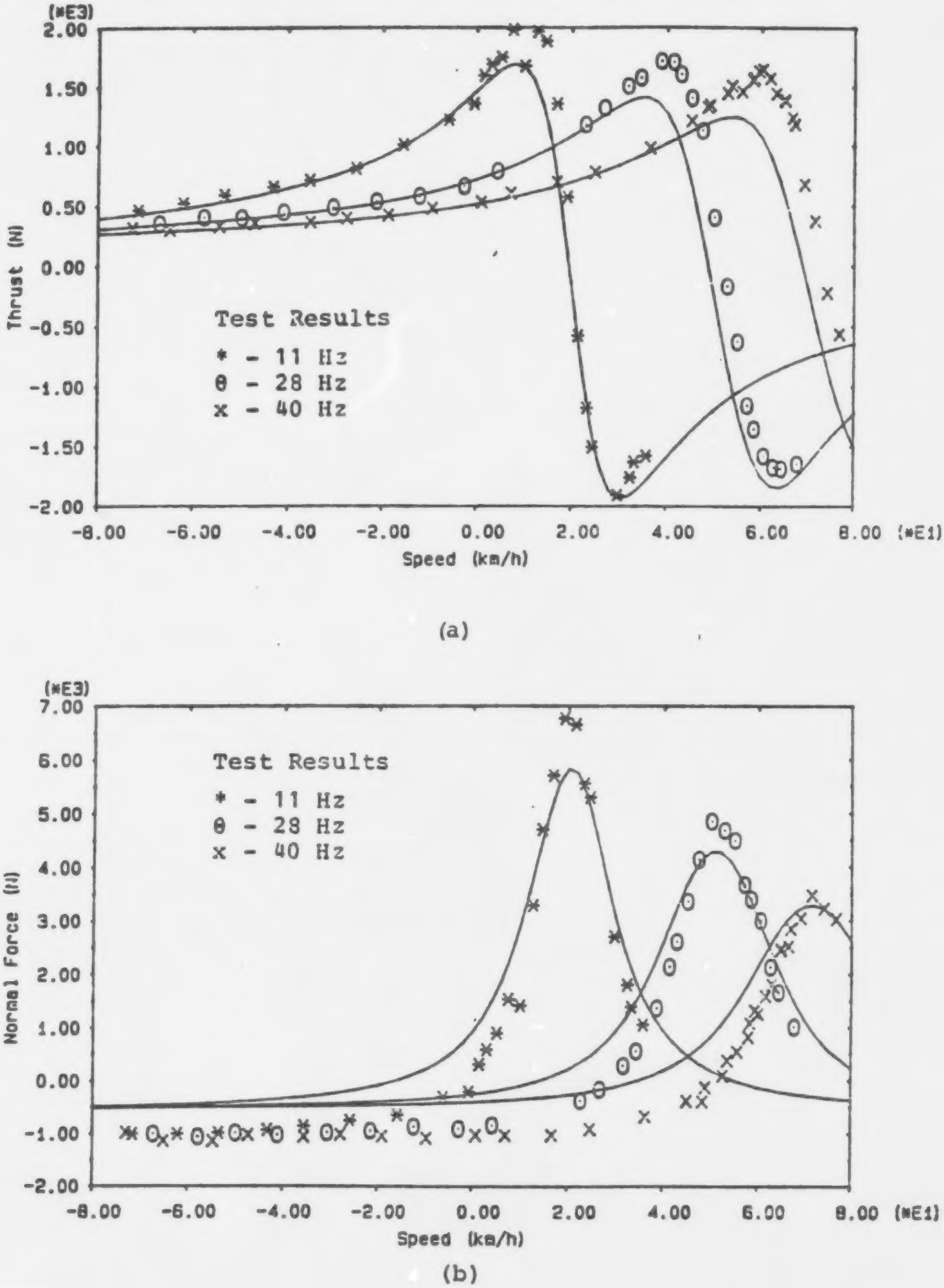

(a)

(b)

Figure 44 Comparison of computed and test results for different frequencies at 200 A, for (a) thrust, and (b) normal force

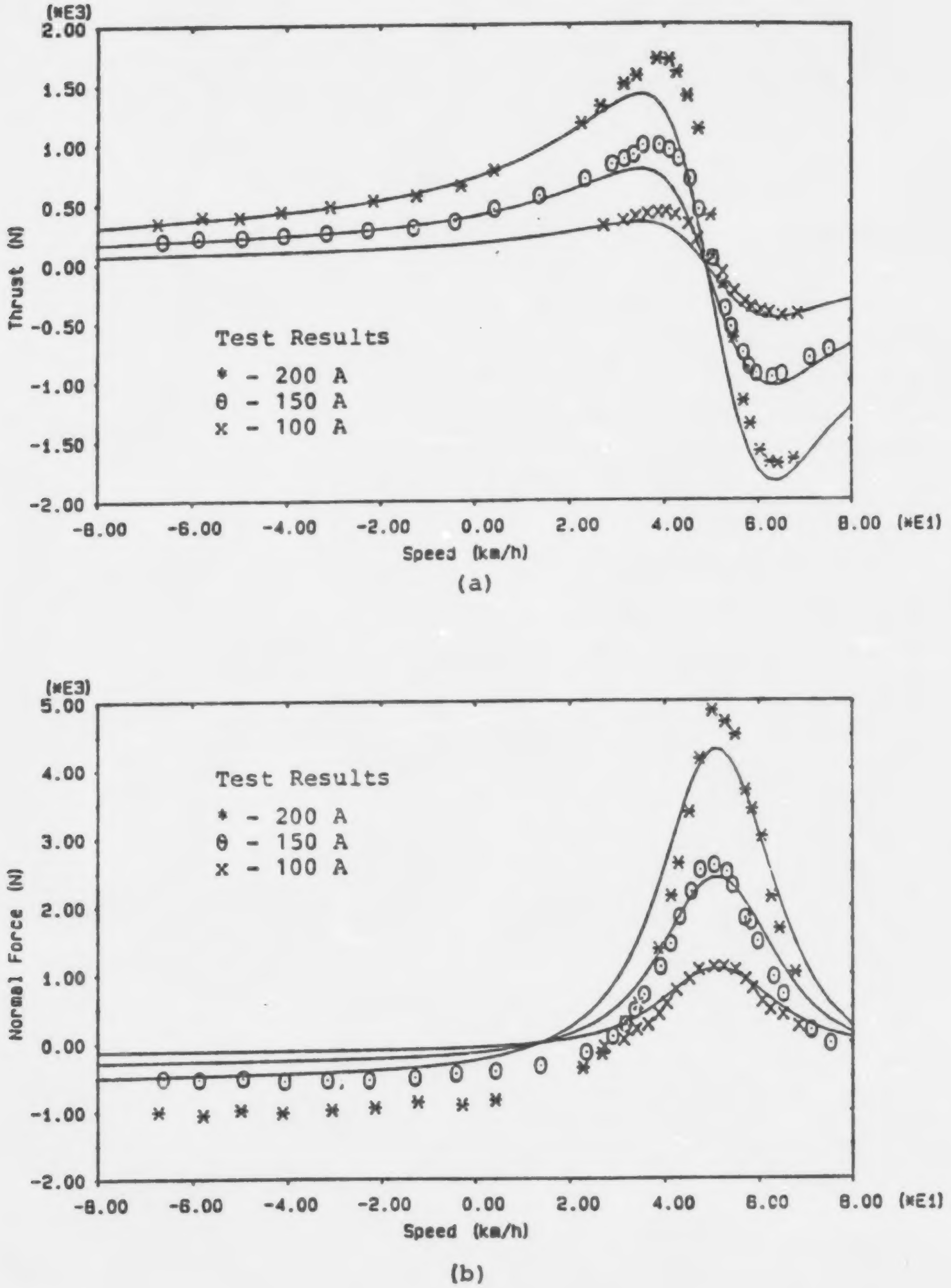

Figure 45 Comparison of computed and test results for different currents at 28 Hz for (a) thrust and (b) normal force

approaches synchronous velocity. The longitudinal end effect is clearly a maximum at synchronous speed and reduces to zero at standstill. The increase in end effect as the excitation frequency is increased can also be noticed in the three synchronous speed flux distributions. Consistent with the predictions of thrust and normal forces, the predicted flux densities are lower than the experimental results, especially at synchronous speed.

The results computed by the finite-element model are shown to compare reasonably well, but are consistently low around peak thrust as compared with test results obtained by experiments on a large-scale test facility at Queen's University.

A two-dimensional finite-element model is considered adequate for most purposes. In order to account for finite width effects, it is necessary to use correction factors, which may affect the accuracy of the computed results. In order to improve the accuracy, it may be necessary to consider a full three-dimensional model. However, three-dimensional finite-element programs have not yet reached the same level of maturity as those for two-dimensional analysis. Moreover, three-dimensional methods are much more complex, and will require substantially longer computation time.

It is considered that the two-dimensional finite-element method provides a sufficient definition of the field distribution in an LIM to justify the use of this technique for analysis of phase unbalance conditions, as reported in the next chapter.

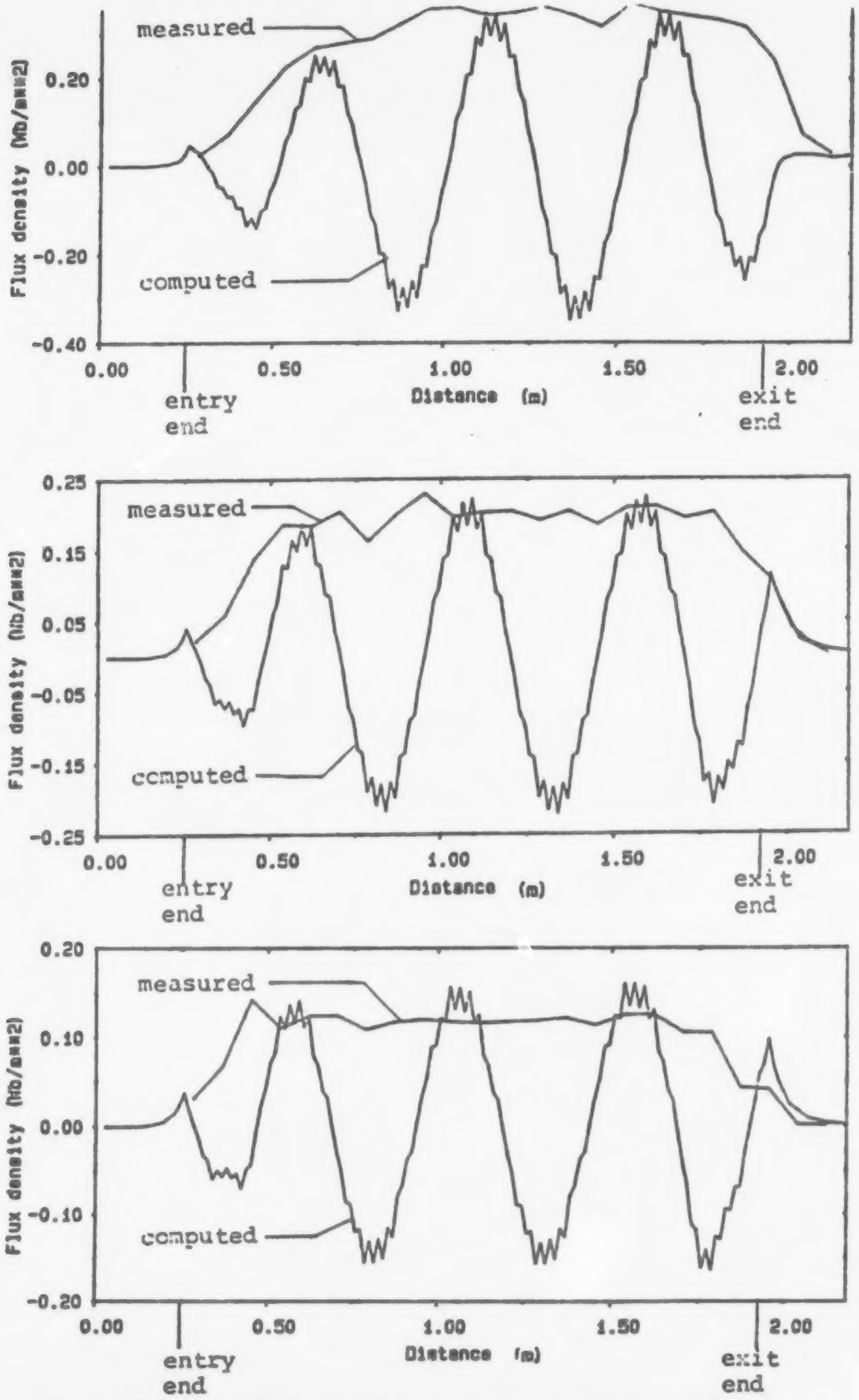

Figure 46 Comparison of computed and test results for flux density for f=11 Hz at slips of (a) 0.0, (b) 0.619 and (c) 1.0

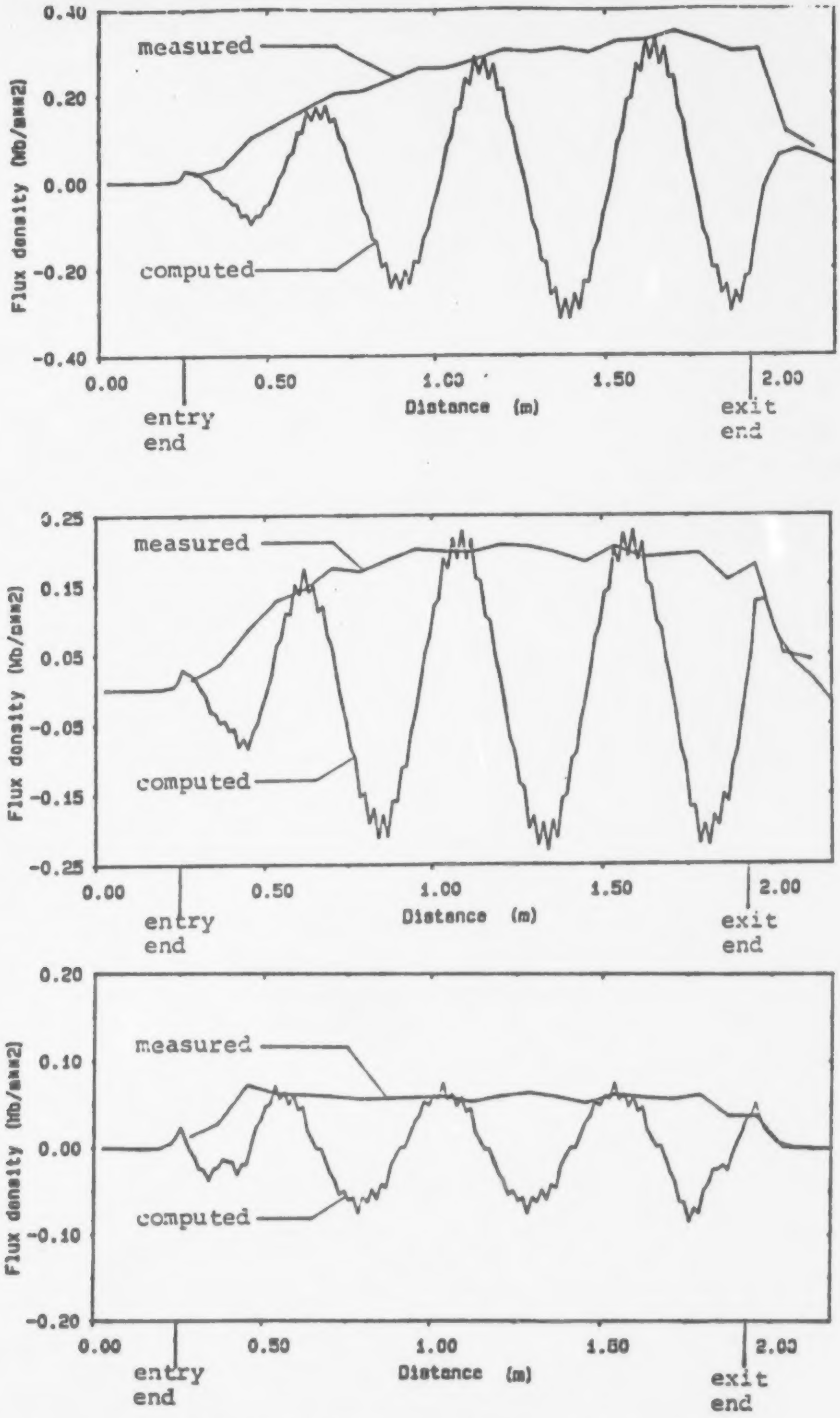

Figure 47 Comparison of computed and test results for flux density for f=11 Hz at slips of (a) 0.0, (b) 0.272 and (c) 1.0

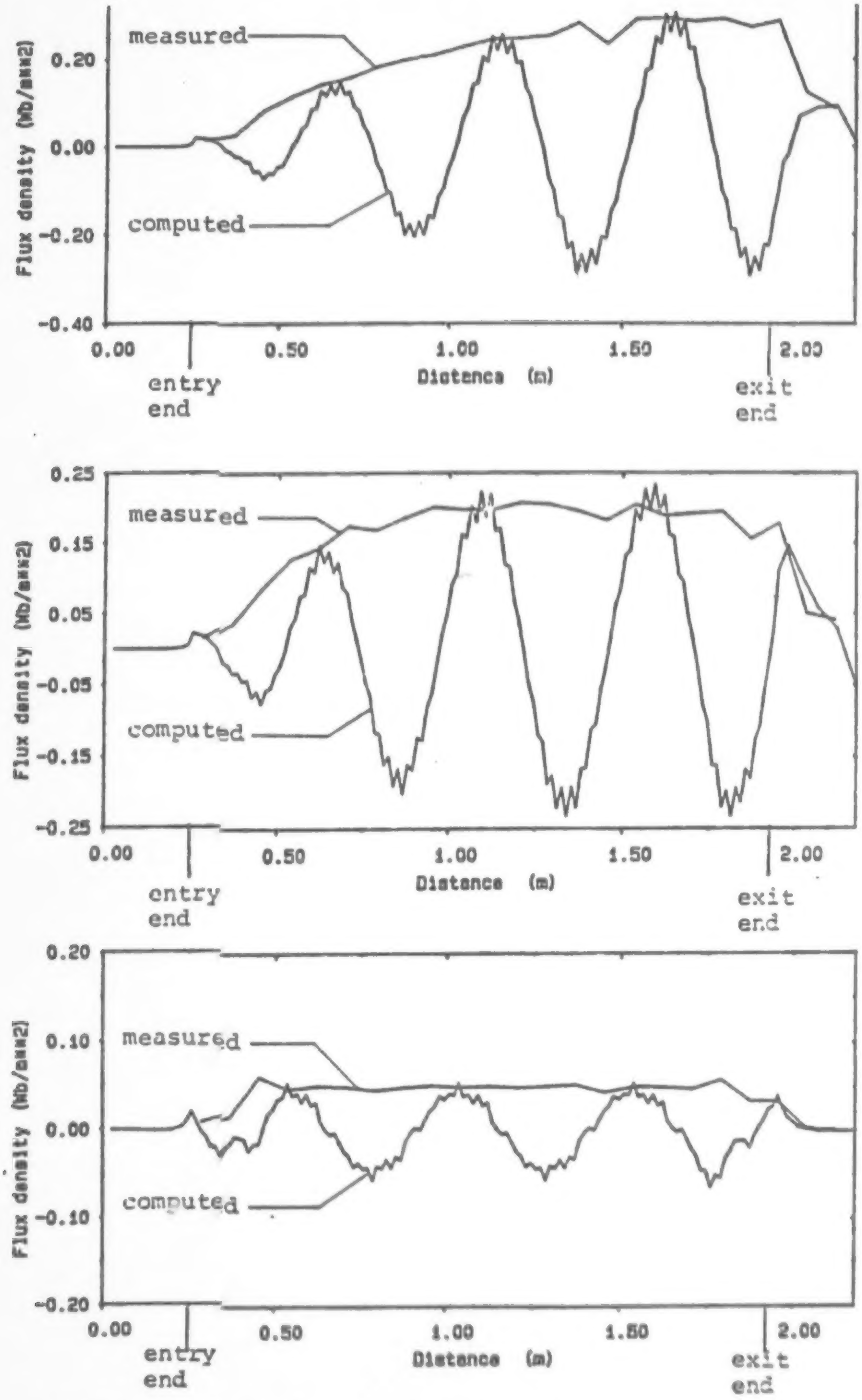

Figure 48 Comparison of computed and test results for flux density for f=11 Hz at slips of (a) 0.0, (b) 0.161 and (c) 1.0

6. PHASE UNBALANCE EFFECTS IN LIMs

6.1 Introduction

The finite element method described in Chapter 5 evaluates the flux distribution in a machine or device, given the excitation current. In most practical situations, however, the excitation voltage is constant, and the excitation current may vary, depending on the operating conditions. The conventional finite-element method is inadequate in this situation. A modification to the finite-element method was introduced recently [42]. In this method, both the current and the flux distribution can be evaluated at same time, for a given excitation voltage. The principles of this method, which has been used for the first time for linear induction machine analysis in this investigation, are described in the following section.

The results of this method applied to the LIM are then compared with experiments performed under constant voltage conditions. Since this method can be used to calculate the currents in a three-phase machine, without the usual assumption that the currents are balanced, it can be used to predict phase unbalance in linear machines. The results of experiments performed to measure phase unbalance are compared with finite element results in this chapter.

6.2 Formulation of the Modified Finite-element Method

In the conventional finite-element method, the electromagnetic field is found by solving the following equation:

$$\nabla \times \nu \nabla \times A = J_s + J_e \tag{6.1}$$

where J_s is the source current density, which is specified, and J_e is the induced current density, which can be expressed in terms of the time and space derivatives of vector potentials. The terminal voltage of a machine can then be found from the known potentials. If the currents are to be found using the conventional finite element method, knowing the applied voltages, an initial set of currents has to be assumed which will then have to be iterated until the specified applied voltages are obtained. This would require several repetitions and a considerable amount of CPU time.

In the modified finite-element method, the source current density is expressed in terms of the phase currents. The matrix equation corresponding to Equation (6.1) can then be expressed as:

$$\begin{array}{cccc} [S'] & \begin{bmatrix} A \\ 1 \end{bmatrix} & = [G] & \quad (6.2) \\ n\mathrm{x}(n+m) & (n+m)\mathrm{x}1 & n\mathrm{x}1 & \text{dimensions of matrices} \end{array}$$

where: S' is the modified S matrix, which includes the relationship between the current at each node to the phase currents, together with geometrical relationships

G is a matrix related to the vector potentials known from Dirichlet boundary conditions.

The terminal voltages are related to the phase currents through the winding impedances. Figure 49 shows the per-phase equivalent circuit of a linear machine. The loop equation for this circuit can be written as:

$$\int_l \partial A/\partial t \; dl + R_p I_{ph} + L_e \, \partial I_{ph}/\partial t = V_{ph} \qquad (6.3)$$

where: l is a contour along the winding in the finite element region, enclosing the total flux in the machine excluding the end winding linkage

L_e is the end winding leakage inductance/phase

R_p is the total primary resistance/phase

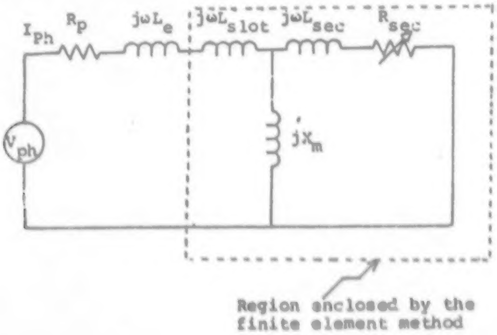

Figure 49 LIM equivalent circuit showing the parameters included in finite element analysis

The first term on the left-hand side is the time derivative of the flux linkage. If there are n conductors in series in each coil, then from Figure 50 we can write the first term of Equation (6.3) as:

$$\int_1 \partial A/\partial t dl. = \Sigma Nw' \partial/\partial t(A_1 - A_2) \qquad (6.4)$$

where: A_1 = average potential in slot 1

A_2 = average potential in the slot 2

n = number of conductors per coil side

w' = width of the primary corrected for fringing (see Appendix A).

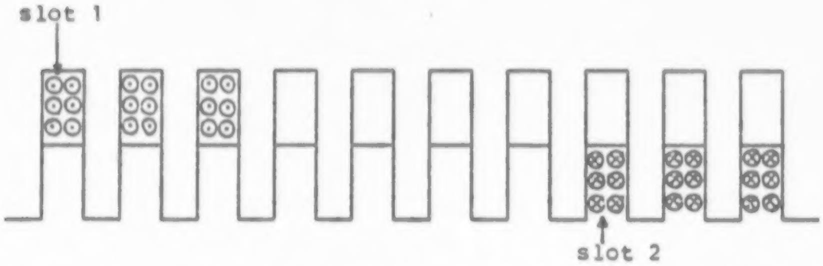

Figure 50 Longitudinal section of LIM showing conductors in one phase

The complex steady-state technique described in Chapter 5 is used in this modified finite-element analysis. Hence, all the time derivatives can be replaced by $j\omega$. Equation (6.3) can therefore be rewritten as:

$$\int_1 j\omega A dl + R_p I_{ph} + j\omega L_e I_{ph} = V_{ph} \qquad (6.5)$$

m equations of the above type may be written for the m phases of a machine. These equations can be expressed in matrix form as:

$$\underset{m\times(n+m)}{[C]} \quad \underset{(n+m)\times 1}{\begin{bmatrix} A \\ I \end{bmatrix}} = \underset{m\times 1}{[V]} \qquad (6.6)$$

The elements of matrix C are constants for a particular frequency. V is the matrix of the specified voltages. Equations (6.2) and (6.6) together produce the required number of equations to solve for all the unknowns.

The final matrix equation will be of the form:

$$\underset{(n+m)x(n+m)}{[D']} \underset{(n+m)x1}{\begin{bmatrix} A \\ 1 \end{bmatrix}} = \underset{(n+m)x1}{\begin{bmatrix} G \\ V \end{bmatrix}} \qquad (6.7)$$

The matrix D is non-symmetrical and, unlike the global matrix in the conventional finite-element method, is banded with edges as shown in Figure 51.

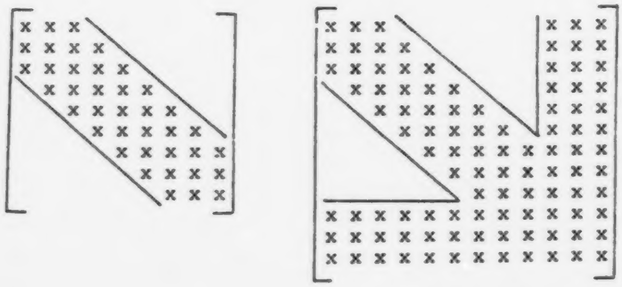

n x n

Conventional finite element method

n+m x n+m

Modified finite element method

Figure 51 Matrix structures of the two finite element methods

The Gaussian elimination method was modified to solve such a matrix. Only a linear case has been treated here, although a nonlinear solution would be a simple extension.

6.3 Computation Model

The discretization shown in Figure 28(b) was used for the analysis described here. The conductivity of the aluminium cap was corrected using the Russell and Norsworthy factor, given by Equation (B.3), and the conductivity of the secondary core was corrected using the factor given by an equation in Appendix A. Thus the model used for the LIM analysis in this chapter includes skin effect, finite length, and finite width effects.

6.4 Constant Voltage Tests

Tests were performed on the large-scale experimental LIM under constant voltage at 60 Hz, over a speed range of -75 to +75 km/h. Finite-element simulation was performed using the method described in the previous sub-section. Figure 52 illustrates a comparison of the experimental and computed results for the thrust and normal forces at 200 V and 160 V (L-L) with 60 Hz excitation. As the synchronous velocity at 60 Hz is above the speed capability of the test wheel, only results in the slip range $1.7 < s < 0.3$ (i.e. in plugging and motoring regions) were accessible.

Figure 52 shows a gradual increase in the thrust as the slip decreases. Under constant voltage conditions, the flux in the machine is constant, hence the thrust-speed characteristic is flatter than under constant current conditions. In the deep plugging region, the normal force is totally repulsive, but as the speed of the LIM approaches the synchronous speed, the normal component of the surface magnetic flux density increases and hence the normal force becomes attractive. The thrust predicted by the finite element compares fairly well with the experimental results, but the normal force predictions do not show good correlation with test data. In particular, the normal force in the plugging region is seen to deviate from the test results. This is because the normal force in the plugging region consists mainly of the repulsive (reaction) component and, as seen in Chapter 5, the finite element predictions for reaction forces are lower than test results. It has to be emphasised again here, that this is considered to be due to the limitations of a two-dimensional model. Slight discrepancy may also be caused by incorrect estimation of the end winding leakage reactance.

6.5 Unbalance Tests

In this method of analysis, the three-phase currents can be computed separately, thus allowing the phase unbalance in the machine to be computed. Figure 53 shows a comparison of the computed and experimental results for the three-phase currents as a function of

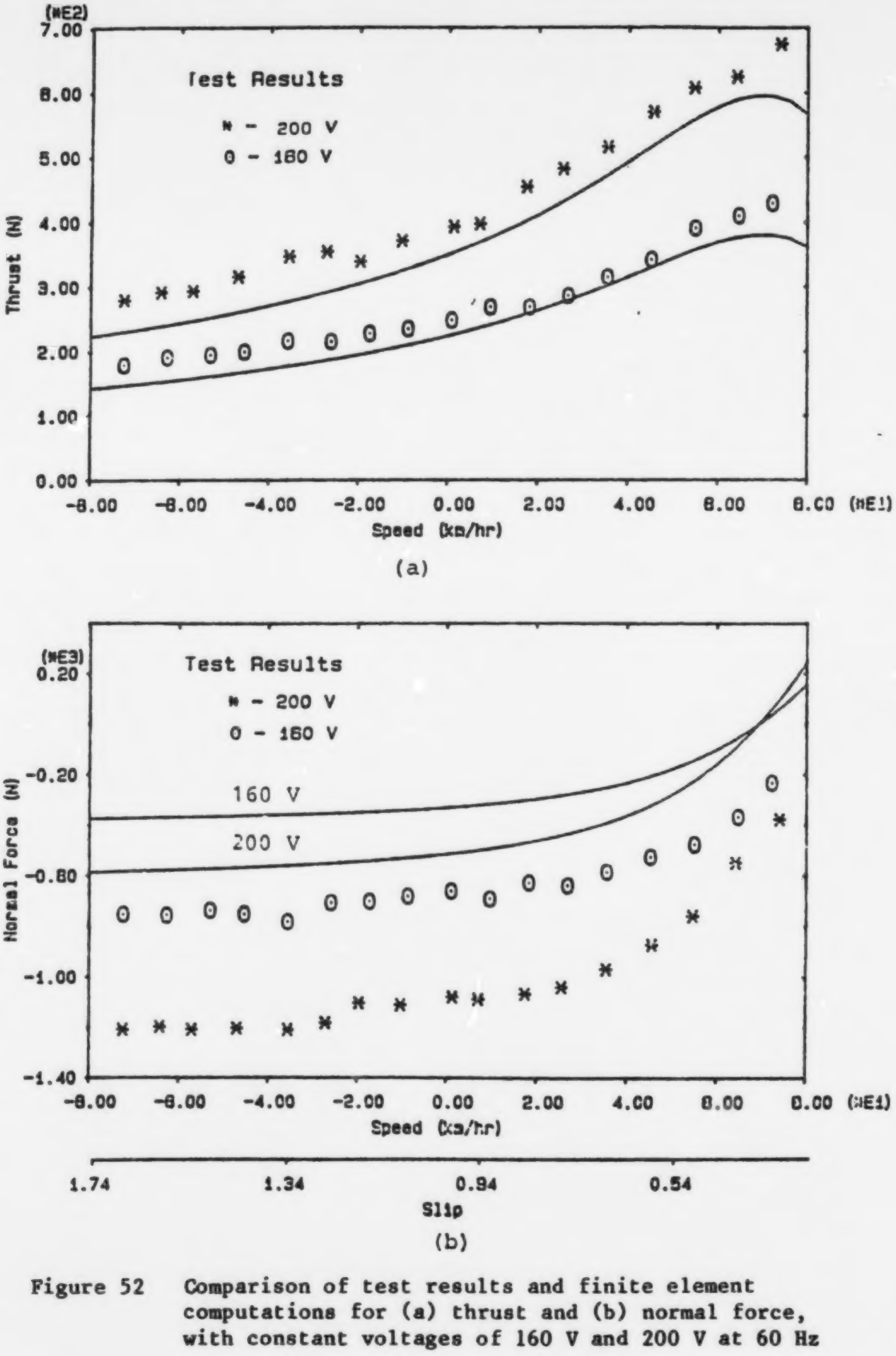

(a)

(b)

Figure 52 Comparison of test results and finite element computations for (a) thrust and (b) normal force, with constant voltages of 160 V and 200 V at 60 Hz

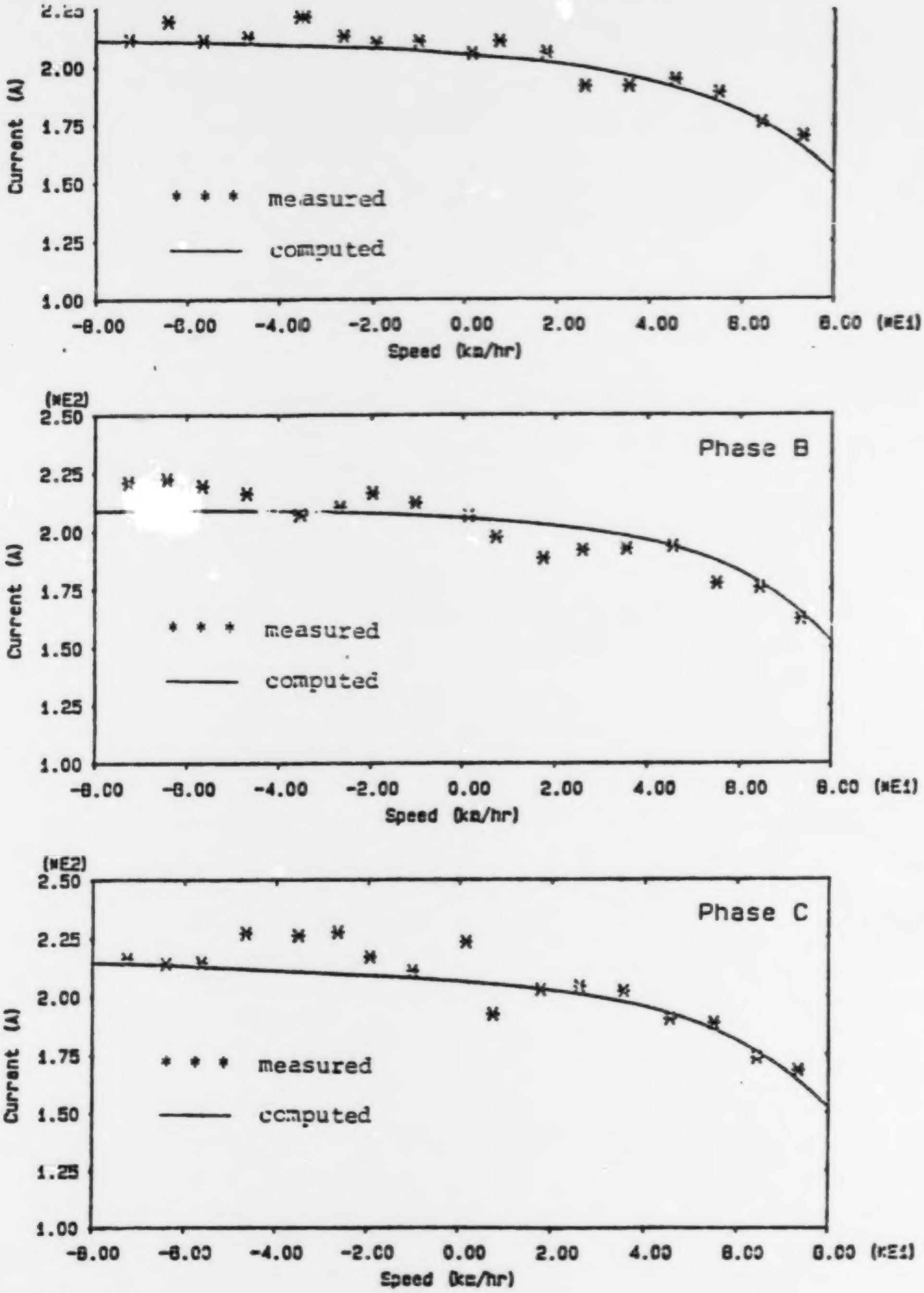

Figure 53 Comparison of test results and finite element computations for phase currents, with a constant voltage of 200 V at 60 Hz

speed with a constant voltage of 200 V at 60 Hz. The current decreases markedly as the speed approaches synchronous velocity. The finite-element predictions are in this case very close to the experimental results. The irregularity in the measured phase currents may be due to slight changes in air gap, or to the applied voltage being not exactly the same each time a measurement was made.

In addition, constant voltage tests were performed at lower frequencies, to compare finite element predictions of phase currents and the observed phase unbalance. Constant voltage tests at three frequencies, namely 11, 28 and 40 Hz, were performed with a constant volts/Hz of 2.67. This corresponds to the lowest voltage available from the inverter at each frequency. This lowest available voltage was used in order to avoid heating of the LIM during the extended periods needed to acquire data.

For analysis of phase unbalance, the individual phase currents were transformed using symmetrical components, and an unbalance factor (U.F.) was defined as the ratio of the negative sequence component to the positive sequence component:

$$\text{U.F.} = -\text{ve sequence component}/+\text{ve sequence component} \qquad (6.8)$$

Figures 54 and 55 show the phase currents and the unbalance factors obtained by experiment and by computation. The currents follow the normal rotary induction machine pattern, remaining at a high value in the plugging and regenerative braking regions, and dropping to a minimum at synchronous velocity. The minimum value, representing the magnetizing current for that frequency, is high because of the large airgap of the LIM. The computed phase currents again compare very well with the experimental results.

At synchronous velocity, the maximum current is in phase A, and the minimum current is in phase B. Both the experimental and computed results show the same trend. The current is a maximum in phase A because it is at the front end of the machine, and hence has a lower flux linkage and hence a low low leakage reactance, due to the asymmetry in the flux distribution caused by end effect. By a similar reasoning, phase C being in the middle, has a higher flux linkage and leakage reactance and hence a lower current, and phase B being the

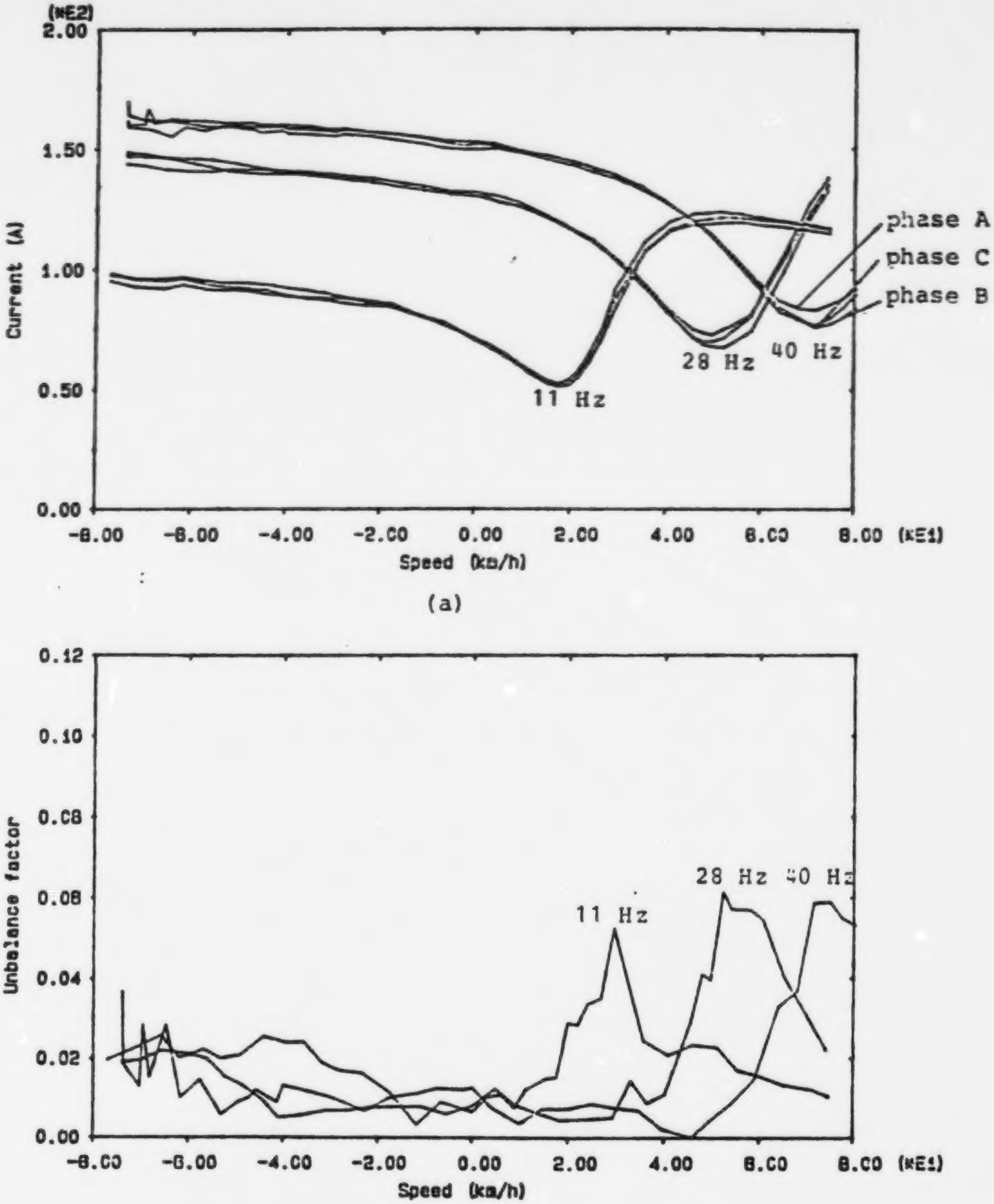

(a)

(b)

Figure 54 Experimental results for (a) phase currents, and (b) the unbalance factor as a function of speed, with constant volts/Hz of 2.67 at 11, 28 and 40 Hz

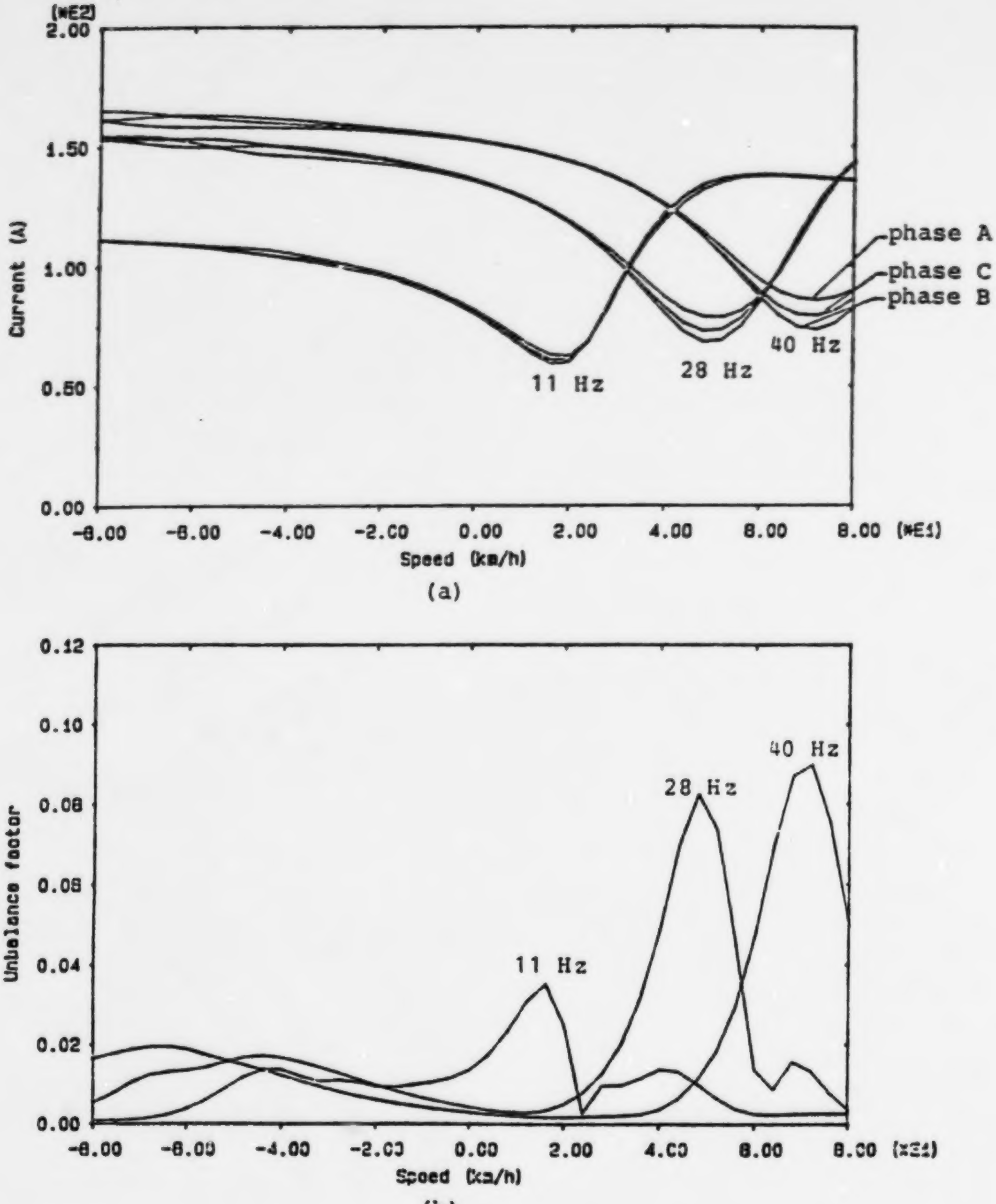

(a)

(b)

Figure 55 Finite element results for (a) phase currents, and (b) the unbalance factor as a function of speed, with constant volts/Hz of 2.67 at 11, 28 and 40 Hz

furthest from the entry end of the machine has the highest flux linkage and leakage reactance and hence the lowest current.

Even though the computed and experimental unbalance factors show the same trend, differences in the amplitude and in the position of the peaks are evident. Experiments show that the maximum unbalance occurs at a speed slightly greater than synchronous speed, whereas the computed results predict that the maximum phase unbalance is at synchronous speed. Phase unbalance, being mainly due to end effect, should be a maximum at synchronous speed according to theory by Yamamura [43]. This conclusion is also consistent with the results published in reference [44]. The unbalance factor should also increase with frequency, in accordance with the increasing end effect. The computed maximum unbalance factor increases more rapidly with frequency than observed experimentally.

It should be noted here that the phase current measurements for the above experiments were made with analogue meters of 5 percent accuracy, with a recommended frequency range of 45-65 Hz. Hence, the needles of the analogue meters were vibrating at the lower frequencies, causing an uncertainty in the experimental results. The phase unbalance for the test machine is fairly small, and hence the accuracy of the meters becomes important. However, the intention here was the show that the trend of the finite element predictions is consistent with observed behaviour of a LIM.

6.6 Effect of Phase Unbalance

In this section, the effect of phase unbalance on mechanical performance will be evaluated. As noted earlier, the effect of unbalanced currents is to produce a backward travelling field which degrades the performance characteristics of the LIM. The backward travelling field produces braking thrust in the motoring region and forward thrust in the plugging region of operation.

To study the effect of phase unbalance on the computed performance of the LIM, the thrust and normal forces were calculated by forcing unbalanced currents on the primary. The complex steady-state method was used for this analysis. The primary was assumed to be star-connected with a floating neutral. Hence, if the magnitude of each of the three phase currents is specified, the phase angle between the phase currents can be found using the cosine formula. The formula for angle a (see Figure 56) is given by:

$$\text{Cos } a = (I_B^2 + I_C^2 - I_A^2)/(2I_BI_C) \qquad (6.9)$$

Similar equations can be written for angles b and c. The phase currents can then be written in phasor form, with phase A as reference, using these angles. The unbalance factor defined by Equation (6.8) may then be obtained by decomposing the phase currents into positive and negative sequence components. When assigning the currents to the nodes in the finite-element method, it was necessary to take into account the fact that the phase angle between the phase currents is not 120 degrees, because the currents are unbalanced.

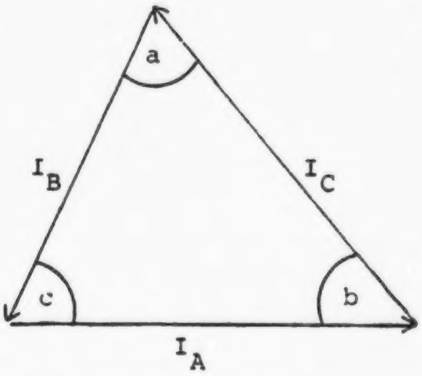

Figure 56 Phasor diagram for star-connected primary

Finite-element computation for the thrust and normal forces were performed for several unbalance factors, keeping the average current constant at 200 A. Following the trend shown by previous experiments and computations, I_A, I_B, and I_C were assumed to have maximum, minimum and average values, respectively. Table 2 shows the magnitude and phase angle of the phase currents for different unbalance factors.

TABLE 2

MAGNITUDE AND PHASE ANGLES OF PHASE CURRENTS FOR DIFFERENT UNBALANCE FACTORS

U.F.	A		B		C	
0.0	200	/0	200	/-120	200	/120
0.1	217.5	/0	182.5	/-120.8	200	/129.4
0.25	242	/0	158	/-124.7	200	/139.5
0.5	275	/0	125	/-138.2	200	/155.4

Average current = 200 A

Figure 57 shows the thrust and normal forces computed for unbalance factors of 0.25 and 0.5 as compared with those for balanced currents. The effect of phase unbalance can be seen to be very small for an unbalance factor of 0.25, but becomes significant for an unbalance factor of 0.5. In practice, unbalance factors above 0.25 are uncommon even for high-speed LIMs. The effect of unbalance is most significant in the plugging and regenerating regions. This can be explained by examining Figure 58, which shows the thrust and normal forces due to positive and negative sequence currents and their sum. It is evident that the shape of the curves predicted by finite element method follows this pattern. The negative thrust produced by the unbalanced currents drop off rapidly in the normal motoring region, and hence the effect of unbalanced currents is lower near peak thrust than in the plugging region. For higher frequencies, the peaks of the thrust and normal forces occur at a higher velocity, and hence unbalanced currents will have a lesser effect on peak thrust as the frequency increases.

To study the degradation of thrust with increase in phase unbalance, the peak thrust was computed for 6, 11, 28, and 40 Hz as a function of unbalance factor. Figure 59 illustrates this dependence, and it is evident that the peak thrust is degraded more significantly at the lower frequencies. In particular, the peak thrust for 6 Hz is negligibly small for an unbalance factor of 1.0, because the peaks of both the positive and negative sequence components, which are equal in magnitude, occur at standstill. The curves are flat for small

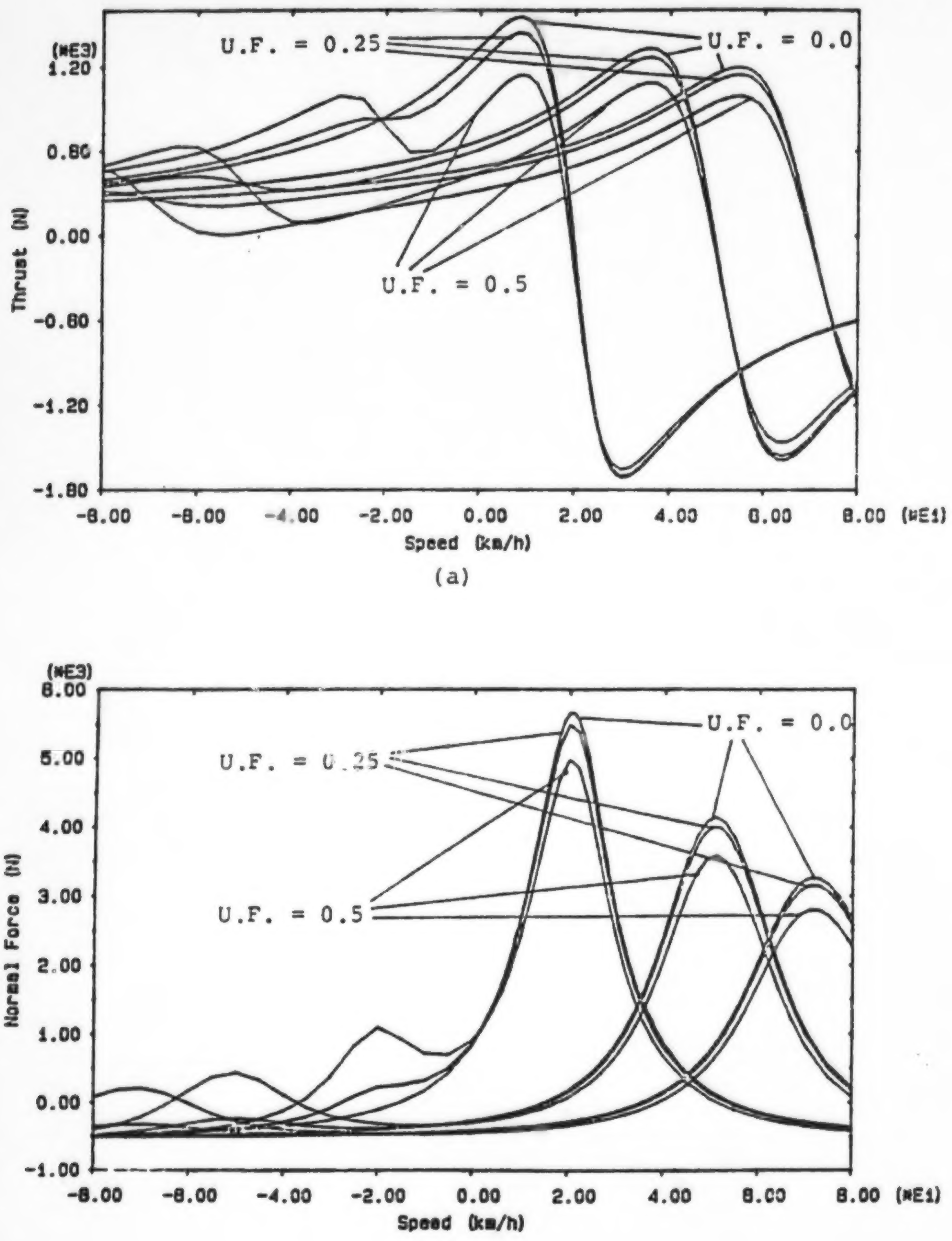

(a)

(b)

Figure 57 (a) Thrust and (b) normal force for f=11, 28 and 40 Hz, for unbalance factors of 0, 0.25 and 0.5

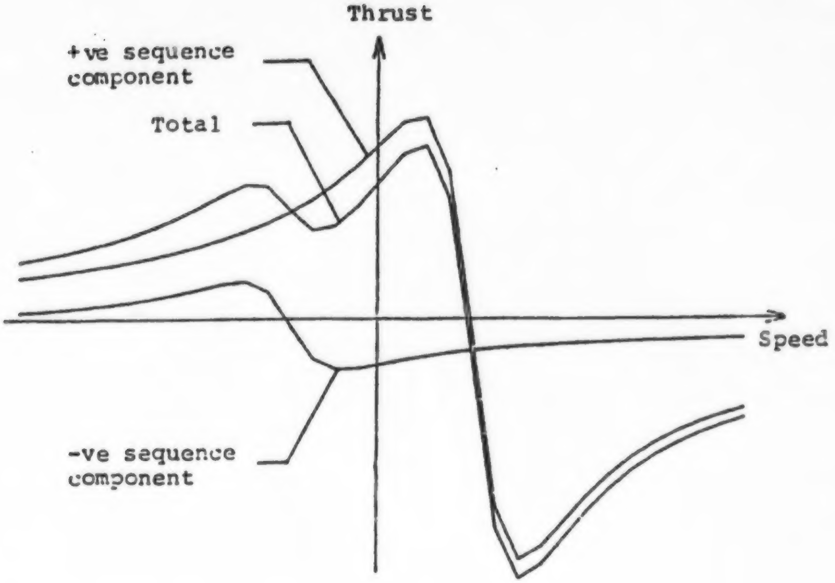

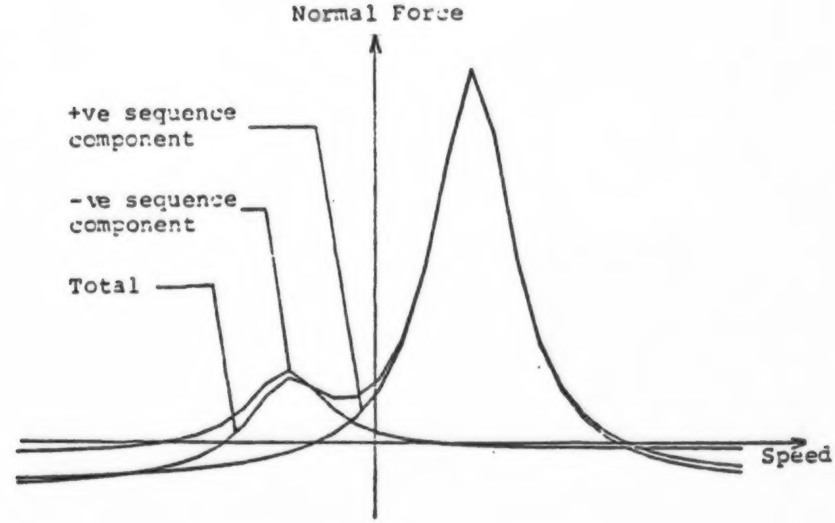

Figure 58 Expected pattern of thrust and normal forces and their sum as a function of speed for positive and negative sequence currents

unbalanced factors, indicating that the effect of unbalance for small unbalance factors up to about 0.1 is insignificant.

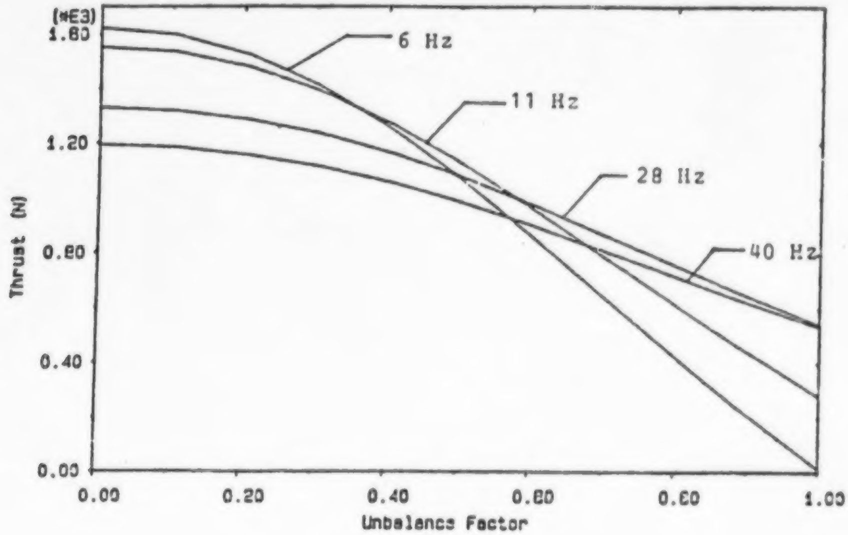

Figure 59 Peak thrust as a function of unbalance factor for f=6, 11, 28 and 40 Hz

6.7 Review of Phase Unbalance Effects

A method for predicting phase unbalance was developed in this chapter. This method is a modified form of the conventional finite-element method in which the currents are also treated as unknowns together with the nodal vector potentials. It was shown that this method predicts the speed dependence of the phase currents under constant voltage conditions very well.

It was shown that phase unbalance is a function of speed, and that it is maximum near synchronous velocity and minimum at standstill. The effect of phase unbalance on mechanical performance of the LIM was found to be negligible for unbalance factors up to about 0.1. Moreover, the effect of phase unbalance is most significant at standstill and in the plugging region. Fortunately, while phase unbalance increases with velocity, the effect of phase unbalance on performance decreases with velocity.

Phase unbalance is caused mainly by longitudinal end effect. Therefore, in order to reduce phase unbalance, end effect has to be reduced, and the distribution of the field has to be made more uniform over the length of the machine. Several techniques for reducing end effect have been discussed (e.g. reference [43]), usually by the introduction of compensation windings at the entry and exit ends. However, compensation windings require graded laminations, which will entail additional stamping costs. It is unlikely to be worthwhile to consider compensating windings if the unbalance factor is less than 0.25. Thus low-speed LIMs, e.g. for urban transit, should retain the simplicity of a uniform phase winding distribution, and compensating windings should be considered only for high-speed LIMs.

The starting performance of an LIM can be degraded by unbalance, but in a well-designed machine this unbalance (caused by asymmetry in the windings) should be minimal. In the test LIM, the unbalance at standstill was measured to be less than 2 percent, producing negligible degradation in performance.

7. REVIEW AND CONCLUSIONS

7.1 Review of Activities

This investigation and report have provided analyses and evaluations of the effects of time harmonics and phase unbalance on the performance of linear induction drives.

7.1.1 Time Harmonics

Before investigating the harmonic behavior of LIM drives, control PWM techniques and the harmonic analysis of PWM waveforms was reviewed.

It was shown that, using digital techniques, the output waveforms of a PWM inverter can be generated and harmonically analyzed for the following modulation techniques:

- natural sampling
- regular sampling

It was noted that the natural sampling inherently introduces a variable degree of asymmetry into the modulating process, whereas uniform sampling results in symmetrical modulation. This ability of regular sampling to unambiguously define the pulse configuration precisely is of considerable advantage in harmonic cancellation, and provides considerable scope for future development of new inverter-induction drive systems.

The harmonic spectra obtained were used in the analysis of time harmonic effects in the linear induction motor. The inverter waveforms used in the experimental study of the LIM could be generated by simulating the step modulation employed in the inverter, and the harmonic spectra obtained were compared with the actual ones measured using the spectrum analyzer, with excellent agreement.

The harmonic behaviour of a rotary induction machine with regard to current, losses, and efficiency was then discussed. The PWM model was combined with the equivalent circuit machine model to simulate the dynamic operation of a drive.

The thrust and normal forces in a SLIM due to time harmonics in the input waveforms were measured experimentally, using a 64-channel microcomputer-based data acquisition system, and verified analytically. Higher time harmonics are strongly damped inside the steel core of the secondary, in comparison with the fundamental of the gap field. In practice, it has been shown from the tests and analytical verification that higher time harmonics have effectively no influence on thrust. The total thrust due to higher time harmonics can either add to or subtract from the thrust due to the fundamental of the field, depending on the magnitude of harmonics of order 6k+1 in comparison with the magnitude of those of order 6k-1. Any degradation or improvement in thrust due to PWM excitation of an LIM is very small, either with an aluminum-capped or solid-steel reaction rail. The dominant effect of PWM over sinusoidal excitation is a higher level of noise (both acoustic and electromagnetic) and somewhat higher primary losses.

The equivalent circuit method, with mutual and secondary parameters evaluated from two-dimensional field analysis with appropriate correction factors for edge, end and saturation effects, provides an effective tool for the calculation of LIM performance. It gives analytical results which are very close to the test data, as illustrated in Figures 20, 21, 25 and 26. The PWM model, in conjunction with the LIM model, enables one to evaluate the harmonic effects conveniently by feeding the carrier ratio and modulation index of the inverter used. This technique can be used for design studies of LIMs for transportation applications under constant voltage or under constant current excitation conditions for double-layer or single-layer secondary.

7.1.2 Phase Unbalance

A two-dimensional finite-element analysis was shown to predict the performance characteristics of linear induction machines fairly well. Comparison with experimental results has shown that the predictions of mechanical forces and of the magnitude of the airgap field are low by 10-15 percent. An improvement in the prediction capability may require the use of higher-order elements or a full three-dimensional analysis of the LIM.

The finite-element model incorporates all the principal factors that affect the performance of LIMs such as speed and time dependence of induced currents, slotted geometry, nonlinearity of magnetic material, and longitudinal and transverse edge effects. The finite-element model, using the complex steady state solution, was shown to produce a satisfactory representation of machine performance over a wide range of operating conditions.

The conventional finite-element method was modified to analyze linear induction motors with balanced voltage rather than balanced current excitation. Comparison with tests have shown that this finite-element method produces good results for the speed dependence of phase currents. The principal advantage of this method is that it can be used to predict phase unbalance under any operating condition. Phase unbalance, being related to the longitudinal end effect, was shown to be a maximum close to synchronous speed. While a difference in magnitude was evident, the trend of the results for unbalance predicted by finite-element analysis agreed with that found experimentally. The effect of phase unbalance on mechanical performance was evaluated, and was found to be insignificant, for differences in the phase currents of up to 10 percent. It was found that, for a specified unbalance, the degradation in performance decreases as the velocity increases.

7.2 Conclusion

It is considered that the objectives of the work reported here, as detailed in Section 1.4, have been fully realized.

It has been shown that time harmonics in voltage excitation have essentially no effect on the mechanical performance of the LIM drive, apart from a marginal decrease in efficiency.

It has been noted that the dominant effects of inverter driven LIMs are related to acoustic and electromagnetic noise. Experience has shown that the inverter itself is the greater source of acoustic noise, and steps should be taken to acoustically isolate the power electronics from the passenger compartment of a transportation vehicle. The dc bus inductor is the major source of acoustic noise in a thyristorized inverter. This noise can be reduced considerably if a power conditioner with GTO thyristors is used. With regard to electromagnetic interference, the inverter carrier frequency and modulation strategy must clearly be selected to avoid any interference with track control circuits and wayside communication facilities.

With regard to phase unbalance, it is concluded that this feature of LIM operation and its effects are unlikely to be of sufficient magnitude to significantly degrade the performance of low-speed LIMs, such as those used for urban transit. Therefore a uniformly wound machine with a uniformly slotted primary lamination stack appears to be entirely adequate. For high-speed LIMs, however, the dominance of the longitudinal end effect may cause substantial phase unbalance in a uniformly wound machine. Under these conditions the use of compensating windings to more closely balance the phase impedances will likely be beneficial.

REFERENCES

1. Canadian Maglev Group (Ed. A.R. Eastham). Electrodynamic Suspension and Linear Synchronous Motor Propulsion for High-Speed Guided Ground Transportation. CIGGT Report No. 77-13, September 1977.

2. Hayes, W.F. High Speed Electrodynamic Maglev Guided Ground Transportation Systems Conceptual Design Study. NRC Report No. LTR-CS-176, September 1977.

3. Eastham, A.R., G.E. Dawson, D.L. Atherton, and C.L. Schwalm. Data Report for the Study of a SLIM as an Integrated Suspension/Propulsion System. CIGGT Report No. 79-3, January 1979.

4. Katz, R.M. Integrated Suspension and Propulsion of Guided Ground Transportation Vehicles with a SLIM. Report No. UMTA-VA-06-0035-79-1, January 1979.

5. Eastham, A.R., C.L. Schwalm, K.A. Lancaster, and W.D. Watson. Evaluation of the Dynamic Braking Performance of a Single-Sided Linear Induction Motor with a Cage Reaction Rail. CIGGT Report NO. 79-10, June 1979.

6. Katz, R.M. Linear Induction Machine with Solid Iron Reaction Rail for Integrated Magnetic Suspension and Propulsion. Report No. UMTA-VA-06-0068-80-1, January 1981.

7. Eastham, A.R., G.E. Dawson, D.M. Pringle and J.A. Davidson. Comparative Experimental Evaluation of the Performance of a SLIM with Solid Steel Reaction Rail and with an Aluminum-Capped Reaction Rail. CIGGT Report No. 80-7, December 1980.

8. Eastham, A.R., G.E. Dawson, V.I. John, A.M.A. Kamar, P.C. Sen and A.K. Wallace. "Voltage-Controlled 60 Hz Linear Induction Drives." Electric Machines and Power Systems, 1983, 8, (6), pp. 487-97.

9. Dawson, G.E., A.R. Eastham, V.I. John, P.C. Sen, A.M.A. Kamar and D.M. Pringle. A Technical Evaluation of a Variable-Voltage Fixed-Frequency LIM Propulsion System for ICTS. Department of Electrical Engineering Report No. EE-S-82-1, Queen's University, April 1982.

10. Bowes, S.R., and B.M. Bird. "Novel Approach to the Analysis and Synthesis of Modulation Processes in Power Converters." Proc. IEE, 1975, 122, (5), pp. 507-513.

11. Rajashekara, K.W., and J. Vithayathil. "Harmonics in Voltage-Source PWM Inverters." Int. Journal of Electronics, 1981, Vol. 50, No. 5, pp. 325-337.

12. Bowes, S.R., and R.R. Clements. "Computer-Aided Design of PWM Inverter Systems." Proc. IEE, 1982, 129, (1), pp. 1-17.

13. Grant, T.L., and T.H. Barton. "Contro Strategies for PWM Drives." IEEE-IAS, Conference Record, 79CH1484-51A, 1979, pp. 780-785.

14. Bowes, S.R. "New Sinusoidal Pulse Width Modulated Inverter." Proc. IEE, 1975, 122, (11), pp. 1279-1285.

15. Bowes, S.R., and M.J. Mount. "Microprocessor Control of PWM Inverters." IEE Proc. B, Electr. Power Appl., 1981, 128, (16), pp. 293-305.

16. Grant, T.L., and T.H. Barton. "A Highly Flexible Controller for a Pulse Width Modulation Inverter." IEEE-IAS, Conference Record, 78CH1346-61A, 1978, pp. 486-492.

17. Operation manual of the Reliance 200 kVA inverter.

18. Lipo, T.A., and P.C. Krause. "Stability Analysis of a Rectifier-Inverter Induction Motor Drive." IEEE Trans. PAS, 1969, Vol. PAS-88, pp. 55-66.

19. Klingshirn, E.A., and H.E. Jordan. "Polyphase Induction Motor Performance and Losses on Non-Sinusoidal Voltage Sources." IEEE Trans. Power Apparatus and Systems, 1968, Vol. PAS-87, No. 3, pp. 624-631.

20. Slemon, G.R., and S.B. Dewan. "Harmonic Modelling for Induction Motors Including Saturation Effects." IEEEE-IAS, 75CH0999-31A, 1975.

21. Jain, G.C. "The Effect of Voltage Waveshape on the Peforamnce of a 3-Phase Induction Motor." IEEE Trans. Power Apparatus and Systems, 1964, Vol. PAS-83, pp. 561-566.

22. Lipo, T.A., and P.C. Krause. "Analysis and Simplified Representations of a Rectifier-Inverter Induction Motor Drive." IEEE Trans. Power Apparatus and Systems, 1969, Vol. PAS-88, pp. 588-596.

23. Krause, P.C. "Methods of Multiple Reference Frames Applied to the Analysis of Symmetrical Induction Machinery." IEEE Trans. Power Apparatus and Systems, 1968, Vol. PAS-87, pp. 218-227.

24. Murphy, J.M.D. Thyristor Control of AC Motors. Pergamon Press, 1973.

25. Rahman, M.A. "Efficiency of Inverter-Fed Induction Motors." IEEE-IAS, Conference Record, 80CH1575-0, 1980, pp. 1286-1291.

26. Chalmers, B.J., and B.R. Sankar. "Induction Motor Losses Due to Non-Sinusoidal Supply Waveforms." Proc. IEE, 1968, 115, (12), pp. 1777-1782.

27. Paszek, W., B. Sliwa and T. Sztajer. "Performance of a Flat Single-Sided Linear Motor Fed From Non-Sinusoidal Voltage Source." (in Polish). Maszyny Elektryczne-Zeszyty Problemowe, 1976, 24, pp. 51-60.

28. Nicolas, A., and G. Rojat. "An Analytical Theory of Single-Sided Linear Induction Motor with Solid Iron Back Yoke and Variable Frequency Drive." Proceedings of ICEM, 1980, Athens, Vol. 1, pp. 84-92.

29. John, G. Time Harmonics in Linear Induction Drives. M.Sc. Thesis, Queen's University, July 1985.

30. Eastham, A.R., G.E. Dawson, C.L. Schwalm. "The Testing of a Single-Sided Linear Induction Motor with Squirrel-Cage and Solid Steel Reaction Rails." ICEM, 1980, pp. 146-153.

31. Sankaran, R., K.P.P. Pillai and K.A. Muraleedharan. "Voltage-Fed Operation of Linear Induction Motors Under Conditions of Supply Unbalance." Proceedings IEE, Vol. 126, No. 4, pp. 293-97, April 1979.

32. Papageorgiou, C. "Linear Induction Motor Under An Unbalanced Three-Phase Voltage." Proceedings ICEM'80, Athens, Vol. 1, pp. 93-101, September 1980.

33. Gierozak, E., J. Fleszar and J. Tuvouski. "Current Asymmetry in the Three-Phase Linear Motor." ICEM'82, Budapest, Vol. 3, pp. 961-3, September 1982.

34. Deleroi, W. "Unbalanced Terminal Voltages and Currents in the Short Primary Linear Induction Motor." Proceedings ICEM'80, Athens, Vol. 1, pp. 136-45, September 1980.

35. Deleroi, W., and G.C. Paap. "Effects of Unbalanced Leakage Reactances of Linear Motors." Proceedings ICEM'82, Budapest, Vol. 3, pp. 964-7, September 1982.

36. Yegnanarayanan, S.S., and M. Suryaprakasa Rao. "Analysis of Linear Induction Motor Imbalance Characteristics." Proceedings ICEM'82, Budapest, pp. 1089-93, September 1982.

37. Silvester, P., and M.V.K. Chari. "Finite Element Solution of Saturable Magnetic Field Problems." IEEE Transactions on Power Apparatus and Systems, Vol. PAS-89, No. 7, pp. 1642-51, September/October 1970.

38. Chari, M.V.K., and P. Silvester. "Analysis of Turboalternator Magnetic Fields by Finite Elements." IEEE Transactions on Power Apparatus and Systems, Vol. PAS-90, No. 2, pp. 454-64, March/April 1971.

39. Demerdash, N.A., and T.W. Nehl. "An Evaluation of the Methods of Finite Elements and Finite Differences in the Solution of Nonlinear Electromagnetic Fields in Electrical Machines." IEEE Transactions on Power Apparatus and Systems, Vol. PAS-98, No. 1, pp. 74-87, January/February 1979.

40. Chari, M.V.K. "Finite-Element Solution of the Eddy-Current Problem in Magnetic Structures." IEEE Transactions on Power Apparatus and Systems, Vol. PAS-93, pp. 62-72, 1973.

41. Minnich, S.H., S.C. Tandon and D.R. Atkinson. "Comparison of Two Methods for Modelling Large-Signal Alternating Magnetic Fields Using Finite Elements." IEEE Transactions on Power Apparatus and Systems, Vol. PAS-103, No. 10, pp. 2953-60, October 1984.

42. Nakata, T., and N. Takahashi. "Direct Finite Element Analysis of Flux and Current Distributions Under Specified Conditions." IEEE Transactions on Magnetics, Vol. MAG-18, No. 2, pp. 325-30, March 1982.

43. Yamamura, S. Theory of Linear Induction Motors. John Wiley and Sons, New York, 1972.

44. Gieras, J.F., A.R. Eastham and G.E. Dawson, "Influence of Phase Unbalance on the Thrust of a Single-Sided Linear Industrion Motor." Submitted for publication.

45. Russell, R.L. and K.H. Norsworthy. "Eddy Currents and Wall Losses in Screened Rotor Induction Motors." Proceedings IEE, Vol. 105A, pp. 163-75, 1958.

46. Strang, G., and G.F. Fix. An Analysis of the Finite Element Method. Prentice-Hall, 1973.

47. Zienkiewicz, O.C. The Finite Element Method in Engineering Science. McGraw-Hill, London, 1971.

48. Silvester, P.P., and R.L. Ferrari. Finite Elements for Electrical Engineers. Cambridge University Press, Cambridge, 1983.

49. Ong, K.J.R. "Finite Element Analysis of a Linear Homopolar Synchronous Motor." M.Sc. Thesis, Department of Electrical Engineering, Queen's University, Kingston, 1983.

APPENDIX A

54 IEEE TRANSACTIONS ON MAGNETICS, VOL. MAG-22, NO. 1, JANUARY 1986

Performance Calculation for Single-Sided Linear Induction Motors with a Double-Layer Reaction Rail Under Constant Current Excitation

JACEK F. GIERAS, MEMBER, IEEE, GRAHAM E. DAWSON, MEMBER, IEEE, AND
ANTHONY R. EASTHAM, SENIOR MEMBER, IEEE

***Abstract*—A method for computing the performance of a single-sided linear induction motor (SLIM) with a double-layer reaction rail, under constant current excitation, is presented. This method takes into account the reaction of secondary eddy currents on the airgap field, transverse edge and longitudinal end effects, together with skin effect, saturation, nonlinear magnetic permeability, and hysteresis in the solid steel core of a reaction rail. In an equivalent circuit of the machine, the mutual and secondary impedances are found from a solution of the two-dimensional electromagnetic field distribution. Modifying factors account for configurations in which the width of the secondary conductive layer is different from that of the steel core, and in which the thickness of the conductive overhand is different from that over the steel core. Good correlation is obtained between analysis and test results from a large-scale linear induction motor (LIM) at Queen's University. The developed expressions are appropriate for small and large LIM's and may also be used for constant voltage excitation conditions.**

INTRODUCTION

THE SINGLE-SIDED linear induction motor (SLIM) provides both wheeled and noncontact vehicles with a low maintenance adhesion-free means of propulsion and braking [1]-[5]. As further applications for SLIM's are examined, there will be a growing need for analytical tools which will not only accurately predict the performance of a machine of given design but which will allow the computer-aided design of a machine to a given set of specifications. The SLIM with a solid steel reaction rail fed from a constant current source has already been analyzed by the authors [6]. Comparative tests [7] have shown that a secondary consisting of a conductive (usually aluminum) cap over laminated (or solid) steel core produces the greatest thrust with the highest efficiency-power factor ($\eta \cos \phi$) product and with the lowest normal force. This reaction rail is, therefore, favored for noncontact traction purposes.

The purpose of this paper is to present a versatile method for calculating the performance of a SLIM with an aluminum-capped reaction rail. This configuration is analogous to that in a rotating induction motor with double-layer rotor [8]-[10]. Although many analyses for linear induction machines with layered secondaries have been published [2], [11]-[16], the methods are not always appropriate for design studies of transportation SLIM's. Analytical results are usually not close to measured values over a wide range of operating conditions because of neglected or inadequate treatment of skin, edge and end effects, magnetic saturation, and hysteresis. Commonly used correction factors are not sufficiently accurate at high levels of excitation when parts of the magnetic circuit are driven into saturation.

In this paper we show that the performance of a SLIM can be evaluated from an equivalent circuit which is very similar to that commonly used for the rotating machine. Mutual and secondary parameters are derived from an evaluation of the two-dimensional field in a longitudinal section of the machine, and are speed and slip frequency dependent. Generally applicable and validated correction factors are presented to account for the finite length and width of the machine and for the geometry and electromagnetic properties of the reaction rail.

ANALYTICAL APPROACH

From a computational point of view, the calculation of the two-dimensional field in a longitudinal section of a SLIM is preferable to a full three-dimensional analysis and is entirely adequate for SLIM performance evaluation. In this way we avoid double Fourier series and space harmonics along the primary slots (in the y direction). In two-dimensional analysis the currents flow only in the y direction, and the magnetic flux density has only two components; perpendicular B_{mz} and parallel B_{mx} to the direction of motion (x direction). A section of the machine to be analyzed is shown in Fig. 1.

The double-layer reaction rail of a SLIM comprises an aluminum cap over laminated or solid steel core. The core serves to carry the airgap flux and to reduce the magnetizing current of the machine. Lamination of the core, as opposed to the use of solid steel, improves the performance, particularly for low-speed running. However lamination is expensive and is not cost effective for sections of the guideway in which a LIM is operated at intermediate or high speed due to end effects [17].

When the secondary core is formed from solid material, this layer will also carry slip frequency induced currents.

Manuscript received September 12, 1984; revised May 24, 1985. This work was supported by the Natural Sciences and Engineering Research Council (NSERC) of Canada.

The authors are with the Department of Electrical Engineering, Queen's University, Kingston, Ontario, Canada K7L 3N6.

0018-9464/86/0100-0054$1.00 © 1986 IEEE

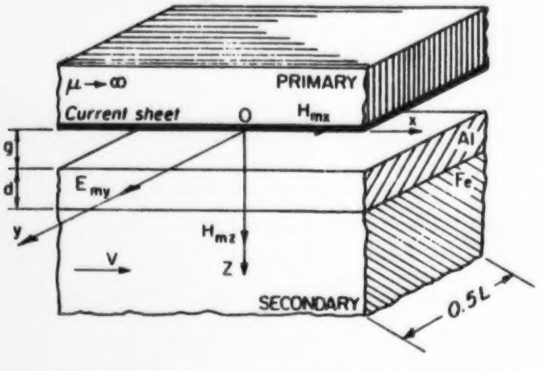

Fig. 1. Model of single-sided linear induction motor with double-layer secondary.

The effective secondary resistance now becomes smaller than for a laminated core. In addition the magnetic properties of cast steel are such that variable permeability and hysteresis losses of the core will have a significant effect on the secondary impedance. These effects should be included in any general model for SLIM design and analysis.

The analysis of a SLIM with double layer secondary presented here includes

1) skin effect in the secondary,
2) reaction of the secondary eddy current on the primary magnetic field,
3) saturation and hysteresis effects in the solid core of the secondary,
4) longitudinal end and transverse edge effects.

The two-dimensional electromagnetic field distribution is described by equations in series form which take into account the skin effect and reaction of the secondary eddy current. Saturation and hysteresis effects are included by means of the equivalent relative magnetic permeability of solid steel, μ_{re} [18]:

$$\mu_{re} = \mu_{rs}(\mu' - j\mu'') \tag{1}$$

where μ_{rs} is the surface value of relative magnetic permeability. The real and imaginary components, μ' and μ'', are described in [18].

The saturation factor for the magnetic circuit (see Appendix I) is given by

$$k_\mu = \frac{V}{2(V_g + V_d)} \tag{2}$$

where V equals the magnetomotive force (MMF) per pole pair, V_g is the magnetic potential drop across the airgap, and V_d is the magnetic potential drop across the nonmagnetic layer (i.e., the aluminum cap). In accordance with classical theory of electrical machines, the saturation factor influences the magnetizing reactance (discussed later), and the differential and slot leakage reactances of the primary.

Carter's coefficient k_c is used to obtain the equivalent airgap of the machine:

$$g' = k_c g. \tag{3}$$

The Carter coefficient must be calculated for the entrefer $(g + d)$, and it should be noted that the slot opening of the primary may have a lower magnitude than $(g + d)$.

Transverse edge effect in the solid steel reaction plate is included by correction factors described in the paper [6]. Russell and Norsworthy's correction factor [19] is used for edge effect in the high conductivity nonmagnetic layer (see Appendix II). The corrected conductivity of the aluminum cap is then

$$\sigma'_{Al} = \sigma_{Al} k_{RN}. \tag{4}$$

There are four methods for taking longitudinal end effect into account:

1) by superposition of traveling and pulsating fields [20],
2) by superposition of a wave traveling at synchronous speed and two end-effect waves [3],
3) by postulating a periodic distribution of SLIM's, and representing the resultant space harmonics by Fourier series [14], [21],
4) by modifying the electromotive force (EMF) across the mutual impedance of a T-type equivalent circuit [22], [27].

The last technique is considered to give the best results and is the simplest analytically and computationally. The end effect factor is defined as [27]

$$k_e = \frac{E_{me}}{E_{ms}} \tag{5}$$

where E_{ms} is the peak value of the EMF induced in a primary phase winding by the magnetic flux density wave traveling with synchronous velocity, and E_{me} is the peak value of EMF induced by the damped entry-end wave [3]. This method is used in this paper to compute the performance of SLIM's with double-layer secondaries, under constant current excitation.

EQUATIONS OF ELECTROMAGNETIC FIELD DISTRIBUTION

Development of the electromagnetic field equations allows the secondary and mutual impedances in the equivalent circuit of the SLIM to be determined. The plane of electromagnetic field analysis consists of three isotropic layers; the first layer is steel halfspace, the second layer is aluminum or copper plate with thickness d, and the third layer is equivalent airgap g' (3).

The assumptions for the establishment of the electromagnetic field equations are as given in [6]. For the SLIM model with double-layer secondary, as shown in Fig. 1, the electromagnetic field equations are as follows.

1) For $0 \leq z \leq g'$

$$\begin{aligned} H_{mx3} = \sum_{\nu=1}^{\infty} \frac{1}{M_\nu} \Bigg\{ & \frac{\kappa_{\nu 2}}{\beta_\nu} \left[\frac{\kappa_{\nu 1}}{\kappa_{\nu 2}} \cosh(\kappa_{\nu 2} d) \right. \\ & \left. + \mu_{re} \sinh(\kappa_{\nu 2} d) \right] \cosh[\beta_\nu (z - g')] \\ & - \left[\mu_{re} \cosh(\kappa_{\nu 2} d) + \frac{\kappa_{\nu 1}}{\kappa_{\nu 2}} \sinh(\kappa_{\nu 2} d) \right] \\ & \cdot \sinh[\beta_\nu (z - g')] \Bigg\} [-(A_{m\nu}^{+} e^{-j\beta_\nu x} + A_{m\nu}^{-} e^{j\beta_\nu x})] \end{aligned} \tag{6}$$

$$\begin{aligned} H_{mz3} = \sum_{\nu=1}^{\infty} \frac{1}{M_\nu} \Bigg\{ & \left[\mu_{re} \cosh(\kappa_{\nu 2} d) + \frac{\kappa_{\nu 1}}{\kappa_{\nu 2}} \sinh(\kappa_{\nu 2} d) \right] \\ & \cdot \cosh[\beta_\nu (z - g')] - \frac{\kappa_{\nu 2}}{\beta_\nu} \left[\frac{\kappa_{\nu 1}}{\kappa_{\nu 2}} \cosh(\kappa_{\nu 2} d) \right. \\ & \left. + \mu_{re} \sinh(\kappa_{\nu 2} d) \right] \sinh[\beta_\nu (z - g')] \Bigg\} \\ & \cdot j(A_{m\nu}^{+} e^{-j\beta_\nu x} - A_{m\nu}^{-} e^{j\beta_\nu x}) \end{aligned} \tag{7}$$

$$\begin{aligned} E_{my3} = \sum_{\nu=1}^{\infty} \frac{1}{M_\nu} \Bigg\{ & \left[\mu_{re} \cosh(\kappa_{\nu 2} d) + \frac{\kappa_{\nu 1}}{\kappa_{\nu 2}} \sinh(\kappa_{\nu 2} d) \right] \\ & \cdot \cosh[\beta_\nu (z - g')] - \frac{\kappa_{\nu 2}}{\beta_\nu} \left[\frac{\kappa_{\nu 1}}{\kappa_{\nu 2}} \cosh(\kappa_{\nu 2} d) \right. \\ & \left. + \mu_{re} \sinh(\kappa_{\nu 2} d) \right] \sinh[\beta_\nu (z - g')] \Bigg\} \cdot \\ & \cdot \frac{j\omega \mu_0}{\beta_\nu} (A_{m\nu}^{+} e^{-j\beta_\nu x} + A_{m\nu}^{-} e^{j\beta_\nu x}). \end{aligned} \tag{8}$$

2) For $g' < z < d + g'$

$$\begin{aligned} H_{mx2} = \sum_{\nu=1}^{\infty} \frac{1}{M_\nu} \frac{\kappa_{\nu 2}}{\beta_\nu} \Bigg\{ & \frac{\kappa_{\nu 1}}{\kappa_{\nu 2}} \cosh[\kappa_{\nu 2}(z - d - g')] \\ & - \mu_{re} \sinh[\kappa_{\nu 2}(z - d - g')] \Bigg\} \\ & \cdot [-(A_{m\nu}^{+} e^{-j\beta_\nu x} + A_{m\nu}^{-} e^{j\beta_\nu x})] \end{aligned} \tag{9}$$

$$\begin{aligned} H_{mz2} = \sum_{\nu=1}^{\infty} \frac{1}{M_\nu} \Bigg\{ & \mu_{re} \cosh[\kappa_{\nu 2}(z - d - g')] \\ & - \frac{\kappa_{\nu 1}}{\kappa_{\nu 2}} \sinh[\kappa_{\nu 2}(z - d - g')] \Bigg\} \\ & \cdot j(A_{m\nu}^{+} e^{-j\beta_\nu x} - A_{m\nu}^{-} e^{j\beta_\nu x}) \end{aligned} \tag{10}$$

$$\begin{aligned} E_{my2} = \sum_{\nu=1}^{\infty} \frac{1}{M_\nu} \Bigg\{ & \mu_{re} \cosh[\kappa_{\nu 2}(z - d - g')] \\ & - \frac{\kappa_{\nu 1}}{\kappa_{\nu 2}} \sinh[\kappa_{\nu 2}(z - d - g')] \Bigg\} \\ & \cdot \frac{j\omega_\nu \mu_0}{\beta_\nu} (A_{m\nu}^{+} e^{-j\beta_\nu x} + A_{m\nu}^{-} e^{j\beta_\nu x}). \end{aligned} \tag{11}$$

3) For $z \geq d + g'$

$$\begin{aligned} H_{mx1} = \sum_{\nu=1}^{\infty} \frac{1}{M_\nu} \frac{\kappa_{\nu 1}}{\beta_\nu} & e^{-\kappa_{\nu 1}(z - d - g')} \\ & \cdot [-(A_{m\nu}^{+} e^{-j\beta_\nu x} + A_{m\nu}^{-} e^{j\beta_\nu x})] \end{aligned} \tag{12}$$

$$\begin{aligned} H_{mz1} = \sum_{\nu=1}^{\infty} \frac{1}{M_\nu} & e^{-\kappa_{\nu 1}(z - d - g')} \\ & \cdot j(A_{m\nu}^{+} e^{-j\beta_\nu x} - A_{m\nu}^{-} e^{j\beta_\nu x}) \end{aligned} \tag{13}$$

$$\begin{aligned} E_{my1} = \sum_{\nu=1}^{\infty} \frac{1}{M_\nu} & e^{-\kappa_{\nu 1}(z - d - g')} \frac{j\omega_\nu \mu_0 \mu_{re}}{\beta_\nu} \\ & \cdot (A_{m\nu}^{+} e^{-j\beta_\nu x} + A_{m\nu}^{-} e^{j\beta_\nu x}) \end{aligned} \tag{14}$$

where

$$\begin{aligned} M_\nu = \frac{\kappa_{\nu 2}}{\beta_\nu} & \left[\frac{\kappa_{\nu 1}}{\kappa_{\nu 2}} \cosh(\kappa_{\nu 2} d) + \mu_{re} \sinh(\kappa_{\nu 2} d) \right] \\ & \cdot \cosh(\beta_\nu g') + \left[\mu_{re} \cosh(\kappa_{\nu 2} d) + \frac{\kappa_{\nu 1}}{\kappa_{\nu 2}} \right. \\ & \left. \cdot \sinh(\kappa_{\nu 2} d) \right] \sinh(\beta_\nu g') \end{aligned} \tag{15}$$

$$\beta_\nu = \nu \pi / \tau \tag{16}$$

$$\kappa_{\nu 1} = \sqrt{\alpha_{\nu 1}^2 + \beta_\nu^2} = (a_{R\nu \mathrm{Fe}} + j a_{x\nu \mathrm{Fe}}) k_{\nu \mathrm{Fe}} \tag{17}$$

$$\kappa_{\nu 2} = \sqrt{\alpha_{\nu 2}^2 + \beta_\nu^2} = (a_{R\nu \mathrm{Al}} + j a_{x\nu \mathrm{Al}}) k_{\nu \mathrm{Al}} \tag{18}$$

$$a_{R\nu \mathrm{Fe}} = \mathrm{Re}\,[\kappa_{\nu 1}]/k_{\nu \mathrm{Fe}} \tag{19}$$

$$a_{x\nu \mathrm{Fe}} = \mathrm{Im}\,[\kappa_{\nu 1}]/k_{\nu \mathrm{Fe}} \tag{20}$$

$$a_{R\nu \mathrm{Al}} = \mathrm{Re}\,[\kappa_{\nu 2}]/k_{\nu \mathrm{Al}} \tag{21}$$

$$a_{x\nu \mathrm{Al}} = \mathrm{Im}\,[\kappa_{\nu 2}]/k_{\nu \mathrm{Al}}. \tag{22}$$

The propagation constants and attenuation factors are equal to

$$k_{\nu \mathrm{Fe}} = \sqrt{\omega_\nu \mu_0 \mu_{rs} \sigma_{\mathrm{Fe}}/2} \tag{23}$$

$$k_{\nu \mathrm{Al}} = \sqrt{\omega_\nu \mu_0 \sigma'_{\mathrm{Al}}/2} \tag{24}$$

$$\alpha_{\nu 1} = \sqrt{j\omega_\nu \mu_0 \mu_{re} \sigma_{\mathrm{Fe}}} \tag{25}$$

$$\alpha_{\nu 2} = \sqrt{j\omega_\nu \mu_0 \sigma'_{\mathrm{Al}}}. \tag{26}$$

Time factors $\exp(j\omega_\nu^{+})$ in $A_{m\nu}^{+}$, H_{mx}^{+}, H_{mz}^{+}, E_{my}^{+}, and $\exp(j\omega_\nu^{-})$ in $A_{m\nu}^{-}$, H_{mx}^{-}, H_{mz}^{-}, E_{my}^{-}, have been eliminated. The peak values of line current density of the primary A, angular frequencies ω, and slips s, are given by the following formulae.

1) For forward traveling fields:

$$A_{m\nu}^{+} = \frac{mNk_{w\nu}\sqrt{2}\, I}{p\tau} \exp\left[j(\nu - 1) \frac{m - 1}{m} \pi \right] \tag{27}$$

$$\omega_\nu^{+} = s_\nu^{+} \omega = 2\pi f s_\nu^{+} \tag{28}$$

$$s_\nu^{+} = 1 - \nu(1 - s). \tag{29}$$

2) For backward traveling fields:

$$A_{m\nu}^{-} = \frac{mNk_{w\nu}\sqrt{2}\,I}{p\tau} \exp\left[-j(\nu + 1)\frac{m-1}{m}\pi\right] \tag{30}$$

$$\omega_\nu^{-} = s_\nu^{-}\omega = 2\pi f s_\nu^{-} \tag{31}$$

$$s_\nu^{-} = 1 + \nu(1 - s). \tag{32}$$

where m is the number of phases, N is the number of primary turns per phase, $k_{w\nu}$ is the winding factor for the νth space harmonic, p is the number of pole pairs, τ is the pole pitch, I is the primary current, and $s = (v_s - v)/v_s$. For $\nu = km \pm 1$, where $k = 0, 1, 2, 3, \cdots$, $\exp[1 \pm (\nu \mp 1)(1 - 1/m)\pi] = 1$, and $A_{m\nu}^{+} = A_{m\nu}^{-} = A_{m\nu}$.

SECONDARY IMPEDANCE

Unit secondary impedance due to each νth space harmonic is given by the ratio of tangential electric and magnetic field components, as given by (8) and (10):

$$z_{y\nu} = \left.\frac{E_{my2\nu}}{H_{mx2\nu}}\right|_{z=g'} = z_{\nu1} \cdot z_{\nu12} \tag{33}$$

where $z_{\nu1}$ is the unit impedance of the solid steel plate, and $z_{\nu12}$ is the unit equivalent impedance of the high conductivity nonmagnetic layer, which is dependent on parameters of the solid steel reaction plate. To take into account transverse edge effect, impedance $z_{\nu1}$ should be multiplied by the edge effect factor $k_{z\nu} > 1$ [6], and electric conductivity of the nonmagnetic layer should be multiplied by Russell and Norsworthy's factor $k_{RN\nu} < 1$ (Appendix II), i.e.,

$$z_{\nu1} = -\frac{j\omega_\nu\mu_0\mu_{re}}{\kappa_{\nu1}} k_{z\nu} \tag{34}$$

$$z_{\nu12} = -\frac{-\dfrac{1}{z_{\nu1}}\dfrac{j\omega_\nu\mu_0}{\kappa_{\nu2}}\sinh(\kappa_{\nu2}d) + \cosh(\kappa_{\nu2}d)}{\cosh(\kappa_{\nu2}d) - \dfrac{\kappa_{\nu2}}{j\omega_\nu\mu_0} z_{\nu1}\sinh(\kappa_{\nu2}d)} \tag{35}$$

where

$$\kappa_{\nu2} = (a_{R\nu\mathrm{Al}} + ja_{x\nu\mathrm{Al}})\sqrt{\omega_\nu\mu_0\sigma_{\mathrm{Al}}k_{\mathrm{RN}\nu}/2}.$$

For $z_{\nu1} \to \infty$, (33)–(35) give unit impedance of the aluminum cap, i.e.,

$$z_{\nu2} = \frac{-j\omega_\nu\mu_0}{\kappa_{\nu2}} \frac{1}{\tanh(\kappa_{\nu2}d_2)}. \tag{36}$$

Secondary impedance referred to the primary winding is then;

$$Z'_{\nu\mathrm{sec}} = R'_{\nu\mathrm{sec}} + jX'_{\nu\mathrm{sec}} = z_{\nu1}z_{\nu12}k_{tr\nu}\nu\frac{L}{\tau}$$

$$= \frac{z_{\nu1}z_{\nu2}}{z_{\nu1} + z_{\nu2}} k_{tr\nu}\frac{\nu L}{\tau} \tag{37}$$

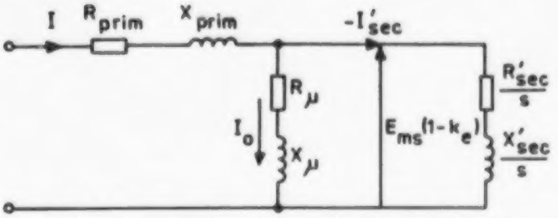

Fig. 2. Per phase equivalent circuit of linear induction motor.

where

$$k_{tr\nu} = \frac{2m(Nk_{w\nu})^2}{\nu p}.$$

The impedance of the secondary branch of the T-type equivalent circuit, as shown in Fig. 2, can now be expressed as

$$\frac{Z'_{\nu\mathrm{sec}}}{s_\nu} = \frac{R'_{\nu\mathrm{sec}}}{s_\nu} + \frac{jX'_{\nu\mathrm{sec}}}{s_\nu} = \frac{z_{\nu1}z_{\nu2}}{z_{\nu1} + z_{\nu2}} k_{tr\nu}\nu\frac{L}{\tau}\frac{1}{s_\nu}. \tag{38}$$

MUTUAL IMPEDANCE

Unit impedance "seen" below the primary current sheet can be calculated from (5) and (7), with $z = 0$, i.e.,

$$z_\nu = \left.\frac{E_{my3\nu}}{H_{mx3\nu}}\right|_{z=0} = z_{\nu1} \cdot z_{\nu12} \cdot z_{\nu123} = z_{y\nu} \cdot z_{\nu123} \tag{39}$$

where

$$z_{\nu123} = \frac{-\dfrac{1}{z_{y\nu}}\dfrac{j\omega\mu_0}{\beta_\nu}\sinh(\beta_\nu g') + \dfrac{\omega}{\omega_\nu}\cosh(\beta_\nu g')}{\cosh(\beta_\nu g') - \dfrac{\omega}{\omega_\nu}\dfrac{\beta_\nu}{j\omega\mu_0} z_{y\nu}\sinh(\beta_\nu g')}. \tag{40}$$

If $z_{y\nu} \to \infty$, the unit reactance in the magnetizing branch can be obtained, i.e.,

$$z_{\nu0} = -jx_{\nu0} = -\frac{j\omega\mu_0}{\beta_\nu}\frac{1}{\tanh(\beta_\nu g')} = -\frac{j\omega\mu_0}{\beta_\nu^2 g'}. \tag{41}$$

Magnetizing reactance referred to the primary winding is, therefore,

$$X_{\nu0} = \frac{\omega\mu_0}{\beta_\nu^2 g'} k_{tr\nu}\nu\frac{L_{\mathrm{prim}}}{\tau}. \tag{42}$$

To take into account active power losses in the primary core, an appropriate resistance $R_{\nu0}$ should be connected in parallel with $X_{\nu0}$. Mutual impedance, when resistance and reactance are connected in series, as in Fig. 2, is then given by

$$Z_{\nu\mu} = R_{\nu\mu} + jX_{\nu\mu} \tag{43}$$

where

$$R_{\nu\mu} = \frac{R_{\nu0}X_{\nu0}^2}{R_{\nu0}^2 + X_{\nu0}^2}$$

and

$$X_{rp} = \frac{R_{r0}^2 X_{r0}}{R_{r0}^2 + X_{r0}^2}. \qquad (44)$$

To take into account saturation of the magnetic circuit, the airgap g' in (42) should be multiplied by the saturation factor k_μ, according to (3) and Appendix I, i.e., $g' = gk_c k_\mu$. The component of magnetizing current due to the nonmagnetic high conductivity layer is included in secondary impedance (37).

THRUST AND NORMAL FORCE

Electromagnetic thrust for the fundamental space harmonic $\nu = 1$ is expressed by

$$F_x = \frac{m(I'_{sec})^2 R'_{sec}}{s v_s} \qquad (45)$$

where R'_{sec} results from (37), and the secondary current referred to the primary winding is

$$I'_{sec} = \frac{E_{m1}(1 - k_e)}{\sqrt{\left(\frac{R'_{sec}}{s}\right)^2 + \left(\frac{X'_{sec}}{s}\right)^2}} \qquad (46)$$

where k_e, the longitudinal end effect factor, is given by(5).

Normal force in the z direction consists of an attractive force F_{za}, and a repulsive eddy current reaction force F_{zr}, i.e.,

$$F_z = F_{za} - F_{zr}. \qquad (47)$$

The attraction force is given by

$$F_{za} = \frac{1}{2\mu_0} B_{mzg}^2 p(\tau + \Delta x)L \qquad (48)$$

where the normal component of magnetic flux density in the airgap is

$$B_{mzg} = \frac{E_{m1}(1 - k_e)}{4\sigma_k \alpha_i f N k_w \tau L}. \qquad (49)$$

In (48), Δx represents an additional length due to half-filled end slots in the linear machine. Expressions for the form factor σ_k and for the ratio α_i of the average value to peak value of magnetic flux density are given in [6].

Because F_x is proportional to B_{mzg}, and F_{zr} is proportional to B_{mxg}, the eddy current reaction force is equal to

$$F_{zr} = F_x \frac{B_{mxg}}{B_{mzg}} \qquad (50)$$

where F_x is expressed by formula (45), and the tangential component of magnetic flux density in the airgap may be found from (8) as

$$\begin{aligned} B_{mxg} &= \mu_0 |H_{mx2}|_{\nu=1, z=g', x=0} \\ &= \mu_0 \Big| [\kappa_{\nu1} \cosh(\kappa_{\nu2} d) \\ &\quad + \kappa_{\nu2} \mu_{r\nu} \sinh(\kappa_{\nu2} d)] \frac{-A_{m\nu}}{\beta_\nu M_\nu} \Big|_{\nu=1}. \end{aligned} \qquad (51)$$

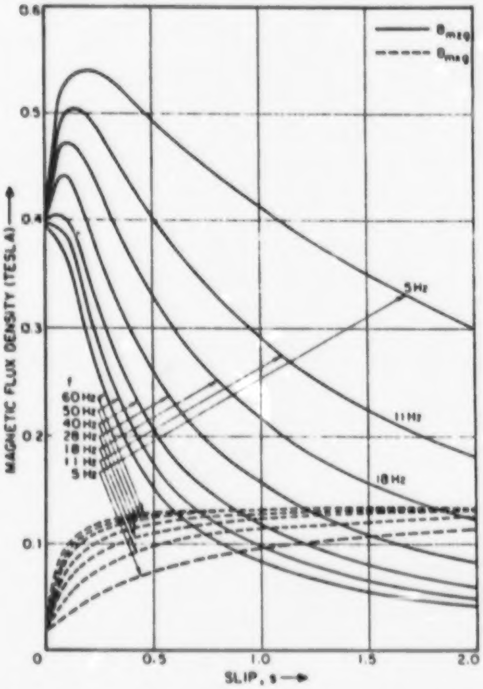

Fig. 3. Calculated peak values of normal and tangential components of magnetic flux density in airgap of the test LIM, at $I = 200$ A, $g = 15$ mm, $d = 2.5$ mm, $w = 111$ mm, $h_{cu} = 33.9$ mm.

Normal B_{mzg}, and tangential B_{mxg}, components of magnetic flux density for the test SLIM (see below) are plotted against slip in Fig. 3.

COMPARISON BETWEEN ANALAYSIS AND TEST RESULTS

The results computed from the analysis presented here were compared with experimental results obtained from a large-scale linear induction motor tested at Queen's University. The test facility consists of a 7.6-m diameter 0-101 km/h wheel, which carried the rim-mounted reaction rail, and a stationary LIM mounted in a six-component force balance and positional adjustment system. A PDP 11/03-based 64-channel data acquisition system accepts and processes test data corresponding to the phase voltages and currents (giving power and power factor), forces and moments with respect to the three coordinate axes, airgap and lateral offset at two positions along the LIM length, frequency, speed, and flux distribution in the machine. A complete description of the test facility and LIM equipment has been given previously [6], [7], [25].

The six-pole test LIM has a pole pitch of 0.25 m, a stack width of 0.101 m, and a 7/9 chorded winding [25]. The primary was excited by means of a 200-kVA variable-voltage variable-frequency inverter. The reaction rail consisted of a solid steel core, 111-mm wide by 25-mm deep, with an aluminum cap of thickness 2.5 mm over the core and 9.5 mm in the overhang.

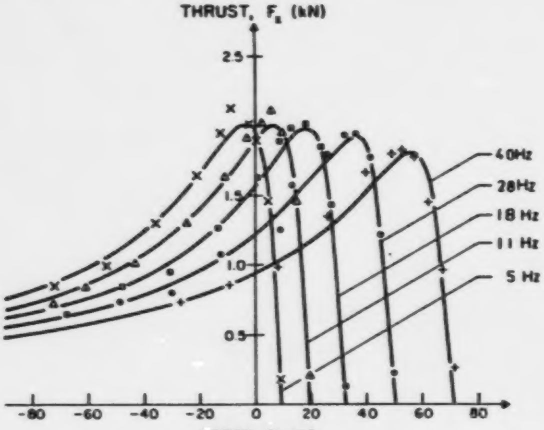

Fig. 4. Thrust F_x as function of speed at constant frequencies, for $I = 200$ A, $g = 15$ mm, $d = 2.5$ mm, $w = 111$ mm, $h_{ov} = 33.9$ mm.

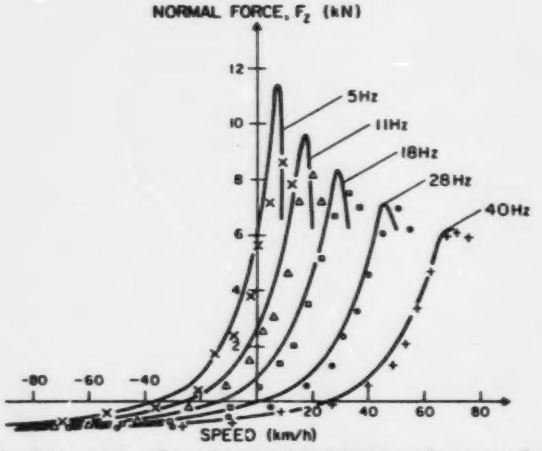

Fig. 5. Normal force F_z as a function of speed at constant frequencies, for $I = 200$ A, $g = 15$ mm, $d = 2.5$ mm, $w = 111$ mm, $h_{ov} = 33.9$ mm.

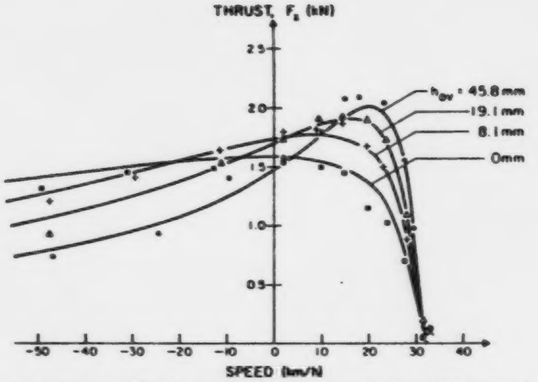

Fig. 6. Influence of aluminum cap overhang (i.e., side-bar width) on thrust, at $I = 200$ A, $f = 18$ Hz, $g = 15$ mm, $d = 2.5$ mm, $w = 111$ mm.

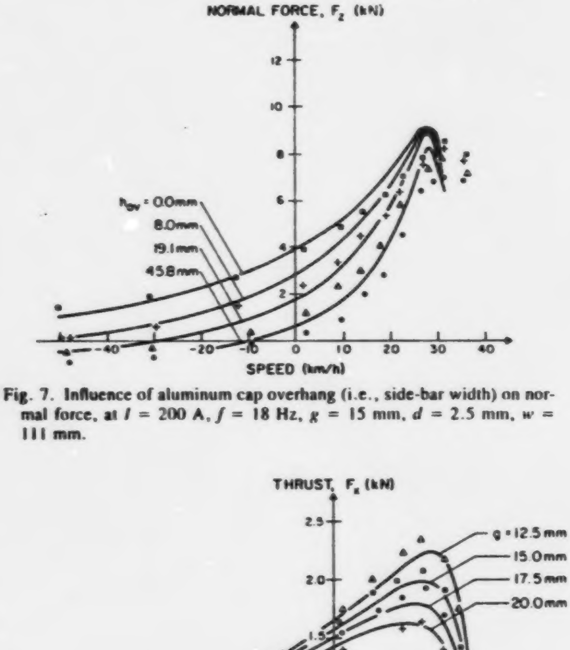

Fig. 7. Influence of aluminum cap overhang (i.e., side-bar width) on normal force, at $I = 200$ A, $f = 18$ Hz, $g = 15$ mm, $d = 2.5$ mm, $w = 111$ mm.

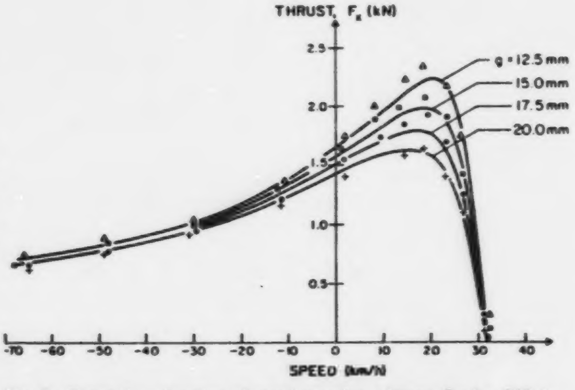

Fig. 8. Thrust F_x as function of speed at various airgaps, for $I = 200$ A, $f = 18$ Hz, $d = 2.5$ mm, $w = 111$ mm, $h_{ov} = 33.9$ mm.

Computation of the performance of a LIM with double-layer secondary was performed in a similar way to that used for the LIM with solid steel secondary [6]. The test program was conducted over a range of speeds for various levels of constant current excitation, at discrete values of frequency and airgap. In order to evaluate the effect of aluminum cap rail overhang, tests were conducted as the width of this overhang was incrementally reduced to zero.

Figs. 4 and 5 compare analytical and test results for thrust and normal forces as a function of speed at various frequencies, for $I = 200$ A, $g = 15$ mm, and with a secondary overhang width $h_{ov} = 33.9$ mm.

The influence of aluminum cap overhang on thrust and normal forces at $I = 200$ A, $g = 15$ mm, $f = 18$ Hz is shown in Figs. 6 and 7. The method of taking the overhand dimension into account is described in Appendix II.

The effect of airgap on thrust and normal forces (at $I = 200$ A, $f = 18$ Hz, $h_{ov} = 33.9$ mm) is shown in Figs. 8 and 9. It may be noted that a LIM with aluminum-capped secondary is less sensitive to variations in airgap than a LIM with solid steel reaction rail [6].

Thrust and normal forces as a function of speed at various levels of constant current in the range $100 < I <$

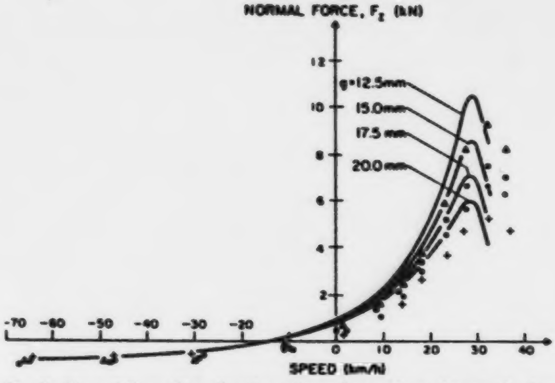

Fig. 9. Normal force F_z as function of speed at various airgaps, for I = 200 A, f = 18 Hz, d = 2.5 mm, w = 111 mm, h_{ov} = 33.9 mm.

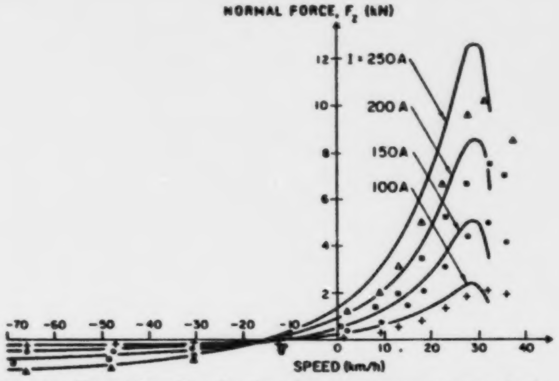

Fig. 11. Normal force F_z as function of speed at constant currents, for f = 18 Hz, g = 15 mm, d = 2.5 mm, w = 111 mm, h_{ov} = 33.9 mm.

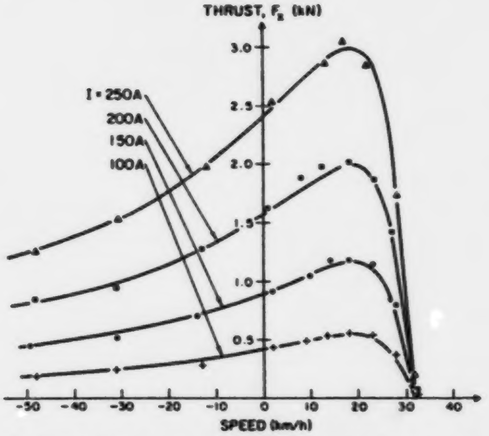

Fig. 10. Thrust F_x as function of speed at constant currents, for f = 18 Hz, g = 15 mm, d = 2.5 mm, w = 111 mm, h_{ov} = 33.9 mm.

250 A are shown in Figs. 10 and 11, for $f = 18$ Hz, $g = 15$ mm, $h_{ov} = 33.9$ mm.

For Figs. 4–11, the thrust and normal force curves were calculated for the fundamental space harmonic $\nu = 1$ using the T-type equivalent circuit shown in Fig. 2, from the analytical expressions (45), (47), (48), and (50). It has been shown that the influence of higher space harmonics on thrust, for slip $s > 0.5$, is very small (see Appendix III).

CONCLUSION

By comparing the experimental points to the analytical curves in Figs. 4–11, it may be concluded that the method for determining the mechanical performance of a linear induction motor with double-layer secondary as presented in this paper gives very good results over a wide range of frequency, airgap, current, and secondary overhang.

While this analytical approach is based on an equivalent circuit of the LIM, both mutual and secondary impedance have been evaluated from an analysis of the two-dimensional electromagnetic field distribution in the machine. Mutual impedance takes into account the nonlinearity of the magnetic circuit by including a saturation factor (2). Secondary impedance includes both complex permeability of the rail (1), which models field dependent magnetic permeability and hysteresis losses, and transverse edge effects through the correction factor discussed in Appendix II. Longitudinal end effects are included by modifying the EMF across the mutual impedance; this factor being particularly significant when $0 < s < 0.35$.

Under constant current conditions, both the maximum available thrust and the peak normal force are decreased as the input frequency is increased, primarily through the influence of longitudinal end effects and saturation of the magnetic circuit. At a particular frequency, increasing the airgap from 12.5 mm to 20.0 mm decreases the peak thrust and normal force by only about 25 and 50 percent, respectively. In plugging operation ($s > 1$), the thrust and normal forces are even less sensitive to airgap.

The effect of rail cap overhang cross section was investigated by incrementally reducing the width of the aluminum cap. It was shown analytically and experimentally that LIM performance is insensitive to overhang cross section above a certain value. Reducing the overhang below this value produces a decrease in the maximum available thrust and the peak normal force. The overhang dimension below which performance is degraded is considered to be that at which the effective longitudinal resistance of the side bar becomes significant in comparison with the effective transverse resistance of the cap over the core.

The equivalent circuit approach, with mutual and secondary parameters evaluated from two-dimensional field analysis with appropriate correction factors for edge, end and saturation effects, provides an effective tool for the calculation of LIM performance. This technique can be used for design studies of LIM's for transportation applications under constant current or, by including an additional iterative loop in computation, under constant voltage excitation conditions.

APPENDIX I
SATURATION FACTOR OF MAGNETIC CIRCUIT

The saturation factor k_μ of the magnetic circuit is evaluated by relationship (2). Because of the very high magnetic permeability assumed for the primary core, the magnetic potential drop across teeth and yoke of the primary core tends to zero. MMF due to the νth harmonic per pole pair is, therefore, equal to

$$V_\nu \simeq 2|V_{g\nu}| + 2|V_{d\nu}| + |V_{2\nu}| \tag{52}$$

where

1) magnetic potential drop across the airgap is

$$\begin{aligned} V_{g\nu} = \int_0^{g'} H_{mz\nu 3}\Big|_{x=0} dz = j\Bigg\{\Bigg[(\mu_{re} \cosh(\kappa_{\nu 2} d) \\ + \frac{\kappa_{\nu 1}}{\kappa_{\nu 2}} \sinh(\kappa_{\nu 2} d)\Bigg] \frac{\sinh(\beta_\nu g')}{\beta_\nu} \\ - \frac{\kappa_{\nu 2}}{\beta_\nu}\left[\frac{\kappa_{\nu 1}}{\kappa_{\nu 2}} \cosh(\kappa_{\nu 2} d) + \mu_{re} \sinh(\kappa_{\nu 2} d)\right] \\ \cdot \frac{1 - \cosh(\beta_\nu g')}{\beta_\nu}\Bigg\} \frac{A_{m\nu}}{M_\nu}, \end{aligned} \tag{53}$$

2) magnetic potential drop across the high conductivity nonmagnetic layer is

$$\begin{aligned} V_{d\nu} = \int_{g'}^{d+g'} H_{mz\nu 2}\Big|_{x=0} dz = j\Bigg[\mu_{re} \frac{\sinh(\kappa_{\nu 2} d)}{\kappa_{\nu 2}} \\ - \frac{\kappa_{\nu 1}}{\kappa_{\nu 2}} \frac{1 - \cosh(\kappa_{\nu 2} d)}{\kappa_{\nu 2}}\Bigg] \frac{A_{m\nu}}{M_\nu}, \end{aligned} \tag{54}$$

3) mean magnetic potential drop in the solid steel core in the x direction $V_{2\nu}$ is given in [6]. Equations (53) and (54) should be put into (2) with $\nu = 1$.

APPENDIX II
EDGE EFFECT IN HIGH CONDUCTIVITY NONMAGNETIC LAYER

Edge effect for the high conductivity layer may be taken into account by means of the Russell and Norsworthy [19] factor, i.e.,

$$k_{RN\nu} = 1 - \frac{\tanh\left(\beta_\nu \frac{w}{2}\right)}{\beta_\nu \frac{w}{2}\left[1 + \tanh\left(\beta_\nu \frac{w}{2}\right) \tanh(\beta_\nu h_{ov})\right]}. \tag{55}$$

This expression may be applied for space harmonics $\nu > 1$, although Russell and Norsworthy [19] presented it only for the first space harmonic. The coefficient $k_{RN\nu} < 1$ takes into account currents along the x axis and effectively reduces the electric conductivity of the nonmagnetic layer. In practice, the thickness of overhang t_{ov} is usually greater than the thickness of the layer over the solid iron core (Fig. 12). In this case $\tanh(\beta_\nu h_{ov})$ should be multiplied by the factor

$$1 + 1.3 \frac{t_{ov} - d}{d} > 1. \tag{56}$$

This correction factor (56) has been estimated in an empirical manner.

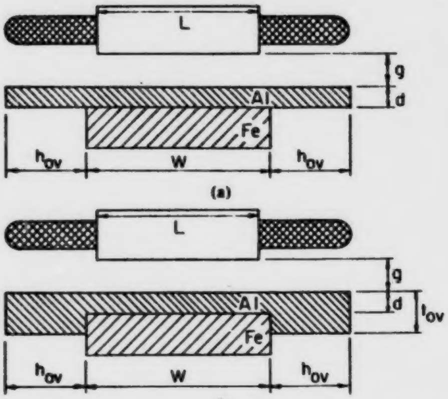

(b)

Fig. 12. Double-layer secondary with aluminum cap over solid steel core. (a) Uniform thickness in overhang and over core. (b) Thickness in overhang (side bars) greater than that over core.

TABLE I
INFLUENCE OF SPACE HARMONICS ON THRUST OF THE TEST LIM

		$\frac{F_{x\nu}}{F_{x\nu=1}}$ [percent]	
ν	$k_{w\nu}$	$s = 0.5$	$s = 1.0$
1	0.902	100.0000	100.0000
5	−0.038	−0.0335	−0.0189
7	−0.136	−0.1516	0.0936
11	−0.136	−0.0938	−0.0244
13	−0.038	−0.0038	0.0011
17	0.902	−1.5611	−0.2848
19	−0.902	−0.9926	0.2016
23	0.038	−0.0013	−0.0002
25	0.136	−0.0120	0.0019
	Total	97.1503	99.9699

$s = 1.0$, $f = 18$ Hz, $I = 200$ A, $g = 15$ mm, $d = 2.5$ mm, $w = 111$ mm.

APPENDIX III
INFLUENCE OF HIGHER SPACE HARMONICS ON THRUST

The effect of higher space harmonics on thrust has been determined using the equivalent circuit. The results for the test LIM are given in Table I. While the 17th and 19th harmonics are the most significant, the effect of all higher space harmonics is very small. While small, the influence of higher space harmonics on thrust is greater for a LIM with two layer (aluminum-capped) secondary than for a LIM with a homogeneous solid steel reaction rail [6].

ACKNOWLEDGMENT

One of the authors (J.F.G.) is indebted to NSERC for an International Scientific Exchange Award to conduct research at Queen's University for the year 1983/84.

REFERENCES

[1] E. R. Laithwaite, *Induction Machines for Special Purposes*. London: Newnes, 1966.

[2] S. A. Nasar and I. Boldea, *Linear Motion Electric Machines*. New York: Wiley, 1976.

[3] S. Yamamura, *Theory of Linear Induction Motors*. New York: Wiley, 1972.

[4] M. Poloujadoff, *The Theory of Linear Induction Machinery*. Oxford: Clarendon, 1980.

[5] G. E. Dawson, A. K. Wallace, A. R. Eastham, and A. M. A. Kamar, "Design study of a LIM with solid steel reaction rail for urban transit," in *Proc. Int. Conf. Electrical Machines*, ICEM '82, Budapest, 1982, part 3, pp. 992–995.

[6] J. F. Gieras, A. R. Eastham, and G. E. Dawson, "Performance calculation for single-sided linear induction motors with a solid steel reaction plate under constant current excitation," *Proc. IEE*, Part B, vol. 132, pp. 185–194, 1985.

[7] G. E. Dawson and A. R. Eastham, "The comparative performance of single-sided linear induction motors with squirrel-cage, solid-steel and aluminum-capped reaction rails," in *16th Annu. IEEE Ind. Appl. Soc. Meeting*, Philadelphia, Oct. 1981, IEEE Conf. Record 81 CH 1678-2, pp. 323–329.

[8] A. Smilgevicius, "Impedance of ferromagnetic rotor with conductive cap," (in Russian), in *Elektriceskie Masiny i Elektroprivod Maloj Moscnosti*, Moskva-Leningrad, Nauka, 1960, pp. 90–95.

[9] M. S. Sarma and G. R. Soni, "Solid-rotor and composite-rotor induction machines," *IEEE Trans. Aerospace*, vol. AES-8, pp. 147–155, 1972.

[10] J. Gieras, "Theory of induction machines with double-layer secondary," *Rozprawy Elektrotechniczne*, 23, pp. 577–631, 1977.

[11] E. M. Freeman, "Travelling waves in induction machines: Input impedance and equivalent circuits," *Proc. IEE*, vol. 115, pp. 1772–1776, 1968.

[12] E. M. Freeman and D. A. Lowther, "Normal force in single-sided linear induction motors," *Proc. IEE*, vol. 120, pp. 1499–1506, 1973.

[13] B. T. Ooi and D. C. White, "Traction and normal forces in linear induction motor," *IEEE Trans. Power Apparatus Syst.*, vol. PAS-89, pp. 638–645, 1970.

[14] I. Boldea and M. Babescu, "Multilayer approach to the analysis of single-sided linear induction modors," *Proc. IEE*, vol. 125, pp. 283–287, 1978.

[15] M. Yamazoe, "Analysis and experiments of single-sided linear induction motor," *Elect. Eng. Japan*, vol. 100, pp. 9–18, 1980.

[16] S. Tanaka and S. Tadakuma, "Magnetic levitation and propulsion system by single-sided linear induction motor," *Elect. Eng. Japan*, vol. 100, pp. 116–123, 1980.

[17] M. Ivamoto, S. Sakabe, K. Itani, K. Kitagawa, and G. Utsumi, "Experimental and theoretical study of high speed single-sided linear induction motors," *IEE Proc. Part B, Electric Power Applications*, vol. 128, pp. 306–312, 1981.

[18] J. F. Gieras, "Analytical method of calculating the electromagnetic field and power losses in ferromagnetic halfspace, taking into account saturation and hysteresis," *Proc. IEE*, vol. 127, pp. 1098–1104, 1977.

[19] R. L. Russell and K. M. Norsworthy, "Eddy currents and wall losses in screened rotor induction motors," *Proc. IEE*, vol. 105A, pp. 163–175, 1958.

[20] A. I. Voldek, "Induction magnetohydrodynamic machines with liquid metal secondary" (in Russian), Energia, Leningrad, 1970.

[21] K. Yoshida, "New transfer-matrix threoy of linear induction machines, taking into account longitudinal and transverse ferromagnetic end effects," *IEE Proc., Part B, Electric Power Application*, vol. 128, pp. 225–236, 1981.

[22] T. Hirasa, S. Ishikawa, and T. Yamamuro, "Equivalent circuit of linear induction motors with end effect taken into account," *Elec. Eng. Japan*, vol. 100, pp. 65–71, 1980.

[23] J. Gieras, "Elements of electromagnetic theory of induction machines," (in Polish), D.Sc. thesis, Zeszyty Naukowe ATR *Elektrotechnika*, no. 2, Bydgoszcz, Poland, 1979.

[24] J. F. Gieras, "Simplified theory of double-sided linear induction motor with squirrel-cage secondary," *IEE Proc., Part B*, vol. 130, pp. 424–430, 1983.

[25] A. R. Eastham, G. E. Dawson, D. L. Atherton, and C. L. Schwalm, "Test facility for determination of linear induction motor performance," CIGGT Rep. No. 80-6, Queen's Univ., Kingston, 1980.

[26] A. R. Eastham, G. E. Dawson, D. M. Pringle, and J. M. Davidson, "Comparative experimental evaluation of the performance of a SLIM with a solid-steel reaction rail and with an aluminum-capped reaction rail," CIGGT Rep. No. 80-7, Queen's Univ., Kingston, 1980.

[27] J. F. Gieras, G. E. Dawson, and A. R. Eastham, "A new longitudinal end effect factor for linear induction motors," Paper 86 WM 209-1, presented at IEEE Power Engineering Society 1986 Winter Meeting, New York, Feb. 1986.

APPENDIX B

FINITE ELEMENT ANALYSIS OF LIMs

B.1 PROBLEM DEFINITION

In any two-dimensional region, R, in the x-y plane bounded by a closed contour, S, the magnetic vector potential, A, satisfies the nonlinear Poisson equation:

$$\nabla \times \nu \nabla \times A = -J \qquad (B.1)$$

where ∇ is the operator $\partial/\partial x \, \bar{i} + \partial/\partial y \, \bar{j}$

A is the z-component of the magnetic vector potential

ν is the material reluctivity

J is the z-directed current which, depending on position, can take the following values:

(i) stator slots $J = J_s$
(ii) nonconducting medium $J = 0$
(iii) rotor plate $J = 0 \, \sigma(E + u \times B)$

where $E = \partial A/\partial T$ and $\nabla B = \nabla \times A$

For an induction machine problem, the net induced current density in the rotor is due to both transformer and velocity effects.

Equation (B.1) may be rewritten as:

$$\partial/\partial x \, (\nu \partial A/\partial x) + \partial/\partial y (\nu \partial A/\partial y) = -J \qquad (B.2)$$

B.1.1 Assumptions

(a) The field distribution is assumed to be uniform in the z-direction. Transverse edge effects are accounted for by correcting the secondary conductivity by use of the Russell & Norsworthy factor [45]:

$$K_{RN} = 1 - \tanh(\tfrac{1}{2} w)/(\tfrac{1}{2}\beta w[1+\tanh(\tfrac{1}{2}\beta w)\tanh(\beta h_{ov})]) \qquad (B.3)$$

where $\beta = \pi/\tau$.

(b) The stator current is known and has only a z-component.

(c) Ferromagnetic materials are isotropic, and B-H characteristics are single valued.

(d) The magnetic field outside the region of discretization is negligible, and hence the boundary contour is treated as a constant potential line with $A = 0$.

(e) The induced currents in the current-carrying conductors are neglected.

(f) The displacement currents are neglected.

There are two methods of formulating Equation (B.2) for solution:

(i) variational method
(ii) Galerkin method.

Both methods will be discussed in the following sections.

B.2 VARIATIONAL FORMULATION

The solution of the boundary value problem (Figure B.1) is obtained first by formulating the partial differential equation in variational terms [46,47] by an energy-related expression called a functional, and then by searching for a function, A, that minimizes the functional instead of attempting to solve Equation (B.2) directly. It is known in variational calculus that the correct solution of Equation (B.2) is that which minimizes the functional whose Euler equation yields the partial differential equation being solved. The appropriate functional for Equation (B.2) is given by:

$$F = \iint_R [\ \tfrac{1}{2}\nu((\partial A/\partial x)^2 + (\partial A/\partial y)^2) + \sigma A \partial A/\partial t - J_s A + \tfrac{1}{2}\sigma u A \partial A/\partial x]\ ds \quad (B.4)$$

where R is the area of definition of the problem.

The vector potential, A, may be expressed as any one of a number of interpolation functions [48]. In this text, the vector potential at any point on an element is assumed to be a linear interpolate of the values at its vertices. First-order elements were preferred because of the simpler computer implementation, i.e.

$$A(x,y) = 1/(2\Delta)\Sigma(\ p_i + q_i x + r_i y\ )\ A_i \qquad (B.5)$$

with $i = 1,2,3$

and where $p_1 = x_2y_3 - x_3y_2$

$q_1 = y_2 - y_3.$

$r_1 = x_3 - x_2$

Δ = area of

in cyclic modulo 3.

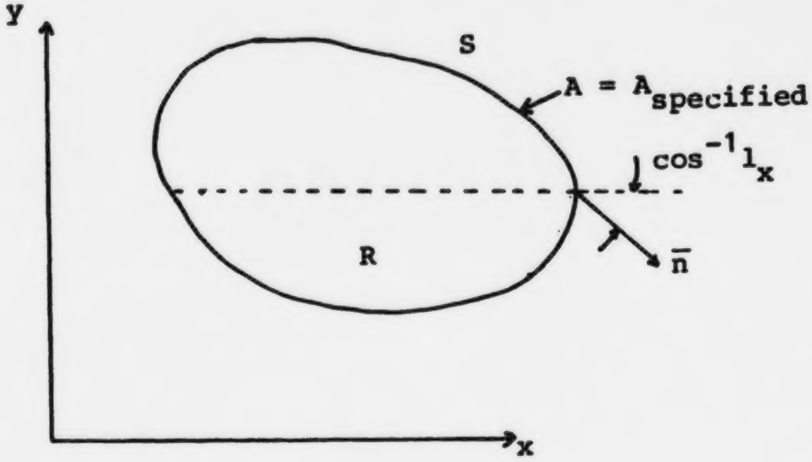

Figure B.1 Schematic showing the problem region for finite element solution

The choice of first-order elements implies that the flux density (and hence the permability) is constant in any one element, and is obtained by differentiating Equation (B.5).

$$B_x = 1/(2\Delta)\Sigma r_k A_k \qquad B_y = 1/(2\Delta)\Sigma q_k A_k \qquad \text{(B.6)}$$

Now, to minimize the functional, set the derivative with respect to each of the vertex potentials to zero, i.e.

$$\partial F/\partial A_k = 0 \qquad \text{for all } k \qquad \text{(B.7)}$$

which on simplification yields:

$$\nu[S][A] + \sigma\partial/\partial t[T][A] + \sigma u[Q][A] = [T][J_s] \qquad \text{(B.8)}$$

where:

$$S = 1/4\Delta \begin{bmatrix} b_1b_1+c_1c_1 & b_1b_2+c_1c_2 & b_1b_3+c_1c_3 \\ b_2b_1+c_2c_1 & b_2b_2+c_2c_2 & b_2b_3+c_2c_3 \\ b_3b_1+c_3c_1 & b_3b_2+c_3c_2 & b_3b_3+c_3c_3 \end{bmatrix}$$

$$T = \Delta/12 \begin{bmatrix} 2 & 1 & 1 \\ 1 & 2 & 1 \\ 1 & 1 & 2 \end{bmatrix}$$

$$Q = 1/6 \begin{bmatrix} b_1 & b_2 & b_3 \\ b_1 & b_2 & b_3 \\ b_1 & b_2 & b_3 \end{bmatrix}$$

B.3 GALERKIN METHOD

Equation (B.8) may also be derived by Galerkin's weak formulation [47] as follows. Let the interpolation formula for the vector potentials be written as:

$$A = \sum \alpha_i A_i \qquad \text{(B.9)}$$

where α_i, the shape function, is given by:

$$\alpha_1 = 1/(2\Delta) \; ((x_2y_3-x_3y_2) + (y_2-y_3)x + (x_3-x_2)y) \qquad \text{(B.10)}$$

in cyclic modulo 3.

Then, using the Galerkin criterion, we can write Equation (B.2) as:

$$\iint_R \alpha_i \left[\partial/\partial x(\nu \partial A/\partial x) + \partial/\partial y(\nu \partial A/\partial y) + \sigma \partial A/\partial t - J_s + \sigma u \partial A/\partial x \right] ds = 0 \qquad i = 1,2,3 \qquad \text{(B.11)}$$

The above equation, on simplification, also yields Equation (B.8).

B.4 METHODS OF SOLUTION

The matrix Equation (B.8) represents the set of equations obtained by variational or Galerkin methods of transformation of the field problem defined by the partial differential Equation (B.2). This equation has a time derivative term and hence cannot be solved directly. The two techniques for solving this type of equation are:

(i) time stepping or time marching method
(ii) complex steady-state method.

The latter method was used exclusively in this investigation in view of its computational efficiency.

B.4.1 Complex Steady-State Method

In this method the fields are assumed to be harmonic functions of time such that:

$$\bar{A} = Ae^{j\omega t} \qquad \text{and} \qquad J = J_s e^{j\omega t} \qquad \text{(B.12)}$$

Hence, the time derivative in Equation (B.8) may be replaced by $j\omega$. Then Equation (B.8) can be rewritten as:

$$\nu[S][A] + j\omega\sigma[T][A] + \sigma u[Q][A] = [T][J_s] \qquad \text{(B.13)}$$

The variables are now represented by complex space phasors, the corresponding physical time-varying field being recovered as the real part of $A\exp(j\omega t)$, where ω is the angular frequency of the sinusoidal excitation. The above nonlinear equation is solved by using the chord iteration technique.

The chord method is a simple iteration method to find the correct reluctivity of each element. At any step in the iteration, the reluctivity of each element is at first calculated from the B-H curve of the material of the element, knowing the local flux density. An underrelaxation factor is used to modify the reluctivities to improve the convergence of the solution. The modified reluctivity is given by the expression:

$$\nu'_{new} = \nu_{old} + e(\nu_{new} - \nu_{old}) \qquad (B.14)$$

where: ν'_{new} = modified reluctivity for next iteration

ν_{old} = reluctivity of the present iteration

ν_{new} = reluctivity calculated from the B-H curve using the flux density in the present iteration

e = convergence factor.

The solution is said to converge when the following two conditions are satisfied:

(i) the maximum difference in potential and the difference in average potential at individual nodes, between two consecutive iterations, are less than specified values

(ii) the maximum difference in permeability between two consecutive iterations is less than a specified value.

The effect of changing the convergence factor and other aspects of convergence using this technique has already been studied in detail [49].

The Newton Raphson method is not feasible for this procedure because of the following two constraints:

(i) The vector potential, being a complex quantity, doubles the number of variables to be solved. Besides, if the real and imaginary parts are considered as two separate variables, then the global matrix loses its parsity.

(ii) It is difficult to establish a reasonable convergence criteria, since the variables are complex.

B.5 ASSEMBLY OF THE GLOBAL MATRIX

All the above equations were developed for a single element. In order to solve the field for the entire region, the above operations must be repeated for all the elements in the region. The global matrix equations are obtained for all the elements in the region. The global matrix equations are obtained by assembling the individual element matrices, as explained in [48]. In the minimization of the energy functional, the potential of each node is allowed to vary freely and hence does not correspond to the actual boundary value problem. The global matrix equations must therefore be modified so that the equations on solution will yield the specified values at the boundary nodes, thus satisfying the boundary conditions.

B.6 MATRIX STORAGE AND SOLUTION

The final matrix equation which has to be solved may be written as:

$$[D][\delta A] = [J] \qquad \text{B.15)}$$

This matrix equation represents a set of linear equations which can be solved by Gaussian elimination. The matrix, D, is banded but non-symmetric due to the velocity term. The matrix, D, is stored as a banded matrix, thus reducing storage space. An efficient Gaussian elimination algorithm to solve banded matrices is then used to solve the equations.